

2008

The semiclassical description of the energy spectrum of hydrogen in near-perpendicular fields

Christopher Robert Schleif
College of William & Mary - Arts & Sciences

Follow this and additional works at: <https://scholarworks.wm.edu/etd>



Part of the [Atomic, Molecular and Optical Physics Commons](#)

Recommended Citation

Schleif, Christopher Robert, "The semiclassical description of the energy spectrum of hydrogen in near-perpendicular fields" (2008). *Dissertations, Theses, and Masters Projects*. Paper 1539623533.
<https://dx.doi.org/doi:10.21220/s2-cqym-jj40>

This Dissertation is brought to you for free and open access by the Theses, Dissertations, & Master Projects at W&M ScholarWorks. It has been accepted for inclusion in Dissertations, Theses, and Masters Projects by an authorized administrator of W&M ScholarWorks. For more information, please contact scholarworks@wm.edu.

The Semiclassical Description of the Energy Spectrum of Hydrogen in Near-Perpendicular Fields

Christopher Robert Schleif

Pleasantville, New York

Bachelor of Music, University of Hartford, 1997
Masters of Science, The College of William and Mary, 2003

A Dissertation presented to the Graduate Faculty
of the College of William and Mary in Candidacy for the Degree of
Doctor of Philosophy

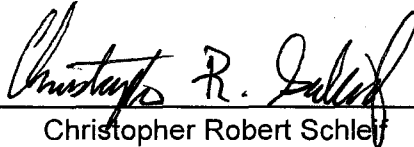
The Department of Physics

The College of William and Mary
August 2008

APPROVAL PAGE

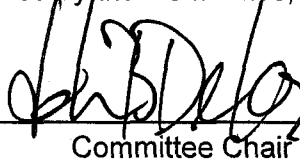
This Dissertation is submitted in partial fulfillment of
The requirements for the degree of

Doctor of Philosophy



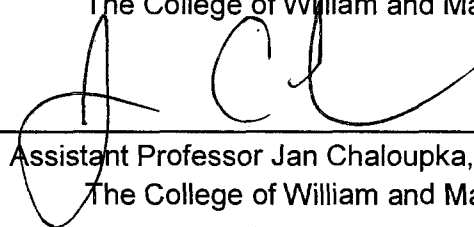
Christopher Robert Schlett

Approved by the Committee, June 2008

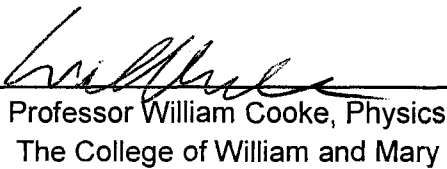


Committee Chair

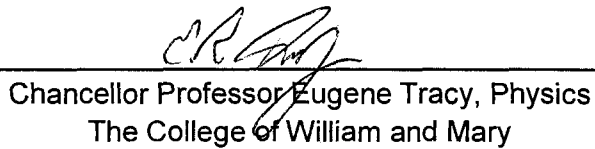
Professor John Delos, Physics
The College of William and Mary



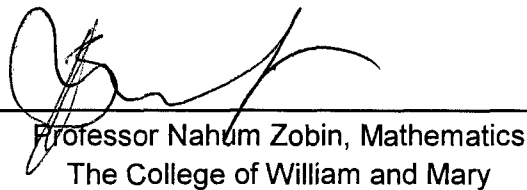
Assistant Professor Jan Chaloupka, Physics
The College of William and Mary



Professor William Cooke, Physics
The College of William and Mary



Chancellor Professor Eugene Tracy, Physics
The College of William and Mary



Professor Nahum Zobin, Mathematics
The College of William and Mary

ABSTRACT PAGE

We examine the energy spectrum of hydrogen in weak near-perpendicular electric and magnetic fields using quantum computations and semiclassical analysis. The structure of the quantum spectrum is displayed in a lattice constructed by plotting the difference between total energy and first order energy versus first order energy, for all states of a given principal quantum number n . For some field parameters, the lattice structure is not regular, but has a lattice defect structure which may be characterized by the transport of lattice vectors. We find that in near-perpendicular fields the structure of the spectrum is divided into six distinct parameter regions, which we characterize by the presence and type of lattice defect. To explain this structure we examine a corresponding classical system which we have derived by classical perturbation theory. Starting from Kepler action and angle variables, we give a derivation of a classical Hamiltonian to second order in perturbation theory; the derivation is different from, but the final result agrees with previous work. We focus especially on the topological structure of the reduced phase space and on the resulting topological structure of the trajectories. We show that construction of action variables by the obvious methods leads to variables that have discontinuous derivatives. Smooth continuation of these "primitive" action variables leads to action variables that are multivalued. We show how these multivalued actions lead to lattice defects in the quantum spectrum. Finally we present a few correlation diagrams which show how quantum eigenvalues evolve from one region of near-perpendicular parameter space to another and show how the structure of the quantum correlations is related to structures in the classical phase space.

Contents

I	Introduction	
II	Lattice Defects and the Structure of the Energy Spectrum of Hydrogen in Near Perpendicular Electric and Magnetic Fields	
I.	Perpendicular Fields	5
II.	Near-Perpendicular Fields	13
A.	Region II: Bifurcations from the Perpendicular Monodromy Interval	14
B.	Regions I.S and I.Z	16
C.	Completely Regular Region R	17
D.	Stark Region: Bifurcations from Perpendicular Fields near the Stark Limit	18
E.	Zeeman Region: Bifurcations from Perpendicular Fields near the Zeeman Limit	26
III.	Conclusion	30
III	Static Monodromy and Multivalued Classical Action Variables	
IV.	Overview	31
V.	Integrable Systems and the Existence of Local Smooth Action Variables	32
A.	The Existence of Tori and Locally Smooth Actions	33
1.	Classical Tori	33
2.	Smooth actions and vectors from the Period Lattice	34
3.	Monodromy	35

B. Primitive Actions	35
----------------------	----

IV Semiclassical Theory of the Structure of the Hydrogen Spectrum in Near-Perpendicular Electric and Magnetic Fields: Derivations and Formulae for EBKM Quantization and Description of Monodromy

VI. Overview	39
A. The classical trajectories	39
B. Comparison with other work	41
VII. Degenerate Perturbation of the Kepler Motion	43
A. Canonical perturbation theory	44
VIII. First Order Dynamics: The Pauli Precession	48
A. The Pauli Precession	48
B. Local canonical coordinates on $S^2 \times S^2$	49
C. Degenerate coordinates on the Pauli 2-Torus	51
IX. Degenerate Perturbation of the Pauli Motion	52
A. The fully reduced Hamiltonian	54
B. Expression in scaled parameters	55
X. Reduced Descriptions	56
A. The structure of the four dimensional reduced phase space Γ_N	56
B. The two dimensional fully reduced phase space $\Gamma_{N,Q}$	58
C. The definition of the classical spectrum	61
D. Connected components of the (Q, h_2) level sets	62
XI. Monodromy of Actions	64

A. Primitive action integrals	66
B. Intrinsically multivalued smooth classical action variables	73
C. Monodromy and vector transport	73
XII. Multivalued Actions and Quantum Lattice Defects	78
A. EBKM Quantization	78
B. Quantum operators	79
C. Quantum lattices	81
XIII. The Structure of Spectra in Near Perpendicular Fields	82
A. The structure of h_2 on $\Gamma_{N,Q}$ at $Q = 0$	85
B. The structure of h_2 on $\Gamma_{N,Q}$ for $ Q > 0$	87
C. The map revisited	89
XIV. Quantum Correlation Diagrams	91
A. Degeneracy breaking: From perpendicular to near-perpendicular fields	91
B. From the Zeeman Limit to the Stark Limit in near perpendicular fields	96
XV. Conclusion:	99
A. Kepler Averaging	100
1. Average in the orbital frame	100
2. Computing Eq. 24 of Section VII A	101
a. The explicit generating function f_1	102
b. The second order Hamiltonian is independent of $F_x B$	103
c. Computing $\langle H_2' \rangle_{\phi_N}$	103
B. The Topology of $\Gamma_{N,Q}$	105

V Supplements to Part IV

C. Supplementary Material	108
References	134
Vita	138

Part I

Introduction

The quantum spectrum of Hydrogen in near-perpendicular electric and magnetic fields has an interesting and somewhat complex structure in the second order energy eigenvalues. The behavior and classification of these spectral structures becomes clear and intuitive when the global structure of the analogous classical system is examined.

The Hydrogen atom in applied fields has long been a model system for the study of order and chaos in classical and quantum mechanics, because it has just two or three degrees of freedom and a collection of controllable parameters, and because it is accessible to both theory and experiment [1]. The first order spectrum in combined electric and magnetic fields was examined roughly 80 years ago by Pauli [2] and relatively recently explored in experiments [3]. Recently, much attention has been given to the spectrum at higher order [4] with work closely related to the present work appearing in publications by Uzer, Gourlay, Farrelly and Milczewski [5], [6], [7] and Solov'ev, Herrick and Braun [8], [9], [10]. Publications by Sadovskii and Cushman [11], [12], [13] have pointed out that for exactly perpendicular fields and a certain interval of field strength ratio, the spectrum displays effects of action-angle monodromy. Recently, we have published two papers which extend these results and have formed the basis of this thesis. In Ref. [14], we showed that if the fields are tilted slightly away from perpendicular, then the phenomena predicted by Sadovskii and Cushman are modified, and additional phenomena are present at other field ratios. In Ref. [15] we showed how such phenomena are connected with quantized classical actions. In this thesis we present the full details of the analysis on which our conclusions were based.

In part II we examine the second order quantum spectra by examining and classifying the structure of spectral lattices related to the approximate constants of the motion

in the classical system. These lattices are formed by the expectation values of quantum operators, but they may be constructed directly from the spectrum by simple inspection of the energy values. When the fields are weak and nearly perpendicular, the n^2 degenerate states at each principal quantum number n are split into $2n - 1$ equally spaced clusters of closely spaced levels (Fig. 1(a)). The clusters are displaced symmetrically about $E_o = -\frac{1}{2n^2}$, and may be labeled by an integer q which ranges from $-(n - 1)$ to $n - 1$ such that the energy of each state in a cluster is located near

$$E_{cluster} = -\frac{1}{2n^2} + \frac{1}{2}\sqrt{B^2 + (3nF)^2}q \quad (1)$$

and the cluster contains exactly $n - |q|$ quantum states. The second-order energy $E - E_{cluster}(n, q) = h_2$ contains the structure which we wish to investigate.

To investigate this structure, the spectra can be arranged in a lattice if for each state in a given n -manifold one plots the second-order energy h_2 versus q (A more rigorous lattice construction using expectation values of quantum operators is explained in Section XII). For some parameter regimes the resulting lattices may have various features such as lattice defects (Fig. 1(b)), double degeneracy, or they may contain regions which display anti-crossings between states of the same q as the fields are varied. Such features can be understood by semiclassical analysis.

In part III we discuss a global structure of phase space found in some classical systems. This structure is commonly called “Monodromy”, and in part III we show how it is identified with the presence of a multivalued action variable as a function of the constants of the motion. This structure exists in the classical system describing Hydrogen in near-perpendicular fields for many regions of the parameter space, and is directly responsible for the structure of the quantum lattice defects. The discussion in this section is a bit more abstract than the rest of the thesis, and can be skipped on first reading.

In part IV we present the whole semiclassical theory, and the structure of spec-

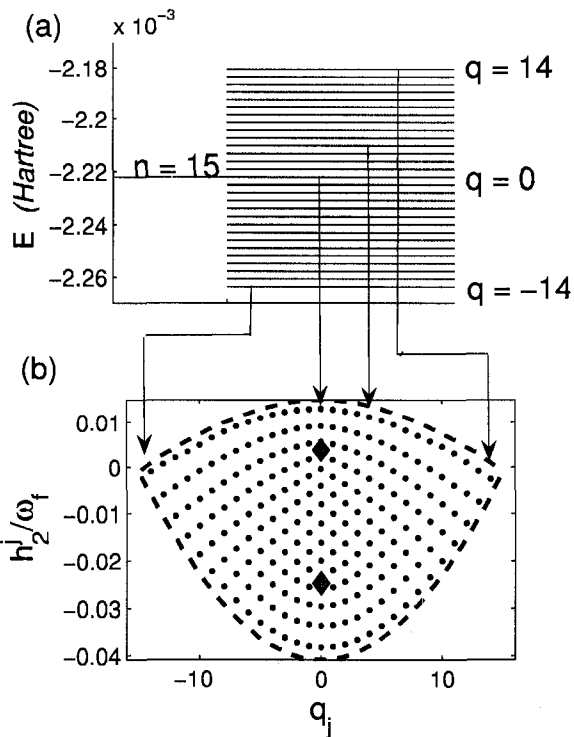


FIG. 1: (color online) (a) The effects of near-perpendicular fields on the energy spectrum of a spinless hydrogen atom at principal quantum number $n = 15$ for electric field $F = 11.14$ V/cm and magnetic field $B = 1.393$ T and $\mathbf{F} \cdot \mathbf{B} = 0.002FB$ or $\theta = 54^\circ$, $\omega_f = 2.963(10^{-6})$ and $\chi = 0.2\omega_f n^3$ (ω_f has the units of a magnetic field and is reported in atomic units in all figures). The quantum basis included n manifolds 12 – 18. When the fields are turned on, the n^2 -degenerate n -manifolds are split into $2n - 1$ equally spaced q -manifolds each containing $n - |q|$ levels. The difference between an energy level and the energy of its parent q -manifold is denoted h_2 . (b) Structure in the second order energies in an n -manifold is made visible by plotting h_2 versus q (In all lattice figures we plot h_2/ω_f with units of energy/magnetic field reported in atomic units). At these field parameters (Region II) the lattice has two defects associated with the values of q and h_2 which are marked by (cyan online) diamonds. For various field parameters the structure in the second order energy spectrum generates various families of spectral lattices. This structure is explained by examining the properties of the classical actions of a Hamiltonian system obtained from Poincaré-Von Zeipel perturbation theory.

tral lattices is predicted for the entire near-perpendicular parameter space using Einstein-Brillouin-Keller-Maslov (EBKM) quantization of approximate action variables ([16], [17], [18], [19]). After having derived the semiclassical connection in full details, we present details of the quantum operators associated with the approximate constants of the motion in section XII B. We then interpret the structure of the quantum lat-

tices semiclassically in section XIII, and then examine the structure of a few quantum correlation diagrams in section XIV.

The derivations for most of the formulas in part IV are complete, but are presented as compactly as possible. To help fill in the gaps, Part V includes a collection of supplementary details of derivations of formulas which were too tedious to include in the main discussion.

Part II

Lattice Defects and the Structure of the Energy Spectrum of Hydrogen in Near Perpendicular Electric and Magnetic Fields

In this part we construct spectral lattices from a list of energy eigenvalues. We then show how to classify these spectra by considering the transport of lattice vectors. This classification scheme leads to six distinct parameter regimes in the near perpendicular parameter space. Where necessary we indicate how semiclassical analysis was used to produce these results, but the full semiclassical analysis is not presented until part IV.

I. PERPENDICULAR FIELDS

We consider the quantum energy spectrum of a non-relativistic, spinless hydrogen atom in static electric and magnetic fields \mathbf{F} and \mathbf{B} . Let the \mathbf{B} field vector define the z axis and let the \mathbf{F} and \mathbf{B} field vectors together define the $x - z$ plane with χ denoting the angle between \mathbf{F} and the x axis. Then for weak, nearly-perpendicular fields [20] the Hamiltonian may be written in the following ordering (Atomic units):

$$\hat{H} = \hat{H}_0 + \hat{H}_1 + \hat{H}_2 = \underbrace{\frac{p^2}{2} - \frac{1}{r}}_{\hat{H}_0} + \underbrace{\frac{B}{2}L_z + xF}_{\hat{H}_1} + \underbrace{x F(\cos\chi - 1) + z F \sin\chi + \frac{B^2}{8}(x^2 + y^2)}_{\hat{H}_2} \quad (2)$$

To obtain a collection of quantum spectra we expand the wave function in a basis [21] of spherical eigenstates of \hat{H}_0 , and compute eigenvalues E_j of the resulting matrix (Fig. 2a).

The structure of the energy spectra may be summarized as follows: (i) The n -manifolds, as well as a further residual near degeneracy are clearly distinguishable (Fig. 2a). (ii) Each n manifold is split into $2n - 1$ equally spaced clusters of levels symmetrically displaced about $E_0 = -\frac{1}{2n^2}$. (iii) The spacing between clusters depends upon the field strengths, and upon n in proportion to

$$\omega_f \equiv \frac{1}{2}\sqrt{B^2 + (3nF)^2} \quad (3)$$

(iv) Each cluster can be labeled by an integer quantum number q , where $-(n-1) \leq q \leq (n-1)$ such that the energy of each cluster, (henceforth referred to as a q -manifold), is given by: $E_q = E_0 + q\omega_f$. (v) Each q -manifold contains exactly $n - |q|$ states [see 2b]. These properties suggest that one may write each energy eigenvalue E_j as the sum of energies of the n -manifold, q -manifold and a small remaining term denoted h_2 . Then,

$$E_j = E_{n,q,h_2} = -\frac{1}{2n^2} + \omega_f q + h_2 \quad (4)$$

The quantity ω_f defined in Eq. 3 is considered to be an effective field strength characterizing the magnitude of the combined field perturbation such that $|h_2| \sim \omega_f^2$. The following definition of θ allows a convenient parameterization of all possible field magnitude ratios at a given perturbation strength ω_f :

$$\theta = \tan^{-1} \left(\frac{3n|F|}{|B|} \right) \quad (5a)$$

$$0 \leq \theta \leq \pi/2 \quad (5b)$$

This implies $F = 2\omega_f \sin(\theta)/3n$ and $B = 2\omega_f \cos\theta$ with the Zeeman and Stark limits at $\theta = 0$ and $\theta = \pi/2$ respectively. The main utility of this parameterization is that the characteristic shape and features of each spectral lattice are stationary with respect to n at fixed θ and fixed scaled angle $\chi/\omega_f n^3$. Changing n only changes the number of lattice points which populate the fixed structure.

To investigate the structure present in the second order corrections h_2 , it is useful to plot the value of h_2 versus q . The resulting plot is a two dimensional lattice consisting of n^2 points, which is called the second-order quantum energy-momentum spectrum (also known as the joint spectrum or simply the second-order spectrum, see Fig. 2).

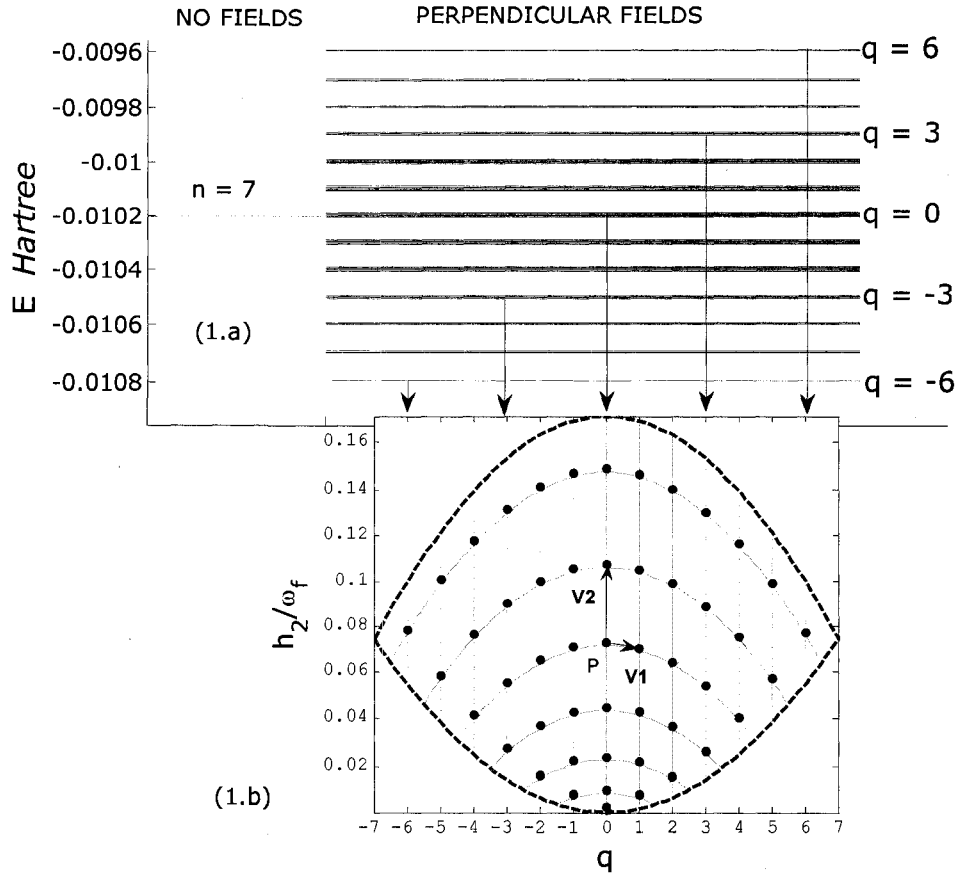


FIG.2. (color online) (a) The effects of perpendicular fields on the energy spectrum of a spinless hydrogen atom at principal quantum number $n=7$ for electric field $F = 26.5$ kV/cm and magnetic field $B = 40$ T or $\theta = 32.8^\circ$ and $\omega_f = 10^{-4}$ (ω_f has the units of a magnetic field and is reported in atomic units in all figures). The quantum basis included n manifolds 1-13. When the fields are turned on, the n^2 -degenerate n -manifolds are split into $2n-1$ equally spaced q -manifolds each containing $n-|q|$ levels. The difference between an energy level and the energy of its parent q -manifold is denoted h_2 . (b) Structure in the second order energies in an n -manifold is made visible by plotting h_2 versus q (In all lattice figures we plot h_2/ω_f with units of energy/magnetic field reported in atomic units). Contours of quantized values of classical actions are plotted in gray and form a smooth grid organizing all lattice points. $V2$ extends from P to the next lattice point along a contour of q . $V1$ extends to the nearest point along the curved contour. One may transport the pair $\{V1, V2\}$ one unit cell by simultaneously sliding the heads and tails along a set of contours until they each occupy the neighboring lattice point. For transport about any closed path inside the dashed red boundary, the lattice vectors return to themselves, indicating a completely regular lattice.

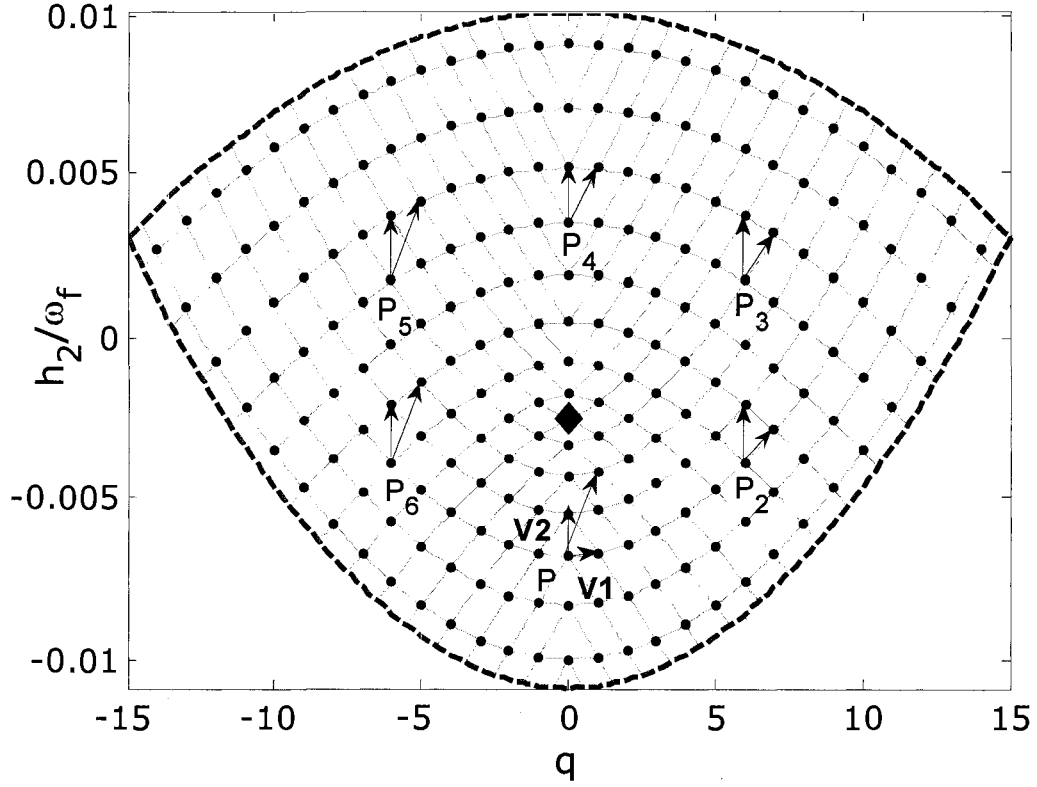


FIG.3. (color online) The monodromy in perpendicular fields. The spectrum h_2 versus q for $\chi = 0$ rad, $n = 15$, $F = 175$ V/cm, $B = 0.302$ T or $\theta = 50^\circ$ and $\omega_f = 10^{-6}$. The quantum basis included n manifolds 11-19. Two families of gray contours are plotted. The upper family passes smoothly through $q=0$ above the diamond but has a discontinuous derivative at $q=0$ below the diamond. Similarly the lower family is only smooth below the diamond. A defect is characterized by lattice vector transport of $\{\mathbf{V}_1, \mathbf{V}_2\}$ along smooth contours connecting points marked by a sequence of P's. When a complete circuit has been made \mathbf{V}_1 returns to the gray vector $\mathbf{V}_1 + 2\mathbf{V}_2$ indicating a $[1,0;2,1]$ defect.

Looking at only the blue lattice points in Fig. 2b, it is obvious to the eye that there is structure hidden "in between the points". Along with the spectrum are plotted several structures we obtained from classical perturbation theory. The lattice has a continuous boundary depicted by the dashed red curves. By construction all points lie on vertical lines of constant q . Most important, all energies can be organized into smooth curves transverse to the vertical lines. In fact, in the classical perturbation theory, n , q and the smooth curves in Fig. 2 are all quantized values of classical action variables. These actions are smooth and single valued functions of q and h_2 , defining a single smooth coordinate system covering all points inside the spectral boundary. Any spectral lattice with this property is said to form a completely regular lattice. If the spectrum in Fig. 2b were transformed into the smooth action coordinates one would find that all points lie on contiguous intersections of a rectangular grid.

The "trivial" nature of this lattice can be characterized by a matrix, which represents the effect of the transport of any pair of independent lattice vectors around any closed loop inside the spectral boundary. The lattice vectors $(\mathbf{V}_1, \mathbf{V}_2)$ at P (Fig. 2b) are unchanged by such transport, so that matrix is the unit matrix $E = [1, 0; 0, 1]$. Any such completely regular spectrum is completely described by the single-element list of matrices $\{E\}$.

In Fig. 2 we have carefully chosen critical values of θ and χ to obtain the completely regular spectrum. Not all values of θ and χ produce a regular lattice. Among the ways a hydrogen spectral lattice can fail to be totally regular are the following, discovered by Sadovskii and Cushman [11] in the case of exactly perpendicular fields $\chi = 0$. (i) There are ranges of θ at $\chi = 0$ such that the spectrum is divided into two disjoint trivial subsections, with different smooth action coordinates in each section. These subsections are divided by boundaries similar to the outer boundary of the spectrum (here denoted with dashed red curves). Examples of such disjoint spectra can be found

at perpendicular fields for $\theta < \theta_1$ and $\theta > \theta_2$ where

$$\theta_1 = \cos^{-1} \left(2^{-1/4} \right) \quad (6a)$$

$$\theta_2 = \cos^{-1} \left(\sqrt{\frac{\sqrt{6}}{2} - 1} \right) \quad (6b)$$

In such a case one could still characterize the spectrum by a single matrix $\{E\}$, which describes the effects of lattice transport within each separate region. (ii) For a certain range $\theta_1 < \theta < \theta_2$ at $\chi = 0$, Sadovskii and Cushman have shown the existence of a point defect which introduces nontrivial effects of lattice-vector transport, characterized by matrices other than the identity. The following paragraphs demonstrate how to associate a list of matrices with any such defective spectrum.

By construction, every spectrum at fixed n has points on contours of constant q , so these contours are tacitly chosen as one good coordinate on the spectrum. Defects arise when one attempts to choose another smooth coordinate function independent of q . When a lattice defect is present, the spectrum admits only locally consistent choices of smooth action contours.

In Fig. 3 we have plotted two families of contours connecting the lattice points. Given only the lattice points, one might start at the top row and draw contours similar to the upper boundary through the lattice points and continue row by row downward (as in Fig. 2b). After a certain point marked by the cyan diamond, the contours can no longer be drawn smoothly through $q = 0$, so they cannot be interpreted as level sets of a smooth action coordinate everywhere on the spectrum. Similarly, starting at the lower boundary, the lattice points are connected by smooth curves similar to the lower boundary only as far as the diamond marker. Neither of these choices can be used for smooth coordinates on the entire spectrum. However, one can find locally smooth contours in any region excluding the cyan diamond by considering two such choices. The spectrum is said to be locally trivial, or has a locally regular lattice, with a defect

associated with the cyan diamond such that this spectrum requires at least two smooth action charts [22]. The point source of the defect, marked by the cyan diamond, is called a monodromy center.

The local triviality allows a well defined notion of lattice vector transport for circuits on the spectrum. One may characterize the defect by transport around any loop encircling the diamond. In Fig. 3, begin at point P and choose the lower family of contours as locally smooth contours connecting the lattice points in a region about P . \mathbf{V}_2 extends from lattice point P to the next neighbor along a contour of constant q . \mathbf{V}_1 extends to the nearest neighbor along the curved contour of the lower family. Slide the heads and tails of these two vectors along locally smooth contours (including contours of constant q) into neighboring lattice points until an entire counterclockwise circuit about the cyan diamond has been made. Transport of the two vectors around the entire counterclockwise circuit in Fig. 3 has the result that \mathbf{V}_2 comes back to itself $\mathbf{V}_2 \rightarrow \mathbf{V}_2$ while \mathbf{V}_1 comes back to a different vector which is $\mathbf{V}_1 \rightarrow \mathbf{V}_1 + 2\mathbf{V}_2$. This transformation is equivalent to multiplication by the matrix $M_2 = [1, 0; 2, 1]$ written in the lattice basis $\{\mathbf{V}_1, \mathbf{V}_2\}$ at P .

$$M_2 = \begin{bmatrix} 1 & 0 \\ 2 & 1 \end{bmatrix}, \{\mathbf{v}_1, \mathbf{v}_2\} = \left\{ \begin{bmatrix} 1 \\ 0 \end{bmatrix}, \begin{bmatrix} 0 \\ 1 \end{bmatrix} \right\} \quad (7)$$

This M_2 defect was predicted by Sadovskii and Cushman for perpendicular fields.

If vectors are transported about any "trivial loop" in Fig. 3 (one which does not encircle the diamond) one recovers the transformation E . Thus, there are two independent counterclockwise circuits present in the spectrum in Fig. 3. They act as a basis for any circuit on the spectrum. For example, a circuit consisting of twice around the cyan diamond and once about a trivial loop results in the transformation $M_2 M_2 E = [1, 0; 4, 1] = M_4$, which may also be obtained by the obvious matrix multiplication. Also, each counterclockwise circuit has an inverse which is the same curve traversed in the opposite sense. For example if the circuit in Fig. 3 is traversed in a

clockwise sense, the result is the transformation $M_2^{-1} = [1, 0; -2, 1] = M_{-2}$.

Thus, to each quantum spectrum is associated a list of matrices, one for each basis-circuit. The spectrum in Fig. 2 belongs to a family of spectra which are characterized by the single-element list $\{E\}$, while spectra like that in Fig. 3 would be characterized by a two-element list $\{E, M_2\}$.

II. NEAR-PERPENDICULAR FIELDS

We extend the earlier discoveries by considering the case of nearly-perpendicular fields, such that $|\chi|/\omega_f n^3 < 1$, at all electric and magnetic field ratios θ . Much of the organization of the spectrum at perpendicular fields is retained into the near-perpendicular region; in particular the n and q clustering of the energy levels remains intact, allowing the same construction of spectral lattices. However, the second-order structure of the spectrum changes considerably. The effect of nonzero $|\chi|$ is to introduce several classes of spectra characterized by different lattice defects.

Using classical perturbation theory we have reduced the full classical Hamiltonian (Eq. 2) to a one-degree-of-freedom effective Hamiltonian defined on a surface having the topology of a sphere (details appear in part IV). For $|\chi|/\omega_f n^3 \ll 1$, contours of this effective Hamiltonian give an accurate description of the structure of the spectrum, including the sources of lattice defects, and quantization of action for this effective Hamiltonian gives an accurate approximation for almost all eigenvalues.

Using this effective Hamiltonian, we have mapped out all lattice defects observable in the near perpendicular region. The results are shown in Fig. 4. The blue lines demarcate six regions in the parameter space. Each region contains a family of spectra with common lattice defect structure. A characteristic list of matrices and a plot of a typical spectrum's classical structure appear in each zone. The spectra and matrix lists appearing in the lower margin along the θ axis are for the case of exactly perpendicular

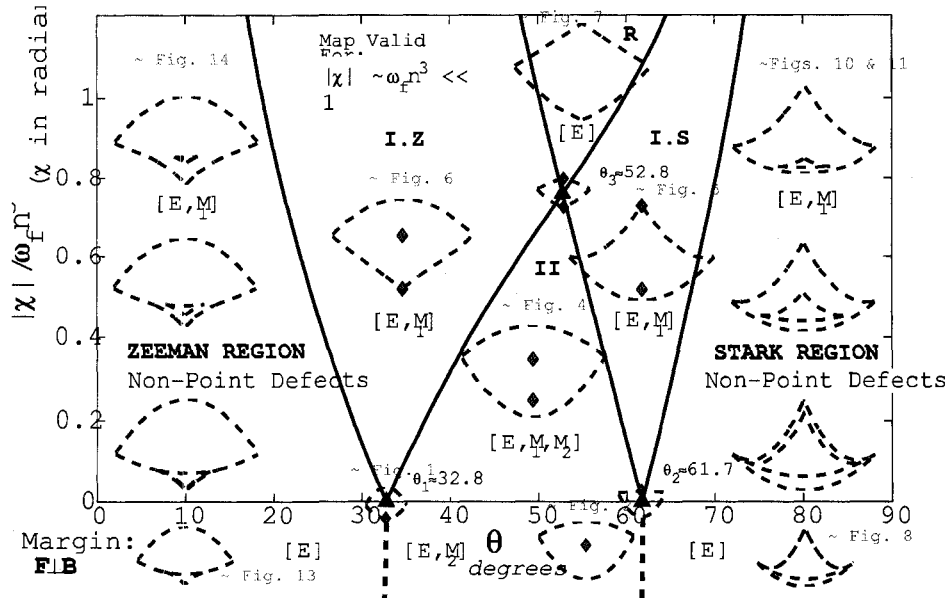


FIG. 4: (color online) A map of spectral structure and lattice defects for all near-perpendicular field configurations. All field magnitude ratios are covered on the horizontal axis by Eq. 5 with $0^\circ \leq \theta \leq 90^\circ$, with pure magnetic field at $\theta = 0^\circ$ and pure electric field at $\theta = 90^\circ$. $\pi/2 - \chi$ is the angle in radians between the electric and magnetic fields, with perpendicular fields $\chi = 0$ along the lower margin of the map. For $0 < |\chi| \lesssim \omega_f N^3 \ll 1$, the blue lines demarcate six regions with distinct spectral types. In each region, depictions of the classical structure of typical spectra appear along with a bracketed list of matrices indicating the quantum spectral lattice classification. The matrices describe the effects of lattice vector transport about closed circuits.

fields $\chi = 0$.

We examine each of the spectral structures in the sections below.

A. Region II: Bifurcations from the Perpendicular Monodromy Interval

As discussed earlier, at perpendicular fields, for any θ such that $\theta_1 < \theta < \theta_2$, the spectrum contains a single M_2 point defect (Fig. 3). As the fields are displaced from perpendicular by increasing $|\chi|$, this point bifurcates into two distinct $M_1 = [1, 0; 1, 1]$ defect points (Fig. 5).

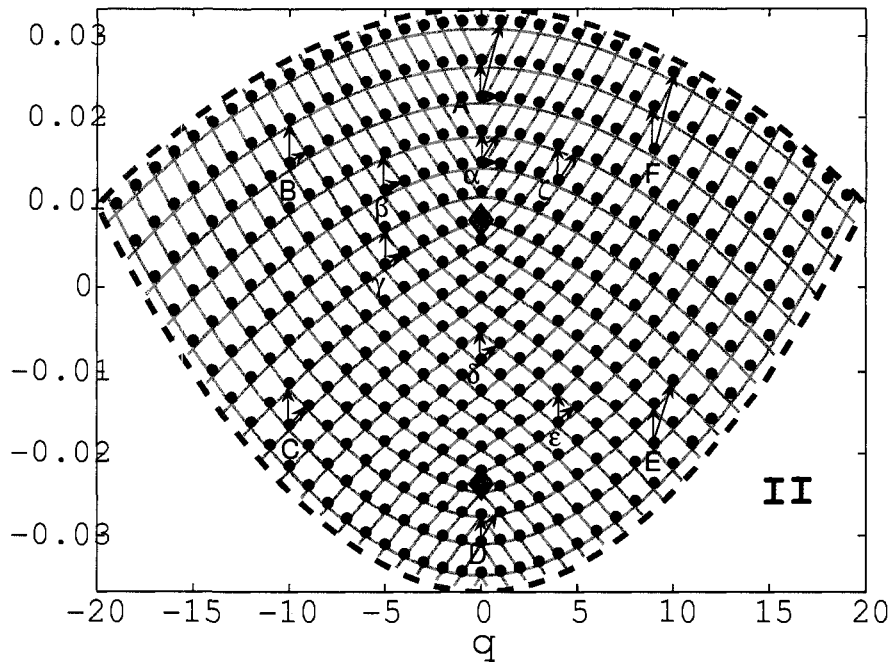


FIG. 5: (color online) Type II spectrum. The spectrum h_2 versus q for $\chi/\omega_f n^3 = 0.2$, $n = 20$, $F = 146V/cm$, $B = 0.302T$, or $\theta = 50^\circ$ and $\omega_f = 10^{-6}$. The quantum basis included n manifolds 18–22. The blue circular dots are derived from quantum calculations, while all other structures were derived from classical perturbation theory and semiclassical quantization of actions. This spectrum is obtained from one similar to Fig. 3 by tilting the fields from perpendicular. A point defect at perpendicular fields bifurcates into the two point defects shown above for non-zero χ . Two independent closed contours are marked by sequences of letters. A $[1, 0; 2, 1]$ defect is characterized by lattice vector transport of $(\mathbf{V}_1, \mathbf{V}_2)$ along locally smooth action contours connecting points marked by the Latin letter cycle $ABCDEF A$. This circuit encircles both point defects and after a complete circuit has been made, \mathbf{V}_1 returns to the vector $\mathbf{V}_1 + 2\mathbf{V}_2$ depicted in gray at A . A $[1, 0; 1, 1]$ defect is characterized by transport of $(\mathbf{V}_1, \mathbf{V}_2)$ along smooth contours connecting points marked by the sequence of Greek letters $\alpha\beta\gamma\delta\epsilon\zeta\alpha$. When a complete circuit has been made \mathbf{V}_1 returns to the vector $\mathbf{V}_1 + \mathbf{V}_2$ depicted in gray at α .

$$M_1 = \begin{bmatrix} 1 & 0 \\ 1 & 1 \end{bmatrix} \quad (8)$$

In Fig. 5 we mark two of the three possible nontrivial counterclockwise circuits by sequences of Latin and Greek letters. The transport of \mathbf{V}_1 and \mathbf{V}_2 about the sequence of Latin letters yields the M_2 defect while transport about the sequence of Greek letters

yields M_1 . There are no other independent nontrivial circuits, for if we traverse the Latin loop and then make a clockwise circuit about the Greek loop, the total circuit is equivalent to a single circuit about the lower diamond marker. Thus this spectrum can be classified by the list $\{E, M_1, M_2\}$. Similar spectra are obtained from any perpendicular spectrum in the interval $\theta_1 < \theta < \theta_2$ by tilting χ . We call this region II.

B. Regions I.S and I.Z

If we start with a spectrum from region II (Fig. 5) and continue to tilt the field angle χ at fixed θ (with $\theta_1 < \theta < \theta_2$), then the defect points change energy until one (or both) reaches the boundary of the second-order spectrum. At larger θ (closer to Stark), the higher defect reaches the upper boundary first, while at smaller θ (closer to Zeeman), the lower defect reaches the lower boundary first. Both defects will join the boundary simultaneously at $\chi = \chi_3$ only if $\theta = \theta_3$ where

$$\chi_3 = \pm 3^{-1/4} \omega_f n^3 \approx \pm 0.7598 \omega_f n^3 \quad (9a)$$

$$\theta_3 = \cos^{-1} \left(\sqrt{\frac{\sqrt{3}-1}{2}} \right) \approx 52.771^\circ \quad (9b)$$

If $\theta_3 < \theta < \theta_2$ then the upper defect point from region II joins the upper boundary to yield a spectrum with a single M_1 defect, and therefore characterized by $\{E, M_1\}$. We call this region I.S. A representative spectrum is depicted in Fig. 6.

Another region with $\{E, M_1\}$ structure may be reached by starting in region II with $\theta_1 < \theta < \theta_3$ and increasing $|\chi|$. In this case, the lower defect from region II will join the lower boundary, again yielding a spectrum with a single M_1 defect.

Analogous transitions of the type II spectra occur when the field strength ratio θ is increased (II \rightarrow I.S) or decreased (II \rightarrow I.Z) at fixed χ with $0 < |\chi| < \chi_3$. These transitions occur at the values of θ marked by the blue lines demarcating region II from its neighboring regions on the map in Fig. 4.

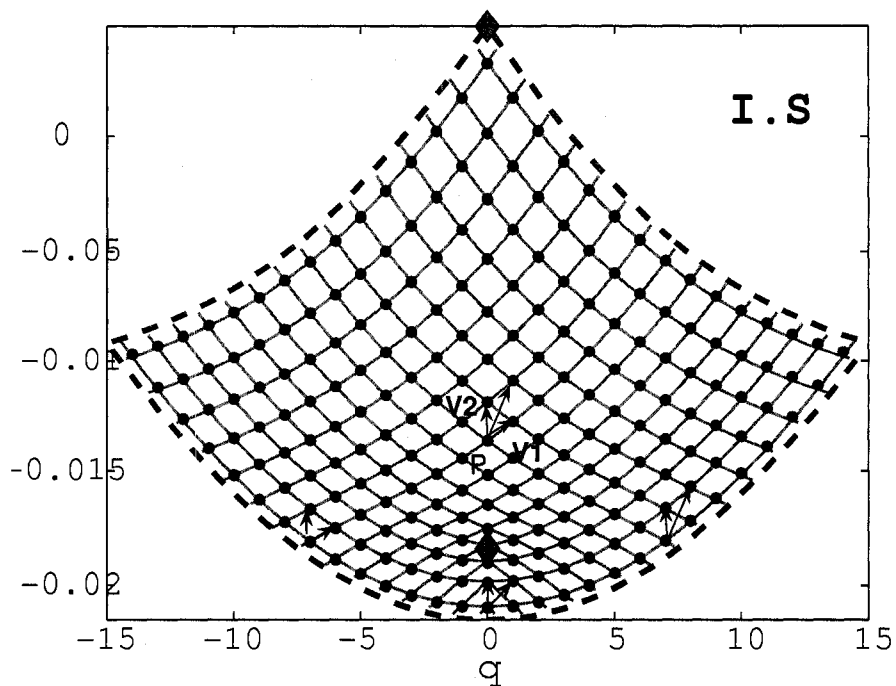


FIG. 6: (color online) Type I.S spectrum. The spectrum h_2 versus q for $\chi/\omega_f n^3 = 0.6$, $n = 15$, $F = 207V/cm$, $B = 0.199T$, or $\theta = 65^\circ$ and $\omega_f = 10^{-6}$. In this calculation, and all calculations at $n = 15$, the quantum basis included n manifolds 11 – 19. By considering the effects of lattice vector transport a type I.S spectrum would be classified $\{E, M_1\}$. This spectrum may be obtained from a type II spectrum with $\theta_3 < \theta < \theta_2$ by increasing $|\chi|$ at constant θ . At a critical $|\chi|$, the upper point defect from a region II spectrum joins the upper boundary leaving a single M_1 defect.

C. Completely Regular Region R

If θ is exactly equal to θ_3 , we pass directly from a type-II spectrum to a completely regular spectrum by increasing $|\chi|$. We may also recover a completely regular spectrum from a I.S or I.Z type by varying θ and $|\chi|$ such that the single defect point is moved to the boundary of the spectrum. The values of θ and $|\chi|$ for which this occurs are marked on the map by the blue lines separating the I.S and I.Z regions from their neighbor at large $|\chi|$ (Fig. 4). For all spectra in the R region, every closed lattice vector transport loop leaves the lattice vectors unchanged. We label this featureless region R (for completely regular). Any spectrum in this region may be covered with a single

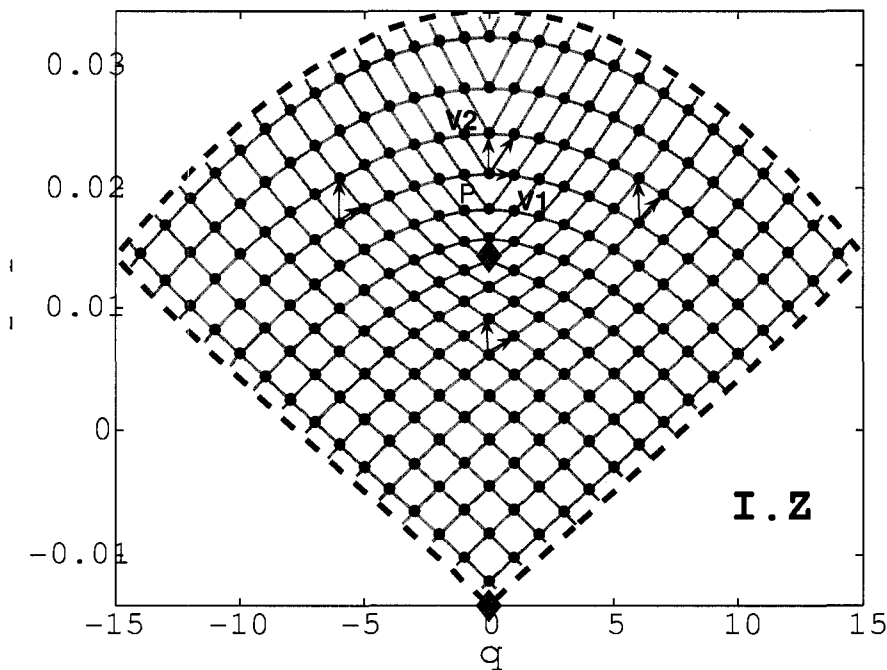


FIG. 7: (color online) A type I.Z spectrum. The spectrum h_2 versus q for $\chi/\omega_f n^3 = 0.6$, $n = 15$, $F = 131V/cm$, $B = 0.385T$, or $\theta = 35^\circ$ and $\omega_f = 10^{-6}$. This spectrum may be obtained from one similar to Fig. 5 with $\theta_1 < \theta < \theta_3$ by increasing $|\chi|$. At a critical $|\chi|$, the lower point defect from the type II spectrum joins the lower boundary of the spectrum. The upper $[1, 0; 1, 1]$ defect remains present.

action chart, and all R spectra are classified by the list $\{E\}$.

D. Stark Region: Bifurcations from Perpendicular Fields near the Stark Limit

The spectra in the Stark region possess a more complex structure. To understand the behavior here, we first re-examine the second order structure in perpendicular fields, previously explained by Solov'ev (Ref. [8]) but using our semiclassical framework. For perpendicular fields the second order spectrum consists of three families of states (Fig. 9). States at low energy are nondegenerate, while states at high energy are very nearly doubly degenerate. The degenerate states are separated from the nondegenerate states by a classical boundary.

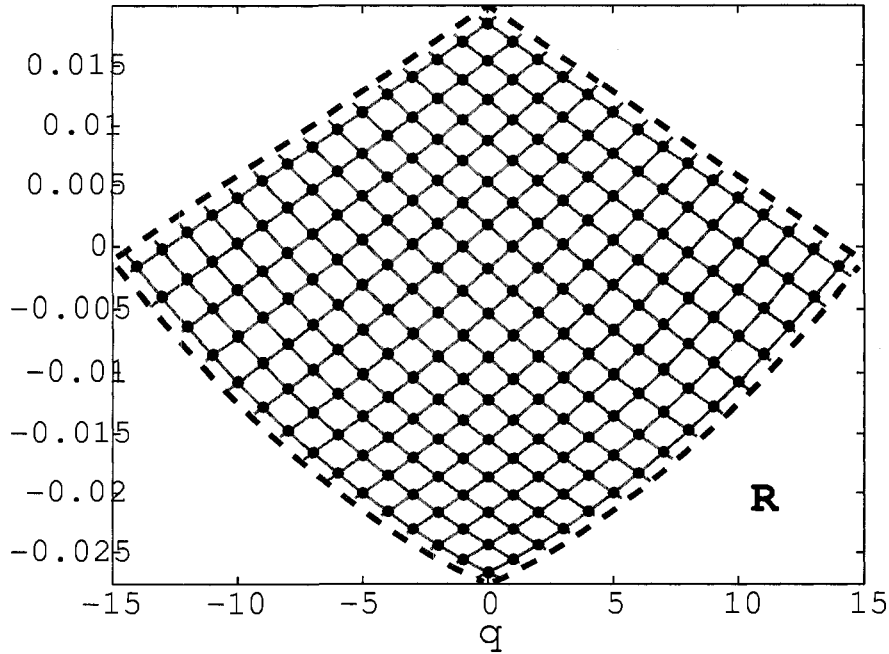


FIG. 8: (color online) A type R spectrum. The spectrum h_2 versus q for $\chi/\omega_f n^3 = 1$, $n = 15$, $F = 187V/cm$, $B = 0.27T$, or $\theta = 55^\circ$ and $\omega_f = 10^{-6}$. Spectra in the R region are completely regular and admit a single smooth action chart. An R spectrum may be obtained from a type II spectrum with $\theta = \theta_3$, by increasing $|\chi|$, or from a type I.S or I.Z spectrum by varying $(\theta, |\chi|)$ along a path which crosses their respective upper borders as indicated by the blue lines on the map in Fig. 4.

To understand this structure let us discuss the reduced Hamiltonian h_2 we derived from classical perturbation theory (details appear in part IV). The reduced Hamiltonian is a π -periodic function of an angle δ_W ($-\pi/2 < \delta_W \leq \pi/2$), and its conjugate momentum W . It also depends parametrically on the classical principal action $N = n\hbar$ and a classical action variable $Q = q\hbar$ corresponding to the q clustering integer ($\hbar = 1$). In the reduced system, N and Q are both constants of the motion. For each $|Q| < N$, the reduced phase space (W, δ_W) has the topology of the surface of a sphere with W related to a latitude, and δ_W related to a longitude. The values of this Hamiltonian describe the classical second order energy, and its derivatives give the motion of the system point on the surface of the sphere. The maximum and minimum values that h_2

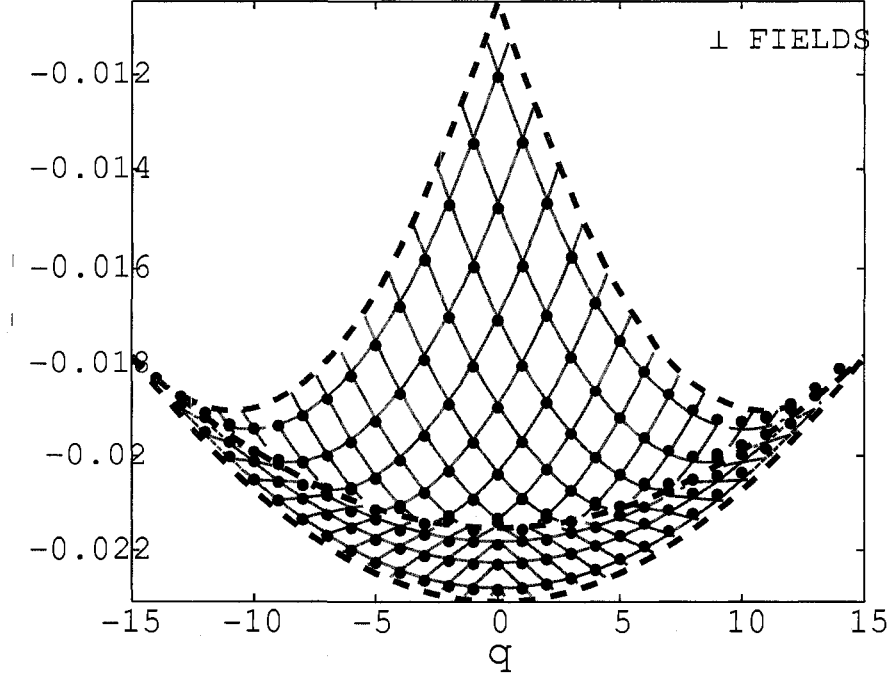


FIG. 9: (color online) A perpendicular fields spectrum near the Stark limit. The spectrum h_2 versus q for $\chi = 0$, $n = 15$, $F = 225V/cm$, $B = 0.082T$, or $\theta = 80^\circ$ and $\omega_f = 10^{-6}$. Spectra with $\chi = 0$, and $\theta_2 < \theta < 90^\circ$ are composed of two disjoint regular regions. All quantum states in the upper triangular region are doubly degenerate with a slight splitting due to tunneling, while all states in the lower crescent shaped region are nondegenerate. The boundary between the two regions marks the energy of a saddle point in the reduced second order Hamiltonian h_2 at each $Q = q$.

assumes on the sphere (at a given $N = n$, $Q = q$) are the upper and lower dashed red boundaries that encase all the quantum spectra plotted in this paper.

Contour plots of this reduced Hamiltonian in the Stark region are shown in a planar projection in Fig. 10.A and 10.B for the case $N = 15$, $Q = 0$ and (A) perpendicular fields, (B) $\chi = 0.8n^3\omega_f$. Darker regions indicate lower energies, blue markers indicate fixed points of the Hamiltonian, and the red contour is a separatrix having the energy of an x-point. The separatrix divides the classical phase space structure into 3 families of energy level sets. At perpendicular fields (A), the Hamiltonian is symmetric about the "equator" $W = 0$. The low energy family is localized in W symmetrically about

the equator and so we refer to this family as the equatorial family. The two high energy families are localized in W in either the northern ($W > 0$) or southern ($W < 0$) hemispheres, so we refer to them as the "northern" or "southern" families respectively.

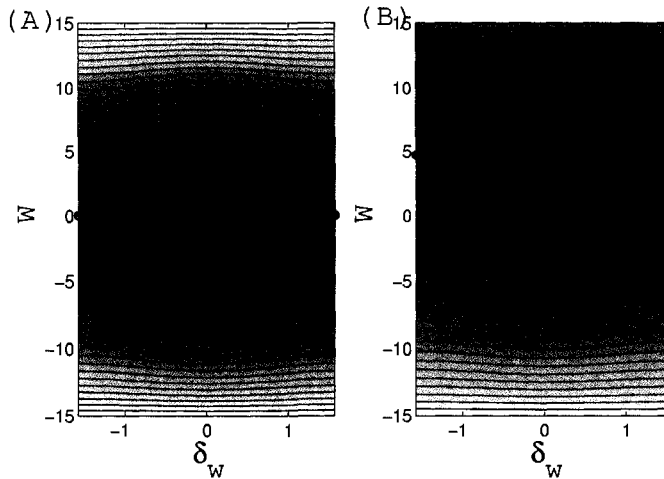


FIG. 10: (color online) Contours of the reduced second order Hamiltonian $h_2(W, \delta_W; n, Q)$ at $n = 15$, $Q = 0$, in the Stark region with $\theta = 80^\circ$ and (A) $\chi = 0$ at perpendicular fields and (B) $\chi/\omega_j n^3 = 0.8$. This Hamiltonian is a function on a spherical phase space such that W is related to a latitude, and δ_W to a longitude. The contour plots are then to be interpreted as a planar projection of the reduced phase space, with left and right edges identified and top and bottom boundaries corresponding to north and south poles respectively. Darker regions indicate lower energies; blue points indicate fixed points and an x-point separatrix is plotted in red. In addition to the o-point in the center of the dark region, two additional o-points are present but not marked at the north and south poles. The separatrix divides the classical contours into 3 families of states. (A) At perpendicular fields the reduced Hamiltonian is symmetric about the equator $W = 0$. At low energies are the "Equatorial" states localized about $W = 0$. At high energies, "northern" states are localized at positive W , and "southern" states are localized at negative W . (B) When the fields are tilted the symmetry is broken such that both the phase space area and the energy range occupied by the northern states are reduced while those of the southern states are increased. The structure of the contours of h_2 is similar for all Q less than a certain $Q_{critical}(N, \theta, \chi)$.

Using a primitive semiclassical approximation, quantum states are associated with contours having half-integral values of an action variable related to the (W, δ_W) phase space area. At perpendicular fields, the reduced Hamiltonian is always symmetric in W . Inspection of Fig. 10A reveals that all level sets with energies greater than that of the x-point appear as disjoint pairs of contours, one in the north and one in the

south. If a northern contour with energy $h_2 = E_2$ has a quantized value of the action variable, then from the W symmetry, it follows that there is a southern contour with the same energy and action value. Thus, at all allowed energies greater than that of the separatrix we expect to find two nearly degenerate quantum states. At each energy below the separatrix, there exists only a single closed contour so we expect the corresponding quantum states to be non-degenerate. This three-family structure, due to the presence of the x-point, exists in the contours of the reduced Hamiltonian for all $|Q|$ less than a certain critical value $Q_{critical}(N, \theta, \chi)$. Therefore we expect to find the quantum degeneracy implied by such a structure for all $|q| < Q_{critical}(N = n, \theta, \chi)$.

Looking back at Fig. 9 one identifies the non-degenerate states in the lower crescent as the equatorial states. The boundary between the crescent and triangular regions marks the energy of the x-point separatrix on each reduced phase space having $|Q| < Q_{critical}(N = 15, \theta = 80^\circ, \chi = 0) = 14.06$. The upper triangular region is filled with pairs of nearly degenerate states, with slight splitting, greatest near the x-point energy. This small splitting arises from quantum tunneling, so the resulting states are symmetric and antisymmetric combinations of northern and southern states.

When the angle between the fields is changed, the symmetry in the Hamiltonian between the northern and southern hemispheres is broken. If we start with the contours in Fig. 10.A and tilt the fields from perpendicular, we introduce a small term proportional to $-\chi W$, producing contours like those plotted in Fig. 10.B at $\chi = 0.8n^3\omega_f$. By comparing these contours with those in Fig. 10.A we see that the energy range and phase space area occupied by southern states increased while the energy range and phase space area of the northern states decreased.

Since each quantum state corresponds to an energy contour having a quantized action, we expect to find in the spectrum fewer northern states occupying a smaller energy range and more southern states occupying a larger energy range. There is similar behavior for all $|q| < Q_{critical}$. Stark region spectra with tilted fields are shown

in Figs. 11 and 12. The southern states are associated with the gray action contours which occupy the whole energetically allowed region of the spectrum. The northern states are associated with the orange action contours which are confined to the smaller triangular region. The lower boundary of this triangle marks the energy of the x-point for each $|Q|$ less than $Q_{critical}(N, \theta, \chi)$. The upper boundary is the maximum energy of the northern contours. Therefore the gray action contours associated with the southern states pass smoothly through the upper boundary. Neither northern nor southern actions can be smoothly continued through the x-point (lower) boundary of the inner triangle.

In contrast to the orange contours, which represent a single valued action variable, the gray curves represent an intrinsically multivalued action. This is evident in Fig. 12 where we consider the effects of lattice vector transport along gray action contours on a closed loop. We obtain an M_1 lattice defect whenever the lower boundary of the small triangular region is enclosed by a single counterclockwise circuit.

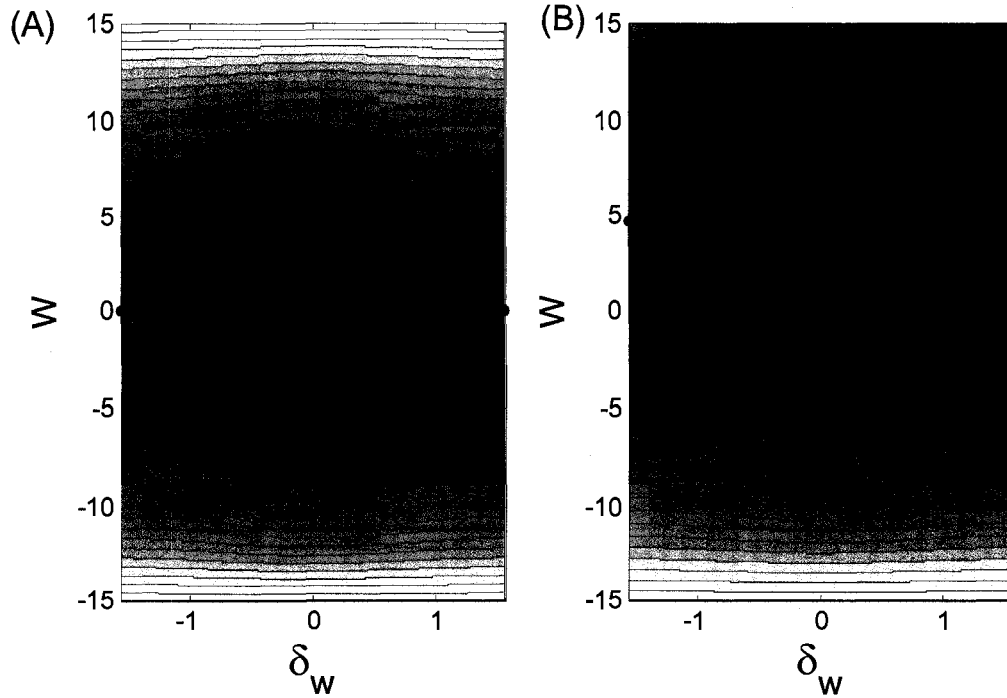


FIG.10. (color online) Contours of the reduced second order Hamiltonian $h_2(W, \delta_w; n, Q)$ at $n = 15$, $Q = 0$, in the Stark region with $\theta = 80^\circ$ and (A) $\chi=0$ at perpendicular fields and (B) $\chi/\omega_{pe}^3 = 0.8$. This Hamiltonian is a function on a spherical phase space such that W is related to a latitude, and δ_w to a longitude. The contour plots are then to be interpreted as a planar projection of the reduced phase space, with left and right edges identified and top and bottom boundaries corresponding to north and south poles respectively. Darker regions indicate lower energies; blue points indicate fixed points and an x-point separatrix is plotted in red. In addition to the o-point in the center of the dark region, two additional o-points are present but not marked at the north and south poles. The separatrix divides the classical contours into 3 families of states. (A) At perpendicular fields the reduced Hamiltonian is symmetric about the equator $W = 0$. At low energies are the “Equatorial” states localized about $W = 0$. At high energies, “northern” states are localized at positive W , and “southern” states are localized at negative W . (B) When the fields are tilted the symmetry is broken such that both the phase space area and the energy range occupied by the northern states are reduced while those of the southern states are increased. The structure of the contours of h_2 is similar for all Q less than a certain $Q_{\text{critical}}(N, \theta, \chi)$.

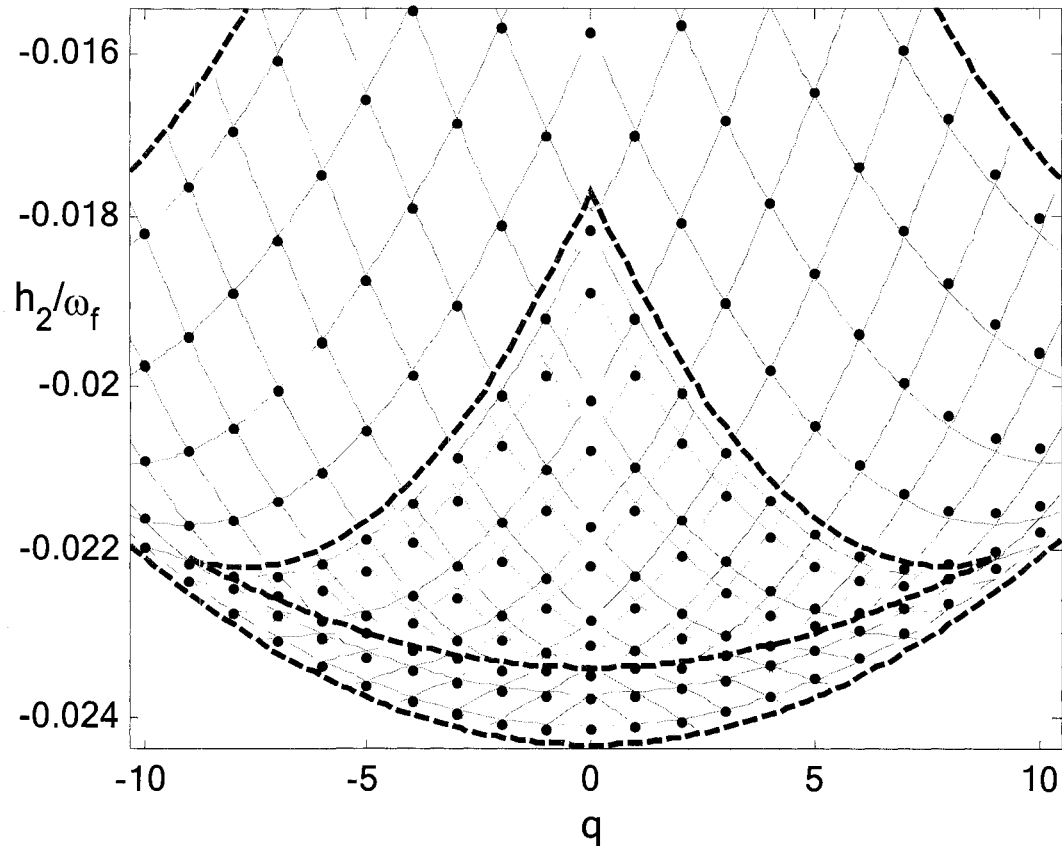


FIG.11. (color online) A portion of a Stark region spectrum; h_2 versus q for $|\chi|/\omega_f n^3 = 1$, $n = 15$, $F = 226$ V/cm, $B = 0.0654$ T or $\theta = 82^\circ$ and $\omega_f = 10^{-6}$. A triangular sub-area of all Stark region spectra with $|\chi| > 0$ contains two families of states with overlapping energy ranges. The states located at the intersections of the orange contours are the northern states, while those at the gray intersections are the southern states. The orange contours exist only within the inner triangular region. The gray contours cover the entire classically allowed region passing smoothly through the upper boundaries of the smaller triangle. Neither northern nor southern contours pass smoothly through the lower boundary.

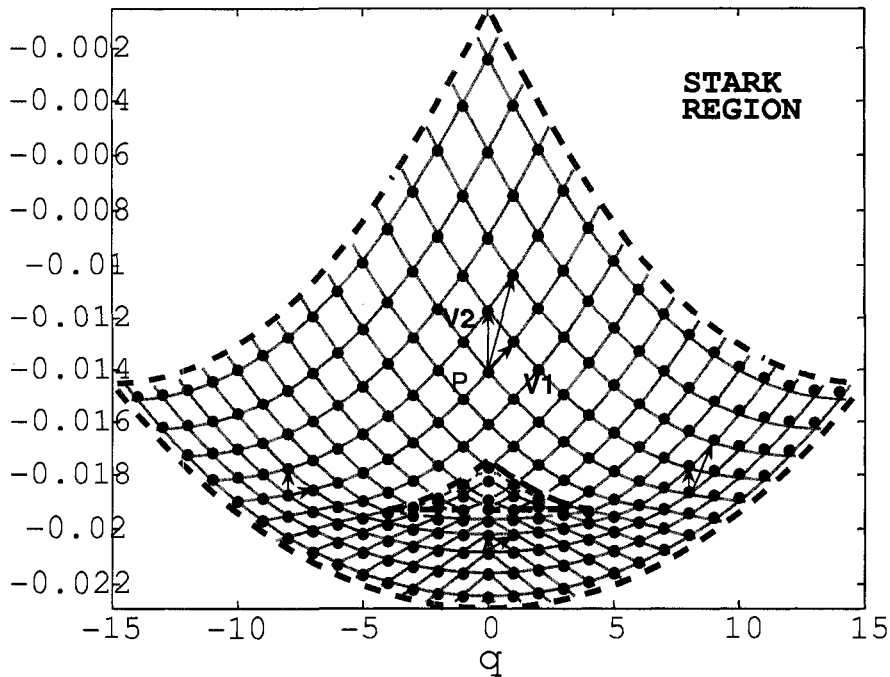


FIG. 12: (color online) Stark region, The spectrum h_2 versus q for $|\chi|/\omega_f n^3 = 0.6$, $n = 15$, $F = 219V/cm$, $B = 0.137T$ or $\theta = 73^\circ$ and $\omega_f = 10 - 6$. All Stark region spectra with $|\chi| > 0$ contain a smaller triangular region containing two families of states. The lower boundary of the smaller triangular region acts as a defect source. Lattice vector transport about any counterclockwise closed loop encircling the lower boundary of the inner triangle displays the presence of an M_1 defect.

Finally, returning to Fig. 4, we have plotted in the Stark region a series of classical skeletons of quantum spectra depicting the changes resulting from tilting the fields from perpendicular.

E. Zeeman Region: Bifurcations from Perpendicular Fields near the Zeeman Limit

Spectra in the Zeeman region are also composed of multiple families of states and possess structure which is similar to that we found in the Stark region.

In Fig. 13 we plot the contours of a typical reduced Hamiltonian in the Zeeman

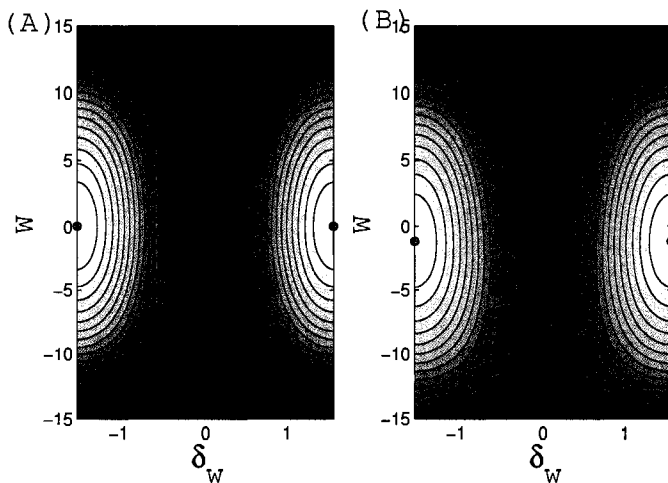


FIG. 13: (color online) Contours of the reduced second order Hamiltonian $h_2(W, \delta_W)$ at $n = 15$, $Q = 0$, in the Zeeman region where $\theta = 15^\circ$ and (A) perpendicular fields ($\chi = 0$) and (B) $\chi/\omega_f n^3 = 0.7$. Darker regions indicate lower energies; blue points indicate fixed points and an x-point separatrix is plotted in red. There are also unmarked o-points located at the north and south poles of both spheres. The separatrix divides the classical contours into three families of states. At high energies are the "Equatorial" states, and at low energies are the "northern" states at positive W and "southern" at negative W . (A) At perpendicular fields the Hamiltonian is symmetric about the equator $W = 0$. (B) When the fields are tilted the symmetry is broken such that both the phase space area and the energy range occupied by the southern states are decreased while those of the northern states are increased. The structure of the contours of h_2 is similar for all Q less than a certain $Q_{critical}(N, \theta, \chi)$.

region at $Q = 0$ and (A) perpendicular fields, or (B) near-perpendicular fields.

At perpendicular fields the Hamiltonian is symmetric in W and an x-point separatrix divides the contours into three families. In the Zeeman region, the high energy states are equatorial and non-degenerate. In the northern and southern hemispheres are low energy degenerate states for all $Q < Q_{critical}$. Notice that the majority of the phase space is occupied by the nondegenerate equatorial states.

In Fig. 14 we plot a quantum spectrum from the Zeeman region with perpendicular fields. Residing inside the small triangular protrusion are the low energy states. These states are very nearly doubly degenerate with their slight splitting greatest near the red classical boundary which divides the spectra in two. All states in the larger turtle-shaped portion of the spectrum are non-degenerate. We identify the states in the small

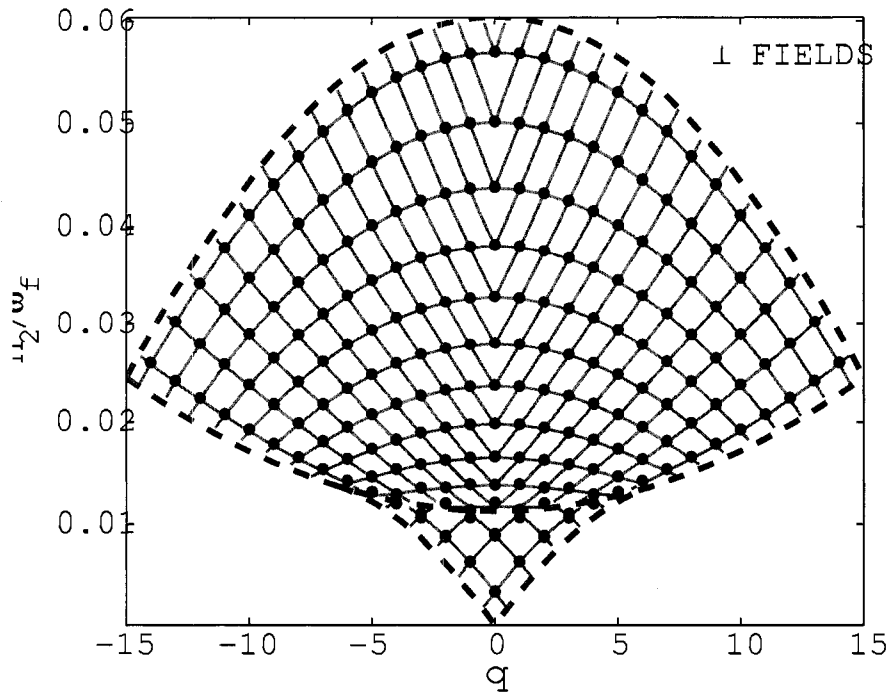


FIG. 14: (color online) A perpendicular fields spectrum near the Zeeman limit; h_2 versus q for $\chi = 0$, $n = 15$, $F = 39.7V/cm$, $B = 0.463T$ or $\theta = 10^\circ$ and $\omega_f = 10^{-6}$. Spectra with $\chi = 0$, and $0 < \theta < \theta_1$ are composed of two disjoint regular regions. All quantum states in the lower triangular protrusion are doubly degenerate with a slight splitting due to tunneling, while all states in the upper turtle-shaped region are nondegenerate. The boundary between the two regions marks the energy of a saddle point in the reduced second order Hamiltonian h_2 at each $|q| < Q_{critical}$.

protrusion as symmetric and antisymmetric linear combinations of the northern and southern states. We also identify the non-degenerate states as the equatorial family separated from the nearly degenerate states by the energy of the x-point separatrix at each $|q| < Q_{critical}$.

When the fields are tilted the symmetry is again broken by an additional term proportional to $-\chi W$. In (B) we see that when χ is increased the northern states acquire a larger energy range and more phase space area while the southern states are depleted of phase space area and span a reduced energy range. Since there is similar structure for all reduced Hamiltonians with $|Q| < Q_{critical}$, the features of the near perpendicular

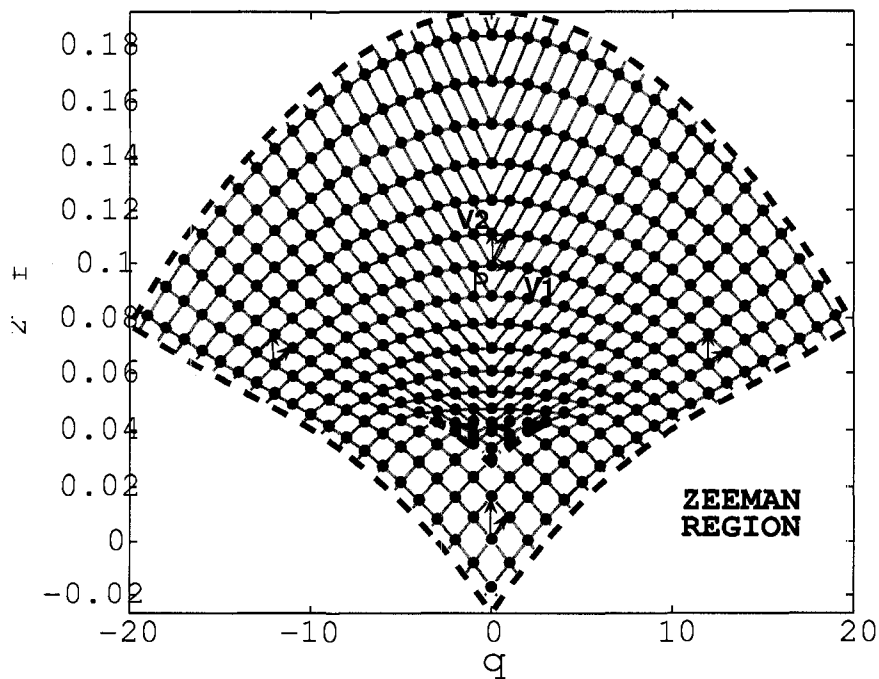


FIG. 15: (color online) The spectrum h_2 versus q for $\chi/\omega_f n^3 = 1$, $n = 20$, $F = 30V/cm$, $B = 0.463T$ or $\theta = 10^\circ$ and $\omega_f = 10^{-6}$. The quantum basis included n manifolds 18 – 22. The red triangular region centered about $q = 0$ and $h_2 = 0.04$ contains two families of states and the upper boundary acts as a source for a $[1, 1; 0, 1]$ defect. Lattice vector transport of $(\mathbf{V}_1, \mathbf{V}_2)$ along smooth contours connecting points marked by vector pairs counterclockwise about the degenerate region causes \mathbf{V}_1 to return to the gray vector $\mathbf{V}_1 + \mathbf{V}_2$.

quantum spectra in the Zeeman region (Fig. 15) are interpreted as follows.

The southern states are confined to the small triangular region bounded by two classical boundaries. The lower boundary marks the minimum energy of the southern contours, while the upper boundary marks the energy of the x-point separatrix. The action associated with the southern family is depicted by orange contours and is single valued and smooth. The northern family is present in the entire energetically allowed region of the spectrum and the associated action is depicted by gray contours. This action is intrinsically multivalued, as is illustrated in Fig. 15, where lattice vector transport along the gray contours produces an M_1 defect for any closed loop which encircles the upper boundary of the inner triangle.

III. CONCLUSION

We have examined the quantum energy spectrum of hydrogen in weak, nearly-perpendicular electric and magnetic fields using both classical and quantum descriptions. We found that the presence of a phenomenon known as monodromy, previously predicted by Sadovski and Cushman to be present in the case of exactly perpendicular fields for a limited range of field strength ratios, not only persists in near perpendicular fields, but assumes new manifestations over a wide range of field ratios. Using classical mechanics we have mapped out the parameter space and found that it is divided into six distinct regions. Each region is identified by a lattice defect structure present in the energy spectrum which is associated with the classical phenomenon known as monodromy. Variation of field strengths and angles leads to transitions between the different defect structures. We have found that a point defect, which was previously predicted to exist at perpendicular fields, undergoes a bifurcation into two distinct point defects as the fields are tilted. We also showed that non-point defects arise when fields are tilted from perpendicular near the Stark and Zeeman limits. In part IV we will present the entire theory in detail.

Part III

Static Monodromy and Multivalued Classical Action Variables

In this section we present the mathematical connection between multivalued classical action variables and the topology of level sets in classical phase space. We also define the concept of a primitive action and show that a simple relationship exists between these primitive actions and the smooth but multivalued classical action variables. The reader who wishes to skip this section will not have trouble following the discussions in part IV where the primitive actions are constructed directly from the classical system.

IV. OVERVIEW

In classical integrable systems with k degrees of freedom, there are k functions $f_i(p, q)$ which are conserved on every trajectory. Phase space is the union of joint level sets of these functions, [i.e. $f_i(p, q) = c_i$, $i = 1 \dots k$] with each level set labeled by the values of the constants of the motion, (c_1, c_2, \dots, c_k) . The space of all allowed values $\{c_i, i = 1 \dots k\}$ is the *classical spectrum*. If the functions $f_i(p, q)$ are independent at every point in a compact connected component of a level set, then that component is a k -torus. However, in some systems, certain level sets are not collections of disjoint k -tori. Those level sets which are k -tori may form: (a) a single simply-connected family; (b) a single multiply connected family; (c) two or more disjoint families, each of which may be either simply or multiply connected. In a small neighborhood of phase space about any one torus, k smooth action variables may be constructed, providing an alternative labeling for the tori. These smooth action variables are locally single-valued functions of the constants of the motion. However, if a family of tori is multiply connected, smooth continuation of

a local action variable may lead to a globally multiple-valued function on the classical spectrum. Whenever smooth continuation of an action variable around some closed loop in the classical spectrum brings that action variable back to a new value, the system is said to have “nontrivial monodromy of action and angle variables”, or simply, “monodromy”.

V. INTEGRABLE SYSTEMS AND THE EXISTENCE OF LOCAL SMOOTH ACTION VARIABLES

Consider a classical phase space manifold R^{2n} with the global coordinates (\mathbf{p}, \mathbf{q}) and the symplectic 2-form $\omega^2 = \sum_i dp_i \wedge dq_i$. A dynamical system constructed on such a phase space is called *integrable* if there exist n independent functions $f_i(\mathbf{p}, \mathbf{q})$ ($i = 1, \dots, n$) on phase space which have mutually vanishing Poisson brackets.

$$\{f_i, f_j\} = 0 \quad \forall i, j \quad (10)$$

At a given phase space point (\mathbf{p}, \mathbf{q}) , these functions may or may not be (i) well defined, (ii) smooth, or (iii) independent. The functions are independent at a given phase space point if their associated cotangent vectors exist, and are linearly independent at that point:

$$\sum_{i=1}^n \alpha_i df_i = 0 \Rightarrow \alpha_i = 0 \quad \forall i \quad (11)$$

If Eq. 11 is not true for any point in phase space where the f_i are well defined and smooth, then the f_i are functionally dependent at that point.

A *Joint Level Set* of the f_i is the collection of points of phase space for which:

$$\mathbf{f} = \mathbf{c} \quad (12)$$

Such a joint level set is denoted $L_{\mathbf{c}}$ and may or may not be (i) compact, or (ii) connected. Since such joint level sets are subsets of R^{2n} , $L_{\mathbf{c}}$ will be compact if it is closed and bounded.

By the implicit function theorem, if (a) the mapping \mathbf{f} is continuously differentiable in a neighborhood of a phase space point \mathbf{z} for which $\mathbf{f}(\mathbf{z}) = \mathbf{c}$, and (b) the components of \mathbf{f} are functionally independent at \mathbf{z} , then locally the joint level set $L_{\mathbf{c}}$ is a smooth n dimensional subset of R^{2n} .

If (a) and (b) are satisfied at every point of a connected component of $L_{\mathbf{c}}$, then that component of $L_{\mathbf{c}}$ is a smooth submanifold of R^{2n} .

A. The Existence of Tori and Locally Smooth Actions

A classical theorem, found in chapter 10 of V.I. Arnold's *Mathematical Methods of Classical Mechanics* [44] proves the following assertion.

1. Classical Tori

If at every point of a compact connected component of a joint level set $\mathbf{f} = \mathbf{c}$ the following two conditions are met: (i) $\{f_i, f_j\} = 0 \forall i, j$ and (ii) $\sum_{i=1}^n \alpha_i df_i = 0 \Rightarrow \alpha_i = 0 \forall i$, then that component of the level set is diffeomorphic to an n -torus. Furthermore on some neighborhood about this torus, one can construct local canonical action and angle variables (J_i, ϕ_i) such that:

(1) Each J depends on the f_i alone

(2) Each ϕ is 2π periodic and has a linear t_i time dependence under the flow of any of the f_i (where t_i parameterizes the flow along the Hamiltonian vector field which is generated by f_i , and $\{t_i, f_i\} = 1$).

(3) The symplectic 2-form is written $\omega^2 = \sum_i dJ_i \wedge d\phi_i$

2. Smooth actions and vectors from the Period Lattice

These locally smooth action variables must be constructed in specific manner. Consider the n dimensional space $\{t_i, i = 1 \dots n\}$ of “time” parameters along the n independent and commuting Hamiltonian vector fields which are generated by the f_i . An important piece of Arnold’s proof [44] shows that for each n -torus there exist n linearly independent and non-zero vectors τ^k $k = 1, 2, \dots n$ in the space of t_i with the following significance:

(i) Starting at any point z_0 on the surface of the torus, the curve in phase space which is constructed by flowing along each of the Hamiltonian vector fields generated by the f_i for a “time” given by τ_i^k (ie: the i^{th} component of the vector τ^k) will terminate on z_0 , forming a closed curve on the surface of the torus. Let us denote the resulting n closed curves on the surface of the torus γ^k (with $k = 1, \dots n$).

(ii) Each of these curves is nontrivial and independent on the surface of the torus such that γ^k cannot be smoothly deformed to a point or any other γ^j if $k \neq j$.

Thus for each n -torus in phase space, labeled by a value of the constants of the motion \mathbf{c} there are n non-zero, linearly independent vectors τ^k in the \mathbf{t} space which generate n nontrivial independent closed curves on the surface of the n -torus. Provided that we can fix a smooth n dimensional surface $z_0(\mathbf{c})$, the vectors τ^k are smooth functions of the values of the constants of the motion $\tau^k(\mathbf{c})$. As a result, there are n nontrivial and independent curves $\gamma^k(\mathbf{c})$ on the surface of each torus which depend smoothly on the values of the constants of the motion.

One may now define n action variables in some neighborhood of any n -torus which are guaranteed [29] to be locally smooth functions of the constants of the motion.

$$J_k = \frac{1}{2\pi} \oint_{\gamma^k(\mathbf{c})} \mathbf{p} \cdot d\mathbf{q} \quad (13)$$

It is important to note that the value of the integral in this definition is invariant for homologous deformations of the curves γ^k on the surface of the torus. This follows

immediately from the Poincaré theorem because the J are constant on each torus and:

$$d(pdq) = dp \wedge dq \quad (14)$$

$$\omega^2 = dp \wedge dq = dJ \wedge d\phi \quad (15)$$

3. *Monodromy*

The n smooth actions defined in Eq. 13 cannot be defined on any component of a level set which is not an n -torus, and therefore they are not all defined for some values of the constants of the motion. When a level set that is not an n -torus (or a connected family of level sets which are not n -tori) is situated in phase space such that there exists a family of n -tori which is multiply connected, then the domain of the smooth functions J_k is multiply connected. A locally smooth function on a multiply connected domain need not be single valued (consider the function θ versus the function $\cos\theta$ defined on the unit circle). It follows that if a multiply connected family of tori exist in phase space, the system might have a multiple valued smooth action variable. Whenever a system has an action variable that is a multiple valued function of the constants of the motion, that system is said to have “monodromy”.

B. Primitive Actions

It is not always convenient to compute the τ^k as a function of the constants of the motion, and it is not the commonly used approach for constructing action and angle variables. It is far more common that action variables are constructed for separable systems using integration loops which are formed by the intersection of an n -torus with n Poincaré surfaces. We denote these loops $\gamma_{primitive}^k$ and we call the action integrals

constructed from the primitive loops, *primitive actions* .

$$J_{primitive}^k = \frac{1}{2\pi} \oint_{\gamma_{primitive}^k(c)} \mathbf{p} \cdot d\mathbf{q} \quad (16)$$

However, it turns out that these primitive actions may not be smooth functions of the constants of the motion everywhere on their domain. Where these primitive actions are not smooth they may be smoothly continued using a simple method.

If on every n-torus, we fix a basis of closed curves $\gamma_{fundamental}^k$ for the fundamental homology class of the n-tori, the homology class of any closed curve on the surface of a torus may be expanded in terms of that basis. In particular, both the γ^k generated by the τ^k , and the $\gamma_{primitive}^k$ have the expansions:

$$\gamma^j = \sum_{p=1}^n m_p^j \gamma_{fundamental}^p \quad (17a)$$

$$\gamma_{primitive}^j = \sum_{r=1}^n w_r^j \gamma_{fundamental}^r \quad (17b)$$

where each of the coefficients m_p^j and w_r^j are integers.

Since the sets $\{\gamma^j\}$ and $\{\gamma_{primitive}^j\}$ are each collections of n independent nontrivial closed curves on the surface of the torus, the two collections of n vectors \mathbf{m}^j and \mathbf{w}^j are each linearly independent, and may each be arranged in an $n \times n$ invertible matrix \bar{m} and \bar{w} . It follows that:

$$\gamma^j = \sum_{p=1}^n \beta_p^j \gamma_{primitive}^p \quad (18)$$

where each of the coefficients β_p^j are rational numbers. It follows that the smooth classical action variables may be obtained from the primitive action variables by the relation:

$$J^k = \sum_{p=1}^n \beta_p^k J_{primitive}^k \quad (19)$$

In many familiar systems, the $\gamma_{primitive}^k$ form a fixed basis of curves for the fundamental homology class of the n-tori such that \bar{w} is the identity, and each of the coefficients β_p^j are integers. Thus where these primitive actions are not smooth they may be smoothly continued by determining the appropriate β 's.

Part IV

Semiclassical Theory of the Structure of the Hydrogen Spectrum in Near-Perpendicular Electric and Magnetic Fields: Derivations and Formulae for EBKM Quantization and Description of Monodromy

In this section we present the full details of the classical perturbation theory and show how semiclassical analysis can be used to predict all the features of the quantum spectrum which were discussed in part II. In particular we show how the quantum lattice defect structure is related to the existence of a multivalued classical action variable. We then return to the quantum description and show how the classical analysis suggests the definition of quantum operators which are used to construct the spectral lattices in a more rigorous manner than that which was presented in part II. Finally we show how quantum states are organized according to the classical phase space structure by inspecting a few quantum correlation diagrams in detail.

VI. OVERVIEW

A. The classical trajectories

Classical trajectories of the electron in a hydrogen atom in sufficiently strong magnetic fields are chaotic. However, if the fields are sufficiently weak, then the trajectories can be described as Kepler ellipses with slowly-varying orbital parameters. Most of the trajectories are then quasiperiodic, and form three-dimensional tori in the six-dimensional phase space. Classical perturbation theory replaces the exact Hamiltonian of the system with a “nearby” integrable Hamiltonian that has three constants of the motion, and therefore allows only regular trajectories. These three constants of the motion are approximately conserved on the exact trajectories.

When trajectories form continuous families of tori, then local action and angle variables can be constructed, and a semiclassical approximation to the quantum spectrum can be obtained by identifying those tori (sometimes called eigentori) on which the actions are appropriately quantized (usually as integers or half-integers). One of the actions is a variable called $Q(\mathbf{r}, \mathbf{p})$, whose numerical value we call q , which is quantized as an integer, and which corresponds to the cluster-number in the first-order spectrum.

Two related facts make the second-order spectrum of hydrogen in fields more complex. (1) Not all of the trajectories form tori. As will be explained later, some of them form pinched tori (see figures referenced in Section XD), and it is known that pinched tori are associated with Hamiltonian monodromy. (some more complex structures also occur.) (2) More important from the present perspective, the volume of the reduced phase space is related to $|q|$. Therefore it is not differentiable with respect to q at $q = 0$. It follows that one of the action variables (being an integral over a certain area in phase space) is not differentiable at $q = 0$. In our formulation, this is the source of monodromy in this system. Action variables by definition are supposed to be smooth functions of phase-space variables and of constants of the motion. If some primitive definition of

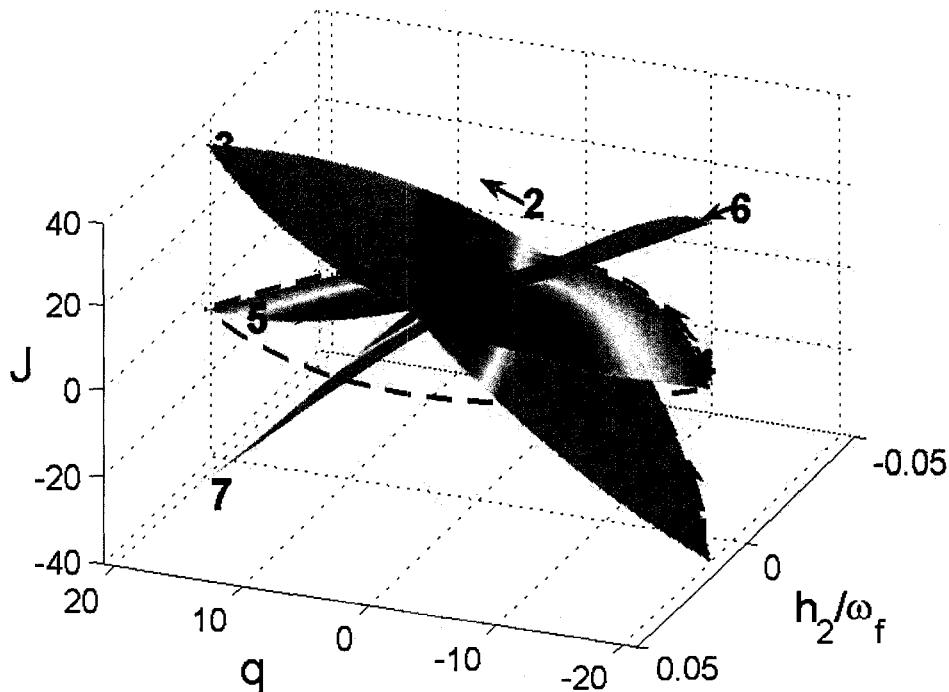


FIG. 16: (color online) For some field strength ratios, the Hamiltonian system obtained by perturbation theory has an intrinsically multivalued action variable $J(q, h_2)$ (here, $\mathbf{F} \cdot \mathbf{B} = 0$, $n = 20$ and $\tan^{-1}[3NF/B] = 50^\circ$). The set of all values of the constants of the motion q and h_2 which are classically allowed at fixed $n = 20$ are contained within the dashed boundary (red online). Almost all points inside this boundary are values of q and h_2 whose classical level sets are tori, but there is one isolated value of q and h_2 in the interior whose level set is a pinched torus. Since a full set of actions may only be defined on the tori, J is not defined at this value ($q = 0$ and $h_2 \sim 0.01\omega_f$) known as the monodromy center. Away from this point, J is locally smooth everywhere only if it is multivalued, with a branch point at the monodromy center. Three branches of the function are plotted in the figure. To continue the classical action variable smoothly, we may start at (1) and follow the arrows sequentially along the surface all the way to (7); then we pass onto a new branch every time we cross $q = 0$ if h_2 is greater than the energy of the monodromy center.

an action variable gives a discontinuous derivative, then that primitive action should be replaced by a smooth function. In systems having monodromy, smooth actions can be constructed, but they turn out to be multivalued functions of the constants of the motion (Fig. 16). The multivalued gradients of these smooth actions produce lattice defects in the semiclassical spectrum.

B. Comparison with other work

The spectrum of Hydrogen in fields is an old topic, going back to the earliest developments in quantum theory, and studied in many recent papers. It follows that any coherent discussion necessarily contains old results mixed with new ones. Let us briefly survey some recent work to discuss what is new in this paper.

The most important issues that have been treated inadequately (or not at all) in most of the earlier work are the topological aspects of the problem. Some had understood that Kepler averaging reduces the phase space from \mathbb{R}^6 to $S^2 \times S^2$. However, only recently was it realized that further reduction arising from averaging over the Pauli precession leads to a complex topological structure that contains ordinary tori, but may also contain doubly-pinched tori in perpendicular fields [11], [12], [13], or singly-pinched tori as well as other structures which are connected with monodromy in near-perpendicular fields [14], [23] (see figures in Section X).

Such phenomena occur at second order in perturbations of combined electric and magnetic fields. To our knowledge, Pauli never went beyond first order. Solov'ev, Uzer and collaborators, and others carried out calculations for crossed fields to second order, but did not make the connection with monodromy, which was not widely understood when they did their work.

There are also several other less important differences between the present work and previous work. (1) Where previous classical perturbation theory made use of the four dimensional Kustaanheimo-Stiefel regularization [26] and a normal form method [27], we carry out the perturbation in the three dimensional Delaunay variables. We obtain a second order Hamiltonian that is different from that obtained by the normal form method until we carry out the Pauli averaging, at which point our result agrees with previous work. To be specific, the resulting intermediate system, describing a small coupling between two independent angular momenta (Pauli's \mathbf{J} momenta), differs from

that derived by Gourlay, Uzer and Farrelly [6] by terms proportional to FB and F^2 (compare our Eq. 34 with Eq. 38 of Ref. [6]). However, after averaging over the motion of the Pauli vectors, the resulting system agrees with the previous results of Milczewski and Uzer [7]. We do not know if there is any significance to the discrepancy that exists prior to the Pauli averaging, but it is pleasing to know that the final averaged Hamiltonians obtained by the two different methods agree. Most recently the normal form method was used by Efstathiou, Sadovskii and Zhilinskiĭ [23] to interpret many of the near-perpendicular spectral structures that we found and displayed in Ref. [14] as well as structures that might be found near resonant angles away from perpendicular fields. We are not able to make an exact comparison between our formulas and theirs, but the structures appearing in figure 8 of [23] look like the ones we found in Ref. [14] and here.

(2) We present semiclassical calculations of spectra obtained by EBKM quantization of action variables, and we show that the result agrees with our *ab initio* quantum calculations, which are based on an expansion of the wavefunction in a multi-n-manifold Hydrogenic basis. Milczewski and Uzer [7] did a classical analysis (with less attention to topology and no attention to monodromy) but did not quantize to obtain a spectrum. Sadovskii and Cushman [11] obtained a reduced classical Hamiltonian, then converted it to a quantum operator by using a certain quantization postulate, and then constructed an approximate spectrum (such methods are sometimes called “semiquantal”). The connection between the quantum and classical second order energies presented by Solov’ev [8] is quite different, but may also be called “semiquantal” and is closely related to works by Herrick [9] and Braun [10]. In these analyses, the quantum Hamiltonian matrix is explicitly obtained and converted to a simple form which may be re-expressed as a recursion relationship. The semiclassical approximations for this recursion relationship yield a classical Hamiltonian. The second order Hamiltonian obtained by Solov’ev appears in Eqs. (7) and (8) of Ref. [8], and is almost the same as our Hamiltonian

(Eq. 30, Section VII). The difference is constant at fixed principal quantum number n , and can be regarded as a quantum correction to semiclassical theory.

(3) The quantum operators $\omega_f \hat{Q}$ and $\omega_f \hat{W}$ defined in Section XII B are generalizations of previously defined operators to multiple n -manifolds (constructed by replacing the quantum number n^2 with the operator $-\frac{1}{2} \hat{H}_0^{-1}$). In Section XIV A we also show that the quantum operator \hat{W} (Eq. 81) has expectation values which correspond to average values of a corresponding classical variable W . Where Solov'ev interpreted some of his results in terms of a "quasibarrier"; we have a concrete representation of a boundary between different types of states in the form of a classical separatrix in the reduced phase space.

(4) Finally there have been a number of papers on the relationship between the quantum spectrum and closed orbits of the electron [28]. The topological aspects (including monodromy) that are discussed here must have an impact on closed-orbit theory, but the implications have not yet been studied.

VII. DEGENERATE PERTURBATION OF THE KEPLER MOTION

Consider a non-relativistic, spinless hydrogen atom in static electric and magnetic fields \mathbf{F} and \mathbf{B} . Let the \mathbf{B} field vector define the z axis and let the \mathbf{F} and \mathbf{B} field vectors together define the $x - z$ plane. Then for weak, nearly-perpendicular fields [20] the Hamiltonian may be written in the following ordering (*Atomic units*):

$$H = H_0 + H_1 + H_2 = \underbrace{\frac{p^2}{2} - \frac{1}{r}}_{H_0} + \underbrace{\frac{B}{2} L_z + x F_x}_{H_1} + \underbrace{z F_z + \frac{B^2}{8} (x^2 + y^2)}_{H_2} \quad (20)$$

For vanishing field strengths, $H \rightarrow H_0$, every bound phase space orbit with finite energy is periodic. In the Delaunay action angle coordinates ([34], [35], [36], and table I), the coordinate along this periodic orbit is the principal angle ϕ_N , conjugate to the principal action N . We use Poincaré-Von Zeipel degenerate canonical perturbation

TABLE I: Delaunay Action and Angle Variables

Canonical Angle	Classical Name
ϕ_N	Mean Anomaly
ϕ_p	Argument of the Perihelion
Ω	Longitude of the Ascending Node
Conjugate Momentum	Classical Name
N	Principal Action
L	Magnitude of the Total Angular Momentum \mathbf{L}
L_z	Space Fixed z Component of \mathbf{L}

theory ([34], [35]) to construct an approximate Hamiltonian which is independent of the new principal angle $\bar{\phi}_N$ through terms of second order in field strengths.

A. Canonical perturbation theory

We first transform the Hamiltonian Eq. 20 from the Cartesian coordinates to the Delaunay action angle variables. We then enact a time independent canonical transformation via a generating function f with the following properties: (i) f is expanded in orders of the field strengths about the identity transformation (ii) f is periodic in both the old and new angles. The canonical transformation relates old and new variables:

$$(N, L, L_z, \phi_N, \phi_p, \Omega)_{old} \leftrightarrow (\bar{N}, \bar{L}, \bar{L}_z, \bar{\phi}_N, \bar{\phi}_p, \bar{\Omega})_{new} \quad (21)$$

through the generating function

$$f(q, \bar{P}) = q\bar{P} + f_1(q, \bar{P}) + f_2(q, \bar{P}) + \dots \quad (22)$$

We refer to the new variables as perturbed Delaunay Coordinates. Equating the old and the new Hamiltonian in the space of mixed coordinates $(\bar{N}, \bar{L}, \bar{L}_z, \phi_N, \phi_p, \Omega)$ we have to second order:

$$\bar{H}_0 = H_0 \quad (23a)$$

$$\bar{H}_1 = H_1 + \frac{\partial H_0}{\partial N} \frac{\partial f_1}{\partial \phi_N} \quad (23b)$$

$$\bar{H}_2 = H_2 + H'_2 \quad (23c)$$

$$H'_2 = \frac{\partial H_1}{\partial N} \frac{\partial f_1}{\partial \phi_N} + \frac{\partial H_1}{\partial L} \frac{\partial f_1}{\partial \phi_p} + \frac{\partial H_1}{\partial L_z} \frac{\partial f_1}{\partial \Omega} + \frac{1}{2} \frac{\partial^2 H_0}{\partial N^2} \left(\frac{\partial f_1}{\partial \phi_N} \right)^2 + \frac{\partial H_0}{\partial N} \frac{\partial f_2}{\partial \phi_N} \quad (23d)$$

By the imposed ϕ_N periodicity on the functions f_1, f_2 one obtains:

$$\bar{H}_0 = H_0 \quad (24a)$$

$$\bar{H}_1 = \langle H_1 \rangle_{\phi_N} \quad (24b)$$

$$\bar{H}_2 = \langle H_2 \rangle_{\phi_N} + \langle H'_2 \rangle_{\phi_N} \quad (24c)$$

where

$$\langle g \rangle_{\phi_N} = \frac{1}{2\pi} \oint g \, d\phi_N \quad (24d)$$

The perturbed Delaunay coordinates are related to a new Cartesian space through the same transformation that connected the original Delaunay variables and the original Cartesian space. In this new Cartesian space we can consider the Kepler orbits and their associated angular momentum and energy-scaled-Laplace-Runge-Lenz Eccentricity vectors $\bar{\mathbf{L}}$ and $\bar{\mathbf{M}}$. When a small perturbation is applied to the Kepler system, one may describe the perturbed trajectory as a Kepler ellipse of fixed \bar{N} , with slowly varying orbital elements $\bar{\mathbf{L}}$ and $\bar{\mathbf{M}}$. For the remainder of this section we will work exclusively in the new coordinates, and for notational convenience, we now drop the *bars* from the new Delaunay variables.

The eccentricity vector \mathbf{M} extends from the nucleus, in the direction of the instantaneous perigee of the ellipse, with magnitude $M = Ne$, where e is the eccentricity of the ellipse with $0 \leq e \leq 1$.

$$\mathbf{M} = N(\mathbf{p} \times \mathbf{L} - \hat{\mathbf{r}}) \quad (25)$$

The angular momentum vector \mathbf{L} extends from the nucleus, normal to the orbital plane.

$$\mathbf{L} = \mathbf{r} \times \mathbf{p} \quad (26)$$

The two vectors are constrained in direction and magnitude by two conditions,

$$\mathbf{L} \cdot \mathbf{M} = 0 \quad (27a)$$

$$\mathbf{L}^2 + \mathbf{M}^2 = N^2 \quad (27b)$$

and share a closed Poisson algebra ([37], [35]).

$$\{\mathbf{L}, \mathbf{L}\} = \epsilon \mathbf{L} \quad (28a)$$

$$\{\mathbf{M}, \mathbf{M}\} = \epsilon \mathbf{L} \quad (28b)$$

$$\{\mathbf{M}, \mathbf{L}\} = \epsilon \mathbf{M} \quad (28c)$$

$$\{\mathbf{L}, H_0\} = \{\mathbf{M}, H_0\} = 0 \quad (28d)$$

Eqs. 23 and 24 are expressed in Delaunay Variables. However, the new Hamiltonian is independent of ϕ_N by construction, and therefore can only depend on the fixed value of N , and on the instantaneous eccentricity and orientation of the ellipse in space. Therefore, it can be expressed as a function of the components of \mathbf{L} and \mathbf{M} . We evaluate the averages in Eq. 24 in an orbital frame defined by the basis vectors

$$\{\hat{z}, \hat{x}, \hat{y}\} = \left\{ \frac{\mathbf{L}}{L}, \frac{\mathbf{M}}{M}, \frac{\mathbf{L} \times \mathbf{M}}{LM} \right\} \quad (29)$$

and it is shown in Appendix A that the resulting Hamiltonian is:

$$\begin{aligned}
\bar{H}(\mathbf{L}, \mathbf{M}; N) &= \bar{H}_0 + \bar{H}_1 + \bar{H}_2 \\
&= -\frac{1}{2N^2} + \underbrace{\frac{1}{2}B_z L_z - \frac{3}{2}NF_x M_x}_{\langle H_1 \rangle_{\phi_N}} \\
&\quad + \underbrace{\frac{B^2 N^2}{16} [N^2 + 4M^2 - 5M_z^2 + L_z^2] - \frac{3}{2}NF_z M_z}_{\langle H_2 \rangle_{\phi_N}} \\
&\quad - \underbrace{\frac{F_x^2 N^4}{16} [29N^2 - 24M^2 - 21L_x^2 + 9M_x^2]}_{\langle H'_2 \rangle_{\phi_N}}
\end{aligned} \tag{30}$$

This result differs from Eqs. (7) and (8) of Ref. [8] by $19N^4 F^2/16$.

The Hamiltonian in Eq. 30 governs the motion of \mathbf{L} and \mathbf{M} at fixed N , preserving the constraints in Eqs. 27. That motion is conveniently described using Pauli's \mathbf{J} vectors.

$$\mathbf{J}_1 = \frac{1}{2}(\mathbf{L} + \mathbf{M}) \tag{31a}$$

$$\mathbf{J}_2 = \frac{1}{2}(\mathbf{L} - \mathbf{M}) \tag{31b}$$

By the properties (Eqs. 27) of \mathbf{L} and \mathbf{M} and their Poisson Brackets (Eqs. 28) one may calculate:

$$\{\mathbf{J}_i, \mathbf{J}_i\} = \epsilon \mathbf{J}_i \tag{32a}$$

$$\{\mathbf{J}_i, \mathbf{J}_{j \neq i}\} = 0 \tag{32b}$$

and

$$|\mathbf{J}_1| = |\mathbf{J}_2| = \frac{N}{2} \tag{33}$$

The two Pauli vectors have identical fixed magnitudes and may be oriented arbitrarily in space. Every Kepler orbit of a given N -manifold is thus identified with a single point on $S^2 \times S^2$; *i.e.* the reduced phase space is the product of two spheres.

Expressing \mathbf{L} and \mathbf{M} in terms of the \mathbf{J} vectors by inverting Eqs. 31 and substituting in Eq. 30 yields:

$$\begin{aligned} \bar{H}(\mathbf{J}_1, \mathbf{J}_2; N) = & -\frac{1}{2N^2} + \frac{B}{2} (J_{1,z} + J_{2,z}) - \frac{3}{2}NF_x (J_{1,x} - J_{2,x}) - \frac{3}{2}NF_z (J_{1,z} - J_{2,z}) \\ & + \frac{B^2N^2}{16} [3N^2 + 4J_{1,z}J_{2,z} - 8(J_{1,x}J_{2,x} + J_{1,y}J_{2,y}) - 4(J_{1,z}^2 + J_{2,z}^2)] \\ & - \frac{F_x^2N^4}{16} [17N^2 + 48(J_{1,y}J_{2,y} + J_{1,z}J_{2,z}) - 12(J_{1,x}^2 + J_{2,x}^2 + J_{1,x}J_{2,x})] \end{aligned} \quad (34)$$

This result differs from Eq. 38 of Ref. [6] by terms proportional to $F_x B$ and F_x^2 .

VIII. FIRST ORDER DYNAMICS: THE PAULI PRECESSION

The Hamiltonian (Eq. 34) governs a reduced two dimensional system describing the slow evolution of the classical orbital elements. Since N is conserved, \bar{H}_0 can be regarded as an additive constant. To first order, the fields are perpendicular, and the first order Hamiltonian is:

$$\bar{H}_1 = \frac{1}{2}B_z L_z - \frac{3}{2}NF_x M_x \quad (35)$$

All orbits of \bar{H}_1 are strictly periodic as will be shown in the following sections.

A. The Pauli Precession

For arbitrary orientation of electric and magnetic fields, a calculation of the first order effects on the hydrogen spectrum is due to Pauli [2]. He defined two ‘effective field vectors’:

$$\boldsymbol{\Omega}_1 = \frac{1}{2}\mathbf{B} - \frac{3}{2}N\mathbf{F} \quad (36a)$$

$$\boldsymbol{\Omega}_2 = \frac{1}{2}\mathbf{B} + \frac{3}{2}N\mathbf{F} \quad (36b)$$

One may define scaled versions of the $\boldsymbol{\Omega}$ vectors such that for exactly perpendicular fields ($\mathbf{F} \cdot \mathbf{B} = 0$) the scaled versions have unit magnitude:

$$\boldsymbol{\omega}_j = \frac{\boldsymbol{\Omega}_j}{\omega_f} \quad (37a)$$

with:

$$\omega_f = \frac{1}{2} \sqrt{B^2 + (3NF)^2} \quad (37b)$$

Using Eqs. 31 and Eqs. 37, Pauli wrote the first order crossed fields Hamiltonian in the form:

$$H_{Pauli} = \omega_f (\boldsymbol{\omega}_1 \cdot \mathbf{J}_1 + \boldsymbol{\omega}_2 \cdot \mathbf{J}_2) \quad (38a)$$

The form of the Hamiltonian (Eq. 38a) and the Poisson algebra of the \mathbf{J}' s (Eqs. 32) imply that the equations of motion describe the precession of \mathbf{J}_1 about $\boldsymbol{\omega}_1$ such that its component μ_1 along the $\boldsymbol{\omega}_1$ axis is conserved, and an analogous precession of \mathbf{J}_2 about $\boldsymbol{\omega}_2$ conserving μ_2 . Then the Hamiltonian (Eq. 38a) can be rewritten in terms of the components μ_i of the \mathbf{J}_i vectors in the $\boldsymbol{\omega}_i$ directions:

$$H_{Pauli} = \omega_f (\omega_1 \mu_1 + \omega_2 \mu_2) \quad (38b)$$

For exactly perpendicular fields ω_1 and ω_2 are unity (Eq. 37). This implies that the first order Hamiltonian (Eq. 35) can be expressed as:

$$\bar{H}_1 = \omega_f (\mu_1 + \mu_2) \quad (38c)$$

Thus, for perpendicular fields, both vectors precess at the same rate ω_f about their respective axes, and the motion is strictly periodic.

B. Local canonical coordinates on $S^2 \times S^2$

We now construct a canonical coordinate system to describe the Pauli Precession motion. For all μ_1 such that $-N/2 < \mu_1 < N/2$ there is an angle ψ_1 with $0 < \psi_1 \leq 2\pi$

which describes the position of \mathbf{J}_1 on the cone of precession. This angle may be defined in terms of the vector components of \mathbf{J}_1 in a Cartesian coordinate system having the z' axis parallel to $\boldsymbol{\Omega}_1$ and the y' axis parallel to the y axis in the space fixed frame such that $J_{1,z'} = \mu_1$.

$$\psi_1 = \tan^{-1} \left(\frac{J_{1,y'}}{J_{1,x'}} \right) \quad (39)$$

Similarly for all μ_2 such that $-N/2 < \mu_2 < N/2$ there is an angle ψ_2 , describing the precession of \mathbf{J}_2 , which is defined analogously to ψ_1 . Thus, at each (μ_1, μ_2) with neither $|\mu_1|$ nor $|\mu_2|$ equal to $N/2$, the available phase space consists of a 2-torus.

It is clear from Eq. 39 that there are some values of the $\mu_i = J_{i,z'}$ for which this coordinate system breaks down. When $|\mu_i| = N/2$, $J_{i,x'} = J_{i,y'} = 0$ and so ψ_i is undefined. However, as long as $|\mu_{j \neq i}| \neq N/2$, ψ_j is still defined, and phase space is a circle. When both $|\mu_1|$ and $|\mu_2|$ are equal to $N/2$, phase space is a point.

By the properties of the \mathbf{J}_1 and \mathbf{J}_2 Poisson algebra (Eqs. 32) and the definitions implied by Eq. 39, the two angles ψ_i and the corresponding effective field vector components μ_i form a system of local canonical coordinates $(\mu_1, \mu_2, \psi_1, \psi_2)$ on the $S^2 \times S^2$ space of all Kepler orbits at fixed N . Their Poisson bracket relations follow from Eqs. 39 and Eqs. 32:

$$\{\mu_i, \psi_j\} = \delta_{i,j} \quad (40a)$$

$$\{\psi_i, \psi_j\} = 0 \quad (40b)$$

$$\{\mu_i, \mu_j\} = 0 \quad (40c)$$

The local symplectic 2-form associated with Eqs. 40 is [38]:

$$\omega^2 = d\mu_1 \wedge d\psi_1 + d\mu_2 \wedge d\psi_2 \quad (41)$$

C. Degenerate coordinates on the Pauli 2-Torus

The first order canonical equations of motion are obtained from Eq. 38c.

$$\mu_j(t) = \mu_j(0) \quad (42a)$$

$$\psi_j(t) = \omega_f t + \psi_j(0) \quad (42b)$$

for $j = 1, 2$. At fixed values of the momenta (μ_1, μ_2) where both angles are defined, the phase space is a 2-torus covered by the coordinates ψ_1 and ψ_2 . When the torus is depicted as a square of length 2π , the motion is along a straight line with a unit slope, reflecting the one-to-one resonance between the angles on the Pauli Torus at perpendicular fields.

We make a canonical transformation into coordinates such that one of the new angles δ_Q is aligned along this periodic motion. The transformation; $(\mu_1, \mu_2, \psi_1, \psi_2) \rightarrow (Q, W, \delta_Q, \delta_W)$ may be enacted with the generating function:

$$G(\psi_1, \psi_2, Q, W) = \frac{Q}{2}(\psi_1 + \psi_2) + \frac{W}{2}(\psi_1 - \psi_2) \quad (43)$$

from which one obtains the new coordinates:

$$Q = \mu_1 + \mu_2 \quad (44a)$$

$$W = \mu_1 - \mu_2 \quad (44b)$$

$$\delta_Q = \frac{1}{2}(\psi_1 + \psi_2) \quad (44c)$$

$$\delta_W = \frac{1}{2}(\psi_1 - \psi_2) \quad (44d)$$

and the new Hamiltonian function:

$$\bar{H}_1 = \omega_f Q \quad (45)$$

Now a 2-torus formerly labeled by the constant values (μ_1, μ_2) is labeled by the constant values (Q, W) . From Eqs. 41 and 43 it follows that in the new coordinates the local canonical 2-form is:

$$\omega^2 = dQ \wedge d\delta_Q + dW \wedge d\delta_W \quad (46)$$

Since $|\mathbf{J}_i| = N/2$, the allowed values of the components μ_1 and μ_2 form a closed square with length $[-N/2, N/2]$. It follows that the allowed ranges of Q and W become $-N \leq Q \leq N$ and $-(N - |Q|) \leq W \leq (N - |Q|)$ as is illustrated in Fig. 17(a). The allowed ranges of δ_Q and δ_W can be chosen in a number of ways. For values of $Q(\mu_1, \mu_2)$ and $W(\mu_1, \mu_2)$ such that both ψ_1 and ψ_2 are defined, they are coordinates on a two torus $mod(2\pi)$, and it is convenient initially to say that each ranges between $-\pi$ and π . Then, δ_Q would also range from $-\pi$ to π , while δ_W would range from $-(\pi - |\delta_Q|)$ to $(\pi - |\delta_Q|)$. This however, is inconvenient. It is better to tile the (ψ_1, ψ_2) plane as indicated in Fig. 17(b) such that δ_Q and δ_W have the independent ranges $-\pi \leq \delta_Q \leq \pi$ and $-\pi/2 \leq \delta_W \leq \pi/2$.

It follows from our discussion of the breakdown of the (μ, ψ) coordinates that not all values of (Q, W) label a 2-torus. If μ_1 and μ_2 were such that one or both ψ 's were undefined, the functions δ_Q and δ_W become meaningless. Thus we cannot use these coordinate functions at any point such that $|W| = N - |Q|$.

IX. DEGENERATE PERTURBATION OF THE PAULI MOTION

In the previous section it was shown that to first order in field strengths and angle, the principal effect of the perturbation is a periodic evolution δ_Q at fixed N, Q, W and δ_W . To describe the effects of second order terms in the Hamiltonian, we use classical canonical degenerate perturbation theory a second time, effectively reducing the system to a single degree of freedom.

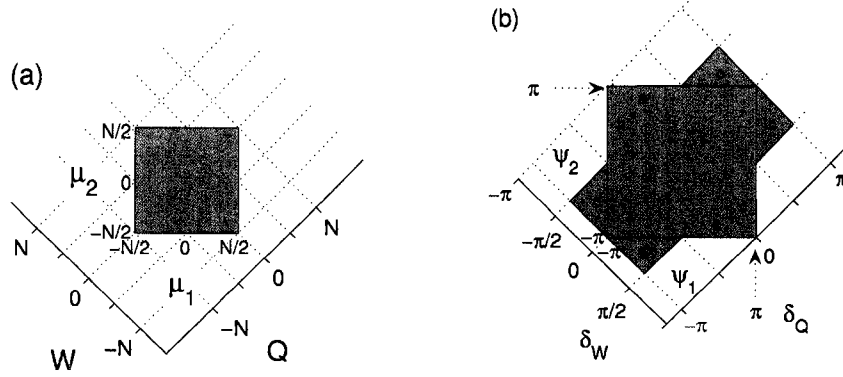


FIG. 17: Transformation of the coordinate ranges. (a) The set of all possible components μ_i of \mathbf{J}_i along ω_i , for $|J_i| = N/2$ and $i = 1, 2$ define a closed square. The introduction of the coordinates $Q = \mu_1 + \mu_2$, $W = \mu_1 - \mu_2$ implies the ranges $-N \leq Q \leq N$ and $-(N - |Q|) \leq W \leq N - |Q|$. (b) ψ_1 and ψ_2 are angular coordinates on a 2-torus, defined $\text{mod}(2\pi)$. The ranges of $\delta_Q = (\psi_1 + \psi_2)/2$ and $\delta_W = (\psi_1 - \psi_2)/2$ are inconvenient when restricted to the square indicated in the figure. Since the square is simply a particular choice of tiling the 2-torus, we are free to retiling the plane such that the new angles have rectangular restrictions. The pairs of triangular regions marked with identical letters contain points in the plane which represent identical points on the torus. We see that the torus can be described by the angles $-\pi < \delta_Q \leq \pi$ and $-\pi/2 < \delta_W \leq \pi/2$.

The Hamiltonian \bar{H} in Eq. 34 is a function of the space fixed components of the Pauli Vectors J_{i,x_j} (Eqs. 31) in the space fixed basis $(\hat{x}, \hat{y}, \hat{z})$. In a reference frame specified by the basis vectors $(\hat{x}'_i \equiv \hat{y} \times \hat{\omega}_i, \hat{y}'_i \equiv \hat{y}, \hat{z}'_i \equiv \hat{\omega}_i)$ the components of the Pauli Vectors J_{i,x'_j} are expressed as functions of μ_i and ψ_i :

$$(J_{i,x'}, J_{i,y'}, J_{i,z'}) = \left(\sqrt{\frac{N^2}{4} - \mu_i^2} \cos \psi_i, \sqrt{\frac{N^2}{4} - \mu_i^2} \sin \psi_i, \mu_i \right) \quad (47)$$

These vector components are then written as functions of the coordinates $\{Q, W, \delta_Q, \delta_W\}$ using the transformations in Eq. 44. The space fixed components of \mathbf{J}_i are related to its ω_i frame components by the orthonormal transformation matrix M_i .

$$J_{i,\alpha} = M_{i,\alpha\beta'} J_{i,\beta'} \quad (48a)$$

where $\alpha = x, y, z$, $\beta' = x', y', z'$, $i = 1, 2$ and

$$M_{i,jk} = \hat{x}_j \cdot \hat{x}'_k \quad (48b)$$

Substitute the resulting expressions $J_{i,x_j}(Q, W, \delta_Q, \delta_W)$ for the space fixed components into Eq. 34 to obtain:

$$\bar{H} = -\frac{1}{2N^2} + \omega_f Q + \bar{H}_2(Q, W, \delta_Q, \delta_W) \quad (49)$$

We then enact the canonical transformation:

$$(Q, W, \delta_Q, \delta_W) \longrightarrow (\tilde{Q}, \tilde{W}, \tilde{\delta}_Q, \tilde{\delta}_W) \quad (50)$$

using a near-identity generating function

$$g(q, \tilde{P}) = q\tilde{P} + g_1(q, \tilde{P}) \quad (51)$$

Since g_1 must be periodic in δ_Q , one obtains expressions for the new Hamiltonian h

$$h_0 + h_1 = \bar{H}_0 + \bar{H}_1 \quad (52a)$$

$$h_2 = \langle \bar{H}_2 \rangle_{\delta_Q} \quad (52b)$$

where

$$\langle f \rangle_{\delta_Q} = \frac{1}{2\pi} \oint f d\delta_Q \quad (52c)$$

The result is a new Hamiltonian $h = h_0 + h_1 + h_2$ which is independent of $\tilde{\delta}_Q$.

A. The fully reduced Hamiltonian

It is straightforward to compute $\langle \bar{H}_2 \rangle_{\delta_Q}$, and one obtains (dropping all decorations in the final coordinate system)

$$h_2 = h_c + \beta W^2 + \zeta W + \alpha \sqrt{(N^2 - (Q - W)^2)(N^2 - (Q + W)^2)} \cos(2\delta_W) \quad (53a)$$

where each of the coefficients α , β , and ζ are second order in field strengths

$$\alpha \equiv -\frac{N^2}{16} 2B^2 \quad (53b)$$

$$\beta \equiv -\frac{N^2}{16} \left[B^2 - (3NF_x)^2 + \frac{2B^4}{B^2 + (3NF_x)^2} \right] \quad (53c)$$

$$\zeta \equiv -\frac{3NF_z B}{2\sqrt{B^2 + (3NF_x)^2}} \quad (53d)$$

h_c is independent of the coordinates (W, δ_W) , and may be regarded as another additive constant,

$$h_c = \frac{N^2}{16} \left[\frac{B^2}{3} \left(7 + \frac{2B^2}{B^2 + (3NF_x)^2} \right) - 17N^2 F_x^2 \right] N^2 + \frac{N^2}{16} \left[\frac{(3NF_x)^2}{3} + B^2 \left(1 - \frac{2B^2}{B^2 + (3NF_x)^2} \right) \right] Q^2 \quad (53e)$$

h_2 is independent of δ_Q rendering Q a constant of the motion, and we have obtained a system with one degree of freedom governed by the effective hamiltonian $h_2(W, \delta_W)$.

B. Expression in scaled parameters

The Hamiltonian in Eqs. 53 can be expressed in terms of ω_f defined in Eq. 37b such that $|h_2| \approx \omega_f^2$. The following definition of θ allows a convenient parameterization of all possible field magnitude ratios at a given perturbation strength ω_f :

$$\theta = \tan^{-1} \left(\frac{3N|F|}{|B|} \right) \quad 0 \leq \theta \leq \frac{\pi}{2} \quad (54)$$

This implies the following two field definitions:

$$3NF = 2\omega_f \sin\theta \quad (55a)$$

$$B = 2\omega_f \cos\theta \quad (55b)$$

with the Zeeman and Stark limits at $\theta = 0$ and $\theta = \pi/2$ respectively. The angle between the electric field and the x axis is χ , and implies that $F \sin\chi = F_z$. Then Eq. 53b is

rewritten using Eq. 55b:

$$\alpha = -\frac{N^2\omega_f^2}{4}2\cos^2\theta \quad (56a)$$

β , ζ and h_c in Eqs. 53c, 53d and 53e depend on the quantity $(3NF_x)^2$. For near perpendicular fields such that $|\chi| \lesssim \omega_f n^3 \ll 1$, we may replace F_z with χF , and $(3NF_x)^2$ with $(3NF)^2$ with negligible error at second order. Using these replacements, along with Eqs. 55, we rewrite Eqs. 53c, 53d and 53e as:

$$\beta = \frac{N^2\omega_f^2}{4} [1 - 2(\cos^2\theta + \cos^4\theta)] \quad (56b)$$

$$\zeta = -\frac{N^2\omega_f^2}{4} \left[4\cos\theta\sin\theta \frac{\chi}{\omega_f N^2} \right] \quad (56c)$$

$$h_c = \frac{N^2\omega_f^2}{4} \left[-\frac{17}{9} + \frac{38}{9}\cos^2\theta + \frac{2}{3}\cos^4\theta \right] N^2 + \frac{N^2\omega_f^2}{4} \left[\frac{1}{3} + \frac{2}{3}\cos^2\theta - 2\cos^4\theta \right] Q^2 \quad (56d)$$

X. REDUCED DESCRIPTIONS

In this section we display the topological structure of the reduced phase spaces.

A. The structure of the four dimensional reduced phase space Γ_N

The space of all Kepler orbits at a fixed N is denoted $\Gamma_N \sim S^2 \times S^2$, and each of the points $(\mathbf{J}_1, \mathbf{J}_2)$ in this four dimensional reduced phase space represents a Kepler orbit. The local canonical coordinates in Γ_N are $(Q, W, \delta_Q, \delta_W)$. We organize the structure of Γ_N by considering the subset of phase space which is located at each value of Q and W (Fig. 18). At each (Q, W) with $|Q| < N$ and $|W| < (N - |Q|)$, there is a 2-torus with coordinates δ_Q and δ_W . At points $0 < |Q| < N$, $W = \pm(N - |Q|)$ there is a circle [39]. At each of the four corners $(Q = \pm N, W = 0)$ and $(Q = 0, W = \pm N)$, there is only a point. At every value of Q and W , we call the phase space orbit generated by the

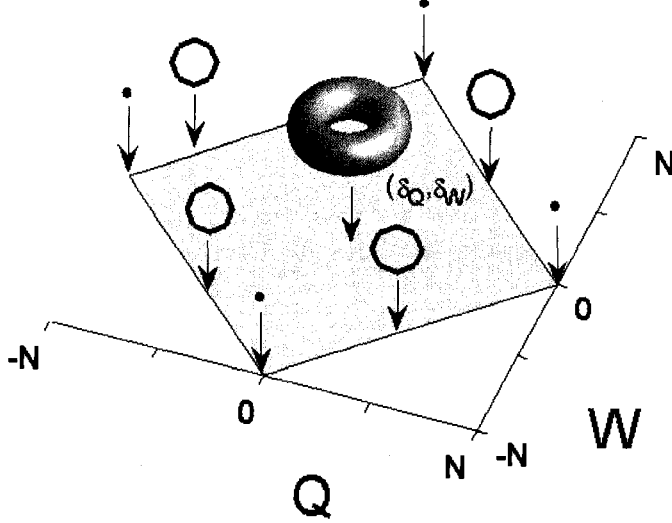


FIG. 18: The structure of Γ_N , the four dimensional reduced phase space at fixed N . Each base point (Q, W) with $|Q| < N$ and $|W| < (N - |Q|)$ labels a 2-torus with coordinates δ_Q and δ_W . The points $0 < |Q| < N$, $W = \pm(N - |Q|)$ correspond to a circle. At each of the four corners ($Q = \pm N, W = 0$) and ($Q = 0, W = \pm N$), the phase space consists of a single point. At each fixed Q, W and fixed δ_W if $|W| < N - |Q|$, there is a periodic orbit, which we call the Pauli Orbit, generated by the Hamiltonian $H = \omega_f Q = \omega_f(\mu_1 + \mu_2)$. Each Pauli orbit is a circle except at the four corners, where it is a point.

Hamiltonian (Eq. 38c) the Pauli orbit at fixed Q, W and also fixed δ_W if $|W| < N - |Q|$. A Pauli orbit is a one dimensional closed curve everywhere except at the four corners where it is a point.

The second order field terms act as a small perturbation to the Pauli system described in section VIII. One may describe the resulting motion as a Pauli orbit of fixed Q , with slowly varying orbital elements W and δ_W .

Three distinct structures of phase space result from fixing particular values of Q on the closed interval $[-N, N]$ (See Fig. 18). (i) The trivial case is obtained by fixing $Q = \pm N$, where phase space is a point. (ii) Fixing any Q such that $0 < |Q| < N$ results in a structure which is depicted in Fig. 19a. W ranges between $\pm(N - |Q|)$, and for all $|W| < N - |Q|$ there is a 2-torus with coordinates δ_Q and δ_W , which collapses to a circle

at either $W = \pm(N - |Q|)$. A circle at every W is identified with a Pauli orbit. For $|W| < N - |Q|$, the Pauli Hamiltonian $H = \omega_f Q = \omega_f(\mu_1 + \mu_2)$ generates the circle with coordinate δ_Q , and at $W = \pm(N - |Q|)$, the Pauli orbit is along the appropriate ψ_i . For convenience we define σ_Q to be equal to δ_Q for $|W| < N - |Q|$, and to be equal to the appropriate ψ_i for $W = \pm(N - |Q|)$. (iii) The case of $Q = 0$ is illustrated in Fig. 19b. W ranges between $\pm N$, and for all $|W| < N$ there is a 2-torus with coordinates δ_Q and δ_W , which collapses to a point at either $W = \pm N$. For $|W| < N$, the Pauli orbit is the circle with coordinate δ_Q , and at $W = \pm N$, the Pauli orbit consists of a single point in Γ_N .

For the nontrivial cases (ii) and (iii), when we consider each Pauli orbit at fixed N and fixed Q to be a point in a fully reduced phase space, then that space is a two dimensional surface denoted $\Gamma_{N,Q}$, which is connected like a sphere (Appendix B) and is equipped with the local canonical coordinates (W, δ_W) .

Here we must caution the reader about a subtle point. In the four dimensional phase space $S^2 \times S^2$, the two dimensional surface defined by constant Q and constant σ_Q , and spanned by (W, δ_W) is not homeomorphic to a sphere. It is only after we regard all points $\sigma_Q (0 \leq \sigma_Q < 2\pi)$ as being equivalent that the (W, δ_W) surface called $\Gamma_{N,Q}$ is homeomorphic to a sphere.

B. The two dimensional fully reduced phase space $\Gamma_{N,Q}$

The total energy of the system is the value of the Hamiltonian h

$$h = -\frac{1}{2N^2} + \omega_f Q + h_2(W, \delta_W; N, Q) \quad (57)$$

where h_2 is defined in either Eqs. 53 or Eqs. 56. Since h_2 conserves N and Q , and is independent of δ_Q , the dynamics are described by the motion of the system point on the (W, δ_W) surface $\Gamma_{N,Q}$. The system point will evolve on this surface according to

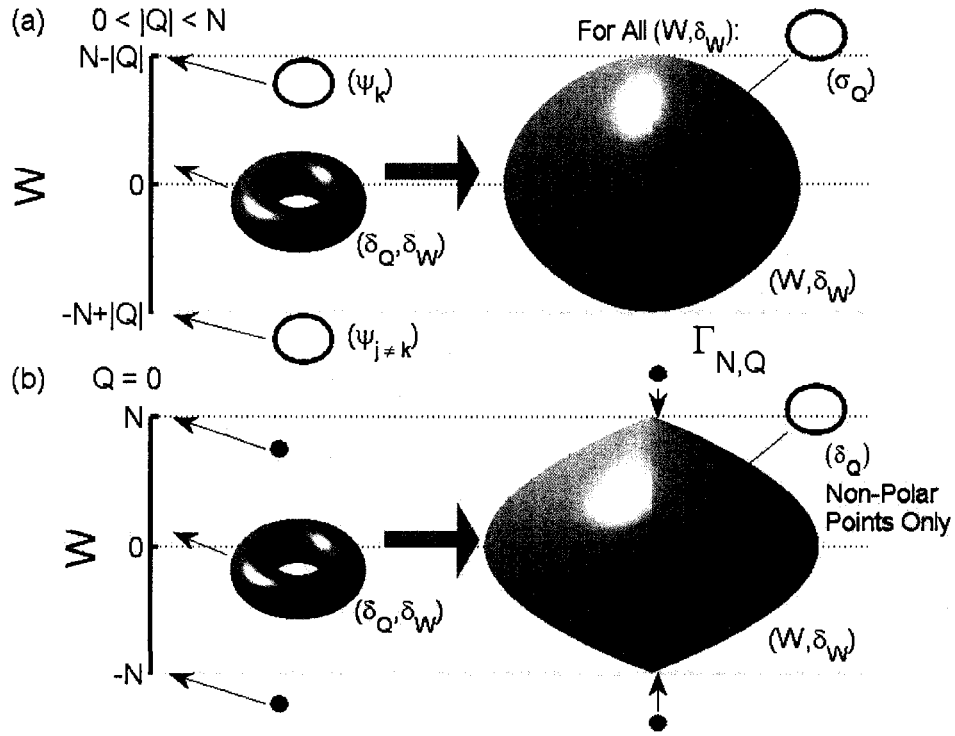


FIG. 19: The structure of the reduced phase space at fixed N and fixed Q , and the space of all Pauli orbits $\Gamma_{N,Q}$. The values of W range between $\pm(N - |Q|)$. For all W such that $|W| < N - |Q|$, there exists a 2-torus with coordinates δ_Q and δ_W . On each torus, the δ_Q circle is identified with the Pauli orbit, generated by the Hamiltonian $H = \omega_f(\mu_1 + \mu_2)$. (a) For a fixed Q with $0 < |Q| < N$, there exists a circle at the endpoints $W = \pm(N - |Q|)$, identified with the Pauli orbit, and having the appropriate ψ_i coordinate. (b) For $Q = 0$ there is only a single point at $W = \pm N$, each identified with a stationary Pauli orbit. (a and b right) For all fixed N and $Q \neq \pm N$, the space of all Pauli orbits $\Gamma_{N,Q}$ is a two dimensional surface that is connected like a sphere and has the coordinates W and δ_W . At every point on this surface there exists a Pauli orbit which is, (a) everywhere a circle for $0 < |Q| < N$, but (b) for $Q = 0$ is a circle at all non-polar points, but is a point at the poles.

Hamilton's equations of motion:

$$\frac{dW}{dt} = -\frac{\partial h_2}{\partial \delta_W} \quad (58a)$$

$$\frac{d\delta_W}{dt} = \frac{\partial h_2}{\partial W} \quad (58b)$$

Therefore, all information about the total energy (Eq. 57), and the dynamics of the second order system (Eqs. 58), are ascertained by inspection of the contours of h_2 on the (W, δ_W) surface at fixed N and Q .

On $\Gamma_{N,Q}$ the canonical two-form in Eq. 46 is:

$$\omega^2 = dW \wedge d\delta_W \quad (59)$$

Eq. 59 is not defined at the poles ($W = \pm(N - |Q|)$), but we will only be interested in surface integrals of (Eq. 59), and not the 2-form itself.

To describe the dynamics of the reduced system, it is useful to depict the (W, δ_W) surface as a two dimensional surface in a three dimensional space in several different ways (Fig. 20).

(1) The (W, δ_W) surface may be depicted as a cylinder of radius $\rho = \frac{1}{2}$ and height $L = 2(N - |Q|)$. Then the canonical 2-form (Eq. 59) is equal to the differential of Euclidean area on the cylinder's surface, $\omega^2 = dA_{cyl}$. However, the boundaries of this cylinder must be understood to each represent a single point on the (W, δ_W) surface (the north and south poles). Cutting this cylinder along $\delta_W = \pm\pi/2$ and unrolling the surface yields flat contour maps of h_2 which appear in this paper and in Ref. [14]. In these flat representations, (i) the area is the canonical area, (ii) left and right edges where $\delta_W = \pm\pi/2$ are identified, and (iii) the upper and lower boundaries where $W = \pm(N - |Q|)$ are understood to each consist of a single point. The cylinder representation is useful for calculating actions, and for depicting the phase space on a page, but it can obscure the behavior near the poles $W = \pm(N - |Q|)$.

(2) As an alternative, the (W, δ_W) surface may be depicted as a sphere [40] of radius $r = N - |Q|$ in a fictitious Cartesian space (ξ_1, ξ_2, ξ_3) , with $W = \xi_3$ and $\delta_W = \frac{1}{2}\tan^{-1}(\xi_2/\xi_1)$. The space of Pauli orbits at any fixed Q with $|Q| < N$ is homeomorphic to this sphere, and the canonical 2-form is related to the differential of Euclidean surface area by: $\omega^2 = \frac{1}{2}dA_{sph}/(N - |Q|)$.

(3) Finally, Sadovskii and Cushman [11], [12], [13] have proposed that the differential structure (smoothness) of the reduced phase space is represented by embedding that

space in the coordinates (π_1, π_2, π_3) , where:

$$\pi_1 = W \tag{60a}$$

$$\pi_2 = 4 \left(J_{1,x'_1} J_{2,x'_2} + J_{1,y'_1} J_{2,y'_2} \right) \tag{60b}$$

$$\pi_3 = 4 \left(J_{1,y'_1} J_{2,x'_2} - J_{1,x'_1} J_{2,y'_2} \right) \tag{60c}$$

In this space the (W, δ_W) surface takes the form of a surface of revolution defined by $(\pi_2, \pi_3) = (\rho \cos(2\delta_W), \rho \sin(2\delta_W))$ with radius function $\rho = \sqrt{(N^2 - (Q + W)^2)(N^2 - (Q - W)^2)}$. For $0 < |Q| < N$ this surface is smoothly embedded. However, if $Q = 0$ this surface is not smoothly embedded, but is pointed at the poles such that in a small neighborhood of $(W = \pm N)$ the embedded (W, δ_W) surface is a cone (Fig. 19(b) Right).

Both the cylinder with ends identified and the $Q = 0$ surface in (3) are homeomorphic to the sphere.

C. The definition of the classical spectrum

The classical (second order) spectrum [41] at a given N is defined by the set of all admissible values of Q and h_2 . Since Q is restricted such that $-N \leq Q \leq N$ the spectrum is confined to lie within this interval. At fixed N and Q , the upper and lower boundaries of the spectrum are given by the maximum and minimum values of h_2 , which is a continuous and bounded function on the (W, δ_W) surface. It follows that the classical spectrum is a closed and bounded subsection of the (Q, h_2) plane. To every point (Q, h_2) in the classical spectrum there corresponds a joint level set in the four dimensional phase space Γ_N , and Γ_N is the union of those level sets. Each level set may be connected or disconnected, and we define the classical degeneracy of the joint level set of (Q, h_2) as the number of its disjoint components. In Fig. 22 each joint level set

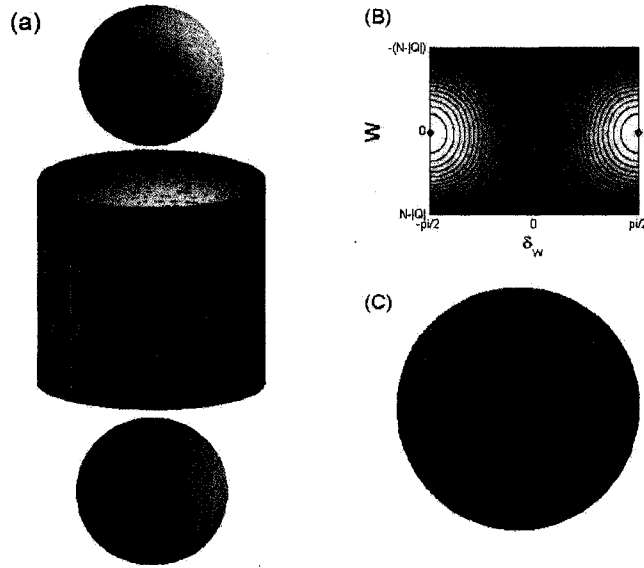


FIG. 20: The (W, δ_W) surface $\Gamma_{N,Q}$ is depicted as a two-dimensional surface in a fictitious three-dimensional space in two manners. The canonical coordinates on $\Gamma_{N,Q}$ are W with $-(N - |Q|) \leq W \leq (N - |Q|)$, and a π periodic coordinate δ_W with $-\pi/2 \leq \delta_W < \pi/2$ (undefined at $W = \pm(N - |Q|)$). (a) The canonical 2-form appropriate for the primitive action integrals is $dW \wedge d\delta_W$ and is equal to the differential of the surface area of the cylinder of radius $\rho = 1/2$ and height $L = 2(N - |Q|)$. Cutting this cylinder along $\delta_W = \pm\pi/2$ and unrolling the surface yields the flat contour map in (b). The upper and lower boundaries of the cylinder each represent a single point. Such is the topology of a surface of a sphere. (c) $\Gamma_{N,Q}$ is depicted by a sphere of radius $N - |Q|$ with $W = \xi_3$ and $\delta_W = \tan^{-1}(\xi_2/\xi_1)/2$. However, the differential of the spherical surface area is $2(N - |Q|)dW \wedge d\delta_W$. On the sphere, all contours that do not contain a fixed point may be regarded as librators, but in the flat representation, the contours can form either apparent librators or apparent rotators.

having h_2 less than the energy of the x-point corresponds to two contours (a “northern” and a “southern”), and is classically doubly degenerate.

D. Connected components of the (Q, h_2) level sets

For many points of the spectrum, each connected component of the corresponding (Q, h_2) joint level set in Γ_N is a 2-torus. Each individual 2-torus has the coordinates σ_Q (see Section X A), and a second periodic coordinate σ_W which increases uniformly

with time around the h_2 contour on the (W, δ_W) surface. However, for some level sets, one or more of its connected components may not be a 2-torus. A component of the (Q, h_2) joint level set is not a 2-torus if its intersection with the (W, δ_W) surface (i) contains a relative fixed point where Eqs. 58 vanish, or (ii) passes through one of the four points (Q, W) where the Pauli orbit degenerates to a point (at $Q = \pm N$, or $Q = 0$ and $W = \pm N$, see Fig. 18). All spectrum points (Q, h_2) for which the joint level set is not composed entirely of 2-tori are marked on the plots of classical spectra with either dashed (red or magenta online) curves or (cyan online) diamonds [42]. (i) and (ii) imply that when a component of a joint level set is not a 2-torus, its structure may be discerned from its intersection with $\Gamma_{N,Q}$.

For components which contain a non-polar relative fixed point on $\Gamma_{N,Q}$, its structure is determined by analysis of the linear stability matrix. Its eigenvalues are given by:

$$\lambda_{\pm} = \pm 2|\alpha|\sqrt{2\cos(2\delta_W)}\sqrt{\frac{\beta}{\alpha}\Lambda + \cos(2\delta_W)}\left[3W^2 - N^2 - Q^2 - \frac{2W^2(W^2 - N^2 - Q^2)^2}{\Lambda^2}\right]$$

$$\Lambda = \sqrt{(N^2 - (Q + W)^2)(N^2 - (Q - W)^2)}$$
(61)

When Eq. 61 is imaginary (real) the relative fixed point is an o-point (x-point).

Components of (Q, h_2) level sets with $0 < |Q| < N$, that appear as an o-point on the (W, δ_W) surface, have the simple structure of a smooth 1-torus (a Pauli orbit). However, components whose intersection contains an x-point have a complex structure resembling a ‘figure eight’ crossed with a circle.

Additional types of complex components are found at $Q = 0$. In Section X A we determined that for $Q = 0$, the Pauli orbit at either pole ($W = \pm N$) is a point. Therefore, any component of a $(Q = 0, h_2)$ level set that contains a pole cannot be a 2-torus. For some **F** and **B**, the value of $h_2(Q = 0, W = \pm N)$ is a local extremum, and

these points are isolated, effectively forming o-points [43] at a pole of $\Gamma_{N,Q}$. However, for some field parameters, there are components of level sets at $Q = 0$ which form an extended contour passing through one or both of the poles of the (W, δ_W) surface. Since there are δ_Q rings present at all points of the contour except the poles, any such component of a level set must contract to a point as it passes through either pole. A component of a level set of (Q, h_2) which passes through either $W = N$ or $W = -N$ or both, is a pinched 2-torus, with a pinch point at each pole it passes through (Fig. 21).

XI. MONODROMY OF ACTIONS

In this section we examine the properties of the classical actions as functions of Q and h_2 . Those (Q, h_2) level sets in Γ_N with components that are 2-tori may form: (a) a single simply-connected family; (b) a single multiply-connected family; (c) two (or more) disjoint families, each of which may be either simply or multiply-connected. In a sufficiently small neighborhood of Γ_N about any one 2-torus, one can always construct local smooth action and angle variables [44]. However we must carefully distinguish between locally smooth action variables and what we refer to as primitive action integrals. The primitive action integrals are simply areas on Poincaré surfaces divided by 2π . However, for some \mathbf{F} and \mathbf{B} , these are not smooth functions of Q and h_2 .

In this section we will first compute the two primitive action integrals associated with each 2-torus, and find that they have discontinuous derivatives as functions of the constants of the motion. We then show how to obtain smooth action variables from the primitive actions by continuation. The resulting functions are locally smooth functions of the constants of the motion, but if a family of tori is multiply-connected, it may be impossible to construct a single valued and smooth action variable on the entire family. When this is the case, smooth continuation of a local action variable leads to a globally multivalued function on the classical spectrum. Whenever smooth continuation of an

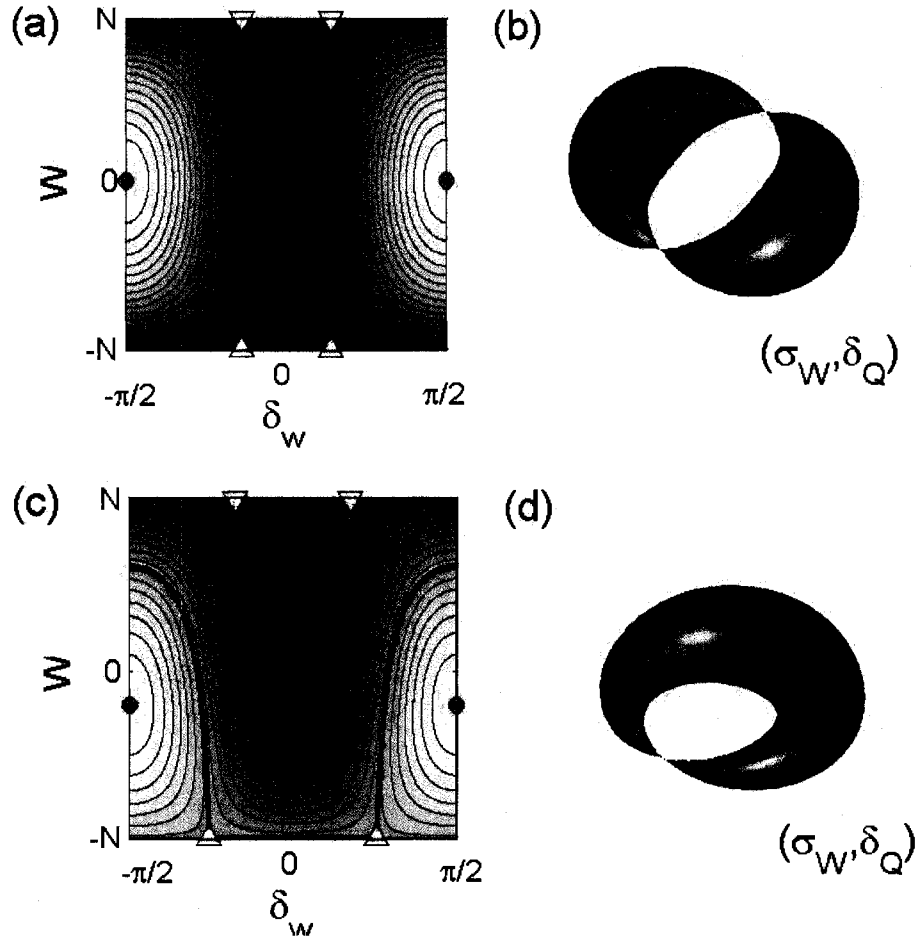


FIG. 21: (color online) For some \mathbf{F} and \mathbf{B} there exist components of (Q, h_2) level sets which are pinched 2-tori at $Q = 0$. (a) Contours of constant h_2 on the unrolled cylinder representation of the (W, δ_W) surface for $Q = 0$, $\chi = 0$ and $\theta_1 < \theta < \theta_2$. A particular contour for which $\partial h_2 / \partial W = 0$ on each of its points is highlighted (red online). This level set meets the north and south poles ($W = \pm N$) at T-points which are marked with (yellow online) triangles. All points (W, δ_W) for which $|W| < N$ are crossed with a circle having the coordinate δ_Q . However, at the poles $W = \pm N$, no such circle exists. (b) Therefore the corresponding level set has the topology of a doubly pinched torus. Everywhere except at the poles it is a smooth two dimensional surface. Coordinates on the two dimensional sections of this surface are (σ_W, δ_Q) , where σ_W is a coordinate around the contour on the (W, δ_W) surface. (c) These contours are obtained from contours similar to (a) by tilting the fields from perpendicular such that $\chi / \omega_f N^3 = 0.2$. The contour which passed through both poles at perpendicular fields divides into the two highlighted (red online) contours at different energies for non-zero χ . (d) The doubly pinched torus in perpendicular fields is split into two singly pinched tori at different energies when the fields are tilted.

action variable around some closed loop in the classical spectrum brings that action variable back to a new value, the system is said to have “nontrivial monodromy of action and angle variables”, or simply, “monodromy”.

A. Primitive action integrals

To construct primitive actions, we consider the intersection of each (Q, h_2) 2-torus with two fixed Poincaré surfaces, and integrate the canonical 2-form Eq. 59 over the area in the Poincaré surface which is bounded by the intersection contour. The two Poincaré surfaces are chosen to be (i) the (Q, σ_Q) surface, and (ii) the (W, δ_W) surface. By inspecting Fig. 18, it can be seen that for $0 < |W| < N$ the (Q, σ_Q) surface is a cylinder which is capped by rings of ψ_1 and ψ_2 at either end, while at $W = 0$ it is connected like a sphere.

The intersection of a (Q, h_2) torus with surface of section (i) is a ring with coordinate σ_Q , and the integral of Eq. 46 over a surface bounded by the Pauli orbit may be taken to be [45],

$$J_Q(Q, h_2) = Q \tag{62}$$

Thus, Q is simultaneously a conserved quantity, a primitive action, and a locally smooth action variable near every torus.

The definition of the other action is complicated because the (W, δ_W) surface is connected like a sphere, and because the area of that surface is not a smooth function of Q near $Q = 0$.

Consider a level set of the fully reduced Hamiltonian on the (W, δ_W) surface defined by the equation $h_2 = E_2$. The level set may consist of a single connected component, or multiple disjoint components on the surface. Each disjoint component may or may not contain a relative fixed point, where Eqs. (4.2) vanish. If a disjoint component does not contain a fixed point and does not pass through the north or south pole at $Q = 0$,

it forms a smooth one-dimensional closed curve on the (W, δ_W) surface [46]. Each such curve (i) divides the (W, δ_W) surface into two areas, and (ii) forms a corresponding contour on the unrolled cylinder which is either an apparent librator or an apparent rotator (Fig. 20). The two areas created on the cylinder by such a contour must sum to the total (W, δ_W) surface area $2\pi(N - |Q|)$, and are identified with the areas inside and outside the contour of an apparent librator, or above and below the contour of an apparent rotator.

The classical action integral is defined for each apparent rotator or librator and is directly proportional to the canonical area $dW \wedge d\delta_W$ which is bounded by the level curve of h_2 on the (W, δ_W) surface. The topology of this surface implies that there are two equally valid areas, which in general have different values. Thus we define for each disjoint smooth curve of the level set $h_2 = E_2$, two equally valid action integrals which we refer to as primitive actions [47]:

$$J_+(h_2; N, Q) = \frac{1}{2\pi} \int_{A_+(h_2)} dW \wedge d\delta_W \quad (63a)$$

$$J_-(h_2; N, Q) = \frac{1}{2\pi} \int_{A_-(h_2)} dW \wedge d\delta_W \quad (63b)$$

The integral is over the area of the (W, δ_W) surface which is bounded by the curve of constant h_2 , and the + and - subscripts have the following meaning. Each apparent rotator or librator is a contour which bisects the total phase space into two areas A_1 and A_2 , such that $A_1 + A_2 = 2\pi(N - |Q|)$ (Fig. 22). Then, the functions in Eqs. 63 could have been defined as $J_1(h_2) = A_1/2\pi$ and $J_2(h_2) = A_2/2\pi$. However, since the sum of the areas is fixed, and no two level sets can intersect, one of the two functions J_1, J_2 is an increasing function of h_2 while the other is a decreasing function. We denote the increasing function $J_+(h_2) = A_+/2\pi$, and the decreasing function $J_-(h_2) = A_-/2\pi$.

As was previously mentioned, for some values of h_2 , there may be multiple contours which are mutually disjoint, but have the same constant value $h_2 = E_2$ (Fig. 22). Since

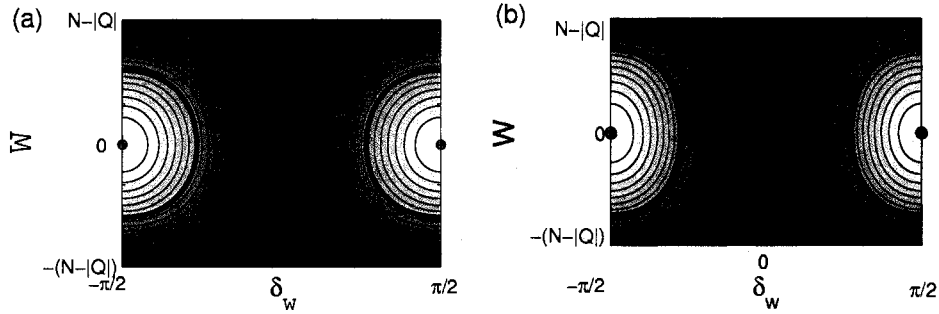


FIG. 22: (Color online) Contours of the Hamiltonian h_2 on the unrolled cylinder representation of the (W, δ_W) surface at $\theta = 5^\circ$, $N = 15$, $\chi = 0$ and, (a) $Q = 0$, and (b) $Q = 4$. The surface has the topology of a sphere such that left and right edges are identified, and the top and bottom edges each consist of a single point. Darker regions indicate lower energies, points indicate fixed points, an x-point separatrix is marked (red online) as are three other disjoint contours (blue online). At $Q = 0$ in (a), fixed points are present, but not marked at $W = \pm N$. As Q increases to $Q = 4$ in (b), these o-points migrate from the poles toward the equator ($W = 0$) along $\delta_W = 0$, to form the two additional o-points marked in (b). Each disjoint contour of h_2 which does not contain a fixed point forms either an apparent rotator or an apparent librator, bisecting the total phase space into two areas A_1 and A_2 , such that $A_1 + A_2 = 2\pi(N - |Q|)$. An appropriate action is defined by either $J_1(h_2) = A_1/2\pi$ or $J_2(h_2) = A_2/2\pi$. We identify the J which increases with energy as J_+ , and that which decreases with energy as J_- . For each energy greater than that of the separatrix, there is a single apparent librator, localized about the maximal energy o-point at $W = 0$, $\delta_W = \pm\pi/2$. Each librator admits the construction of two actions. If A_1 is the area containing the maximal o-point, then $J_- = A_1/2\pi$ is the strictly decreasing function of energy, while $J_+ = A_2/2\pi$ is strictly increasing. For all energies below that of the separatrix, there are two disjoint contours having the same value of h_2 (a classical double degeneracy). One contour C_N is localized in the “north” ($W > 0$), while the other C_S is in the “south” ($W < 0$). In such a case, both $J_+(h_2)$ and $J_-(h_2)$ are defined for each disjoint contour. For C_N , let A_2 be the area containing the minimal energy o-point (which is located at (a) the north pole for $Q = 0$, and (b) at $W \approx 9$, $\delta_W = 0$ for $Q = 4$). Then $J_+^{(N)} = A_2/2\pi$ is the strictly increasing function of h_2 , while $J_-^{(N)} = A_1/2\pi$ is strictly decreasing. Similarly for C_S , if A_2 contains the minimal energy at or near the south pole, $J_+^{(S)} = A_2/2\pi$, while $J_-^{(S)} = A_1/2\pi$.

each of the individual contours C_i that does not contain a fixed point bisects the (W, δ_W) surface, it follows that for every such contour C_i there exists a pair of functions $J_+^{(i)}$ and $J_-^{(i)}$, given by Eqs. 63.

It follows directly from the above discussion that J_+ and J_- cannot both be smooth functions of Q near $Q = 0$. Since the total canonical area on $\Gamma_{N,Q}$ is $\pi 2(N - |Q|)$, by their definitions (Eqs. 63):

$$J_+ + J_- = N - |Q| \quad (64)$$

The derivative with respect to Q of the right hand side of Eq. 64 is not continuous at $Q = 0$. Therefore either J_+ , or J_- , or both, must have a discontinuous derivative with respect to Q at $Q = 0$.

In Fig. 23 we consider a classical spectrum for nearly perpendicular fields. Each point of the dashed red boundary represents a 1-torus. The (cyan online) diamonds each represent a singly pinched torus. All points inside the (red online) dashed boundary, but excluding the two points marked by the (cyan online) diamonds, represent a 2-torus. From each 2-torus we may construct the primitive actions J_+ and J_- and plot their contours. In Fig. 23(a) the contours of $J_+(Q, h_2)$ are smooth for all points on the spectrum except along $Q = 0$, where they are only smooth for energies less than the energy of the lower diamond. At energies above the lower diamond, $\partial J_+/\partial Q$ has a jump discontinuity at $Q = 0$. The magnitude of the jump is greater above the upper diamond. In Fig. 23(b) we plot the contours of $J_-(Q, h_2)$, and find an analogous situation. Here the contours are smooth at energies higher than the upper diamond, and the magnitude of the jump discontinuity increases as we pass each diamond to lower energies.

We can understand the behavior of such discontinuities quantitatively by examining the area generated by level curves of h_2 on a family of schematic cylinders parameterized by Q (Fig. 24).

Consider a family of level sets with a fixed value of h_2 , ranging over an infinitesimal interval of Q , centered about $Q = 0$. This family will intersect $\Gamma_{N,Q}$ at each Q of the infinitesimal interval, forming a contour on its cylindrical representation (Fig. 24). If no member of this family contains a fixed point, or passes through $W = \pm N$, then either all members of the family form apparent rotators, or all members form apparent librators on the cylindrical representation of the $\Gamma_{N,Q}$.

Each apparent rotator (Fig. 24a) has one associated area which contains one pole, and a complementary area containing the other pole. Since the coordinates on the cylinder are W with $-(N - |Q|) \leq W \leq (N - |Q|)$, and δ_W with $-\pi/2 \leq \delta_W < \pi/2$,

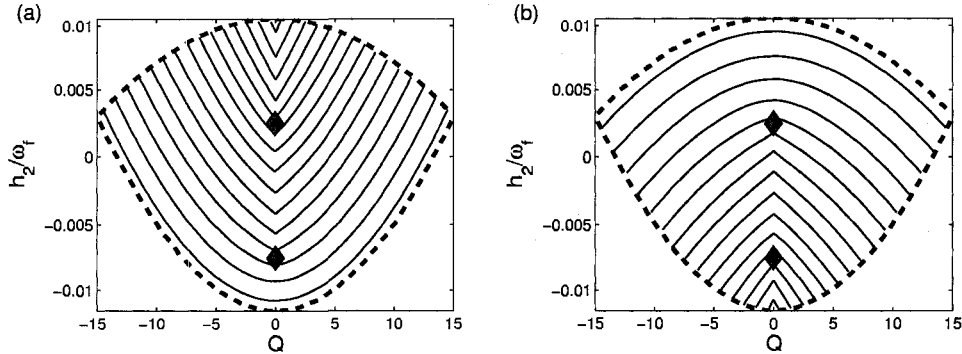


FIG. 23: (color online) Contours of the primitive actions are plotted on a classical spectrum in near perpendicular fields with $N = 15$, $\theta = 50^\circ$, $\omega_f = 10^{-6}$, $\chi/\omega_f N^3 = 0.2$. All points interior of the dashed red boundary and excluding the points marked by the (cyan online) diamonds represent a 2-torus with coordinates (σ_Q, σ_W) . The $\Gamma_{N,Q}$ located at $Q = 0$ is plotted in Fig. 21(c) and we identify each of the (cyan online) diamonds with a singly pinched torus. The primitive actions $J_+(Q, h_2)$ and $J_-(Q, h_2)$ are defined on each 2-torus but may not be smooth at $Q = 0$. (a) $\partial J_+/\partial Q$ is continuous across $Q = 0$ at energies less than that of the low energy singly pinched torus. But at all greater energies, $\partial J_+/\partial Q$ has a jump discontinuity. (b) $\partial J_-/\partial Q$ is continuous across $Q = 0$ at energies greater than that of the high energy singly pinched torus, but has a jump discontinuity at all lower energies. Such structure in the primitive actions can be quantitatively determined for any field parameters by examining the behavior of the joint level sets of (Q, h_2) at fixed h_2 in a neighborhood of Q centered about $Q = 0$.

the complementary areas are:

$$A_{rot}^{above} = \pi(N - |Q|) - \int_{-\pi/2}^{\pi/2} W d\delta_W = 2\pi J_{rot}^{above} \quad (65a)$$

$$A_{rot}^{below} = \pi(N - |Q|) + \int_{-\pi/2}^{\pi/2} W d\delta_W = 2\pi J_{rot}^{below} \quad (65b)$$

The value of the integral $I = \int W(h_2; Q) d\delta_W$ is a smooth function of Q provided that the level set of h_2 does not contain a fixed point. It follows that for a family of apparent rotators, both $\partial J_+/\partial Q$ and $\partial J_-/\partial Q$ include a term equal to $-\frac{1}{2}\text{sign}(Q)$, and therefore are discontinuous at $Q = 0$.

Each apparent librator (Fig. 24(b)) has one associated area which contains neither the north nor the south pole, while the complementary area contains both.

$$A_{lib}^{inside} = \oint W d\delta_W = 2\pi J_{lib}^{inside} \quad (66a)$$

$$A_{lib}^{outside} = 2\pi(N - |Q|) - \oint W d\delta_W = 2\pi J_{lib}^{outside} \quad (66b)$$

Again the integral is smooth provided the level set does not contain a fixed point, and it follows that the primitive action associated with the area inside the apparent libration has a smooth derivative with respect to Q at $Q = 0$, while $\partial J^{outside}/\partial Q$ contains a term equal to $-sign(Q)$ and is therefore discontinuous at $Q = 0$. If a family of librations encircles a minimum of h_2 , J_+ will pass smoothly through $Q = 0$, while if the family encircles a maximum, J_- will be smooth.

Thus we conclude the following: (i) $\partial J_{+/-}/\partial Q$ has a jump discontinuity at $Q = 0$ described by a term $-\frac{1}{2}sign(Q)$ for each pole the associated area contains. (ii) For apparent rotators both the J_+ and J_- areas contain one pole. (iii) For apparent librations encircling a maximum, the J_- area does not contain any pole while the J_+ area contains both. (iv) For apparent librations encircling a minimum, the J_+ area does not contain any pole while the J_- area contains both. We can summarize these conclusions compactly by:

$$\frac{\partial J_{+/-}}{\partial Q} = -\frac{z_{+/-}}{2}sign(Q) + (smooth) \quad (67)$$

where:

$$z_+ = \begin{cases} 1 & \text{Rotators} \\ 0 & \text{Librators encircling a minimum} \\ 2 & \text{Librators encircling a maximum} \end{cases} \quad (68a)$$

$$z_- = \begin{cases} 1 & \text{Rotators} \\ 2 & \text{Librators encircling a minimum} \\ 0 & \text{Librators encircling a maximum} \end{cases} \quad (68b)$$

The types of apparent families present near $Q = 0$ depends on \mathbf{F} and \mathbf{B} and can be determined for all field parameters by analysis of the fully reduced Hamiltonian.

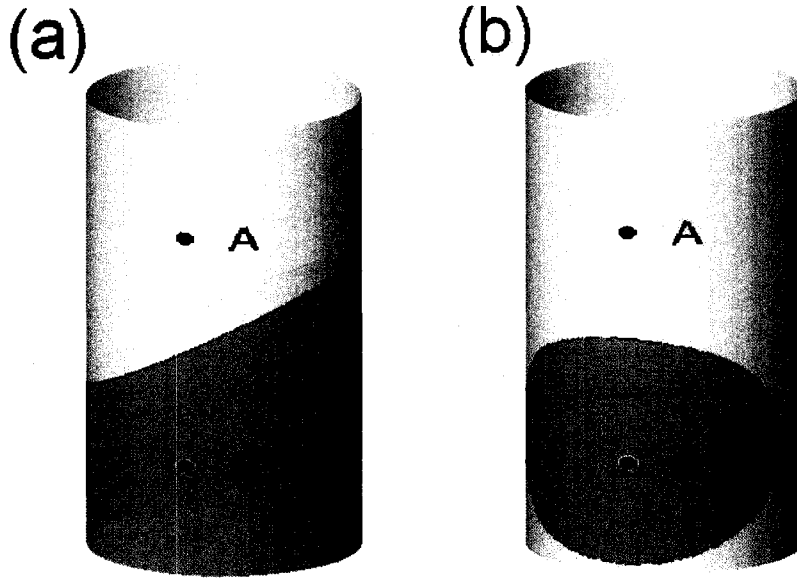


FIG. 24: Most level sets of the second order Hamiltonian h_2 form apparent rotators or apparent librators on a schematic cylinder representation of a (W, δ_W) surface, parameterized by Q . Two points marked A and B schematically represent those o-points of h_2 which attain extremal values on the (W, δ_W) surface. By interchangeably associating these points with a maximum and minimum, one gains insight into the properties of the actions J_+ and J_- as functions of Q by investigating the properties of the areas. In general, the contours of h_2 are smooth curves on the cylindrical surface which are also smooth functions of Q . However, the height of the cylinder is $2(N - |Q|)$, which has a discontinuous derivative with respect to Q at $Q = 0$. (a) The contour of an apparent rotator divides the phase space into two halves. Although the contour itself is a smooth function of Q , both the shaded and unshaded areas are not smooth at $Q = 0$. Since the coordinate W is zero at the equator of the cylinder, the shaded area is $\pi(N - |Q|) + \int W d\delta_W$, and the unshaded area is $\pi(N - |Q|) - \int W d\delta_W$. The value of the integral $I = \int W(h_2; Q) d\delta_W$ is a smooth function of Q provided the level set of h_2 does not contain a fixed point. Therefore, at $Q = 0$, both areas of an apparent rotator have a discontinuity in derivative with respect to Q equal to $-\pi \text{sign}(Q)$. (b) For an apparent liblator, the shaded area is $2\pi J$, where $J = J_+$ if B is a minimum, and $J = J_-$ if B is a maximum. This area is a smooth function of Q . The unshaded area is equal to $2\pi(N - |Q| - J)$ and is composed of a part that is smooth and a part that has a discontinuity in slope equal to $-2\pi \text{sign}(Q)$ at $Q = 0$. Using only these observations and a map of the contours of h_2 at $Q = 0$, one may determine the discontinuities which appear in J_+ and J_- for all parameters.

Let us look back to Figs. 23(a,b). If we investigate the corresponding contours of the Hamiltonian on $\Gamma_{N,Q}$ (plotted at $Q = 0$ in Fig. 21(c)), we find that near $Q = 0$ and energies greater than that of the upper diamond, the level sets form families of apparent

librators which contain a maximum of h_2 . At energies less than the lower diamond the families form apparent librators containing a minimum. Meanwhile at energies which lie between the diamonds, there are families of apparent rotators. The patterns in the magnitudes of the discontinuities are explained by Eqs. 67 and 68.

B. Intrinsically multivalued smooth classical action variables

In order to construct a smooth classical action variable, a discontinuous primitive action must be smoothly continued across $Q = 0$. If we interpret the primitive action $J_{+/-}(Q, h_2)$ as the principal branch of a smooth, but intrinsically multivalued action variable, then at each crossing of $Q = 0$ at energies for which $z_{+/-}$ is nonzero, a new branch of $J_{+/-}(Q, h_2)$ is encountered. Each new branch consists of the old branch plus an additional term:

$$J_+^{continued} = J_+^{old} + \text{sign}(Q)z_+Q \quad (69a)$$

$$J_-^{continued} = J_-^{old} + \text{sign}(Q)z_-Q \quad (69b)$$

where $z_{+/-}$ is given by Eqs. 68. The additional terms in the new branches repair the intrinsically discontinuous slope at $Q = 0$ (Eq. 67) but may introduce a multivalued smooth classical action variable if a single sheet cannot be used to cover an entire spectrum. In Fig. 25 the principal action J_+ is continued across $Q = 0$ into $Q < 0$ at energies which have two different values of z_+ . In both cases it is impossible to cover the entire spectrum with a single valued and smooth classical action variable.

C. Monodromy and vector transport

To classify classical spectra, we consider the smooth transport of two independent vectors tangent to contours of locally smooth action variables. Let (\hat{Q}, \hat{h}_2) be unit

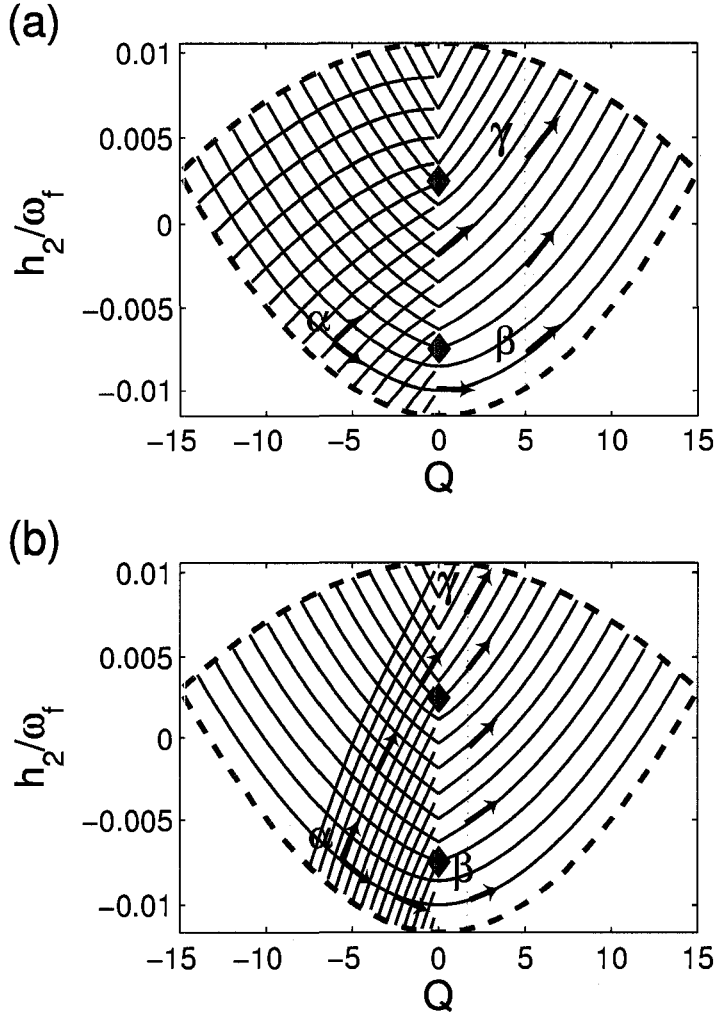


FIG. 25: (color online) Contours of the primitive action $J_+(Q, h_2)$ and its smooth continuation into negative Q are plotted on the classical spectrum. $N = 15$, $\theta = 50^\circ$, $\omega_f = 10^{-6}$, $\chi/\omega_f N^3 = 0.2$. Lighter contours are of the principal branch and the additional darker contours are of the first continued branch encountered when smoothly continuing across $Q = 0$ into $Q < 0$. (a) Here the contours are continued through the rotators where $z_+ = 1$, such that J_+ is smoothly joined to the branch $J_+ - Q$ at $Q = 0$ for energies which lie between the two (cyan online) diamonds. (b) Here the contours are continued through the librators where $z_+ = 2$ such that J_+ is smoothly joined to the branch $J_+ - 2Q$ at $Q = 0$ for energies which lie above the upper (cyan online) diamond. To classify this classical spectrum, consider the smooth transport of vectors tangent to the spectrum about the counterclockwise, closed loops marked $\alpha\beta\gamma$. In both (a) and (b), there is a passage to a second branch at $Q = 0$ between γ and α such that the vector does not return to itself at α . The angle of rotation is greater when the loop encircles both (cyan online) diamonds in (b).

vectors in the tangent space of the spectrum. Vectors \mathbf{t} which are tangent to contours of the primitive actions (Eqs. 63 and 62) are (with arbitrary orientation convention):

$$\mathbf{t}_+ = \frac{\partial J_+}{\partial h_2} \hat{Q} - \frac{\partial J_+}{\partial Q} \hat{h}_2 \quad (70a)$$

$$\mathbf{t}_- = \frac{\partial J_-}{\partial h_2} \hat{Q} - \frac{\partial J_-}{\partial Q} \hat{h}_2 \quad (70b)$$

$$\mathbf{t}_Q = \hat{h}_2 \quad (70c)$$

Vectors which are tangent to contours of the smoothly continued action are given by:

$$\mathbf{t}_+^{continued} = \frac{\partial J_+}{\partial h_2} \hat{Q} - \left[\frac{\partial J_+}{\partial Q} + \text{sign}(Q) z_+ \right] \hat{h}_2 \quad (71a)$$

$$\mathbf{t}_-^{continued} = \frac{\partial J_-}{\partial h_2} \hat{Q} - \left[\frac{\partial J_-}{\partial Q} + \text{sign}(Q) z_- \right] \hat{h}_2 \quad (71b)$$

The vectors in Eqs. 71 differ from the vectors tangent to the primitive actions (Eqs. 70) by a vector tangent to contours of constant Q with integer magnitude.

$$\mathbf{t}_+^{continued} - \mathbf{t}_+ = -\text{sign}(Q) z_+ \hat{h}_2 = -\text{sign}(Q) z_+ \mathbf{t}_Q \quad (72a)$$

$$\mathbf{t}_-^{continued} - \mathbf{t}_- = -\text{sign}(Q) z_- \hat{h}_2 = -\text{sign}(Q) z_- \mathbf{t}_Q \quad (72b)$$

These equations imply that if a primitive action $J_{+/-}$ is smoothly continued across $Q = 0$, a vector tangent to its continued contours is rotated with respect to a vector tangent to the primitive $J_{+/-}$ contours at the same point. The transformation between the vectors tangent to the primitive contours Q and $J_{+/-}$, and vectors tangent to the continued contours can be written in matrix form:

$$\begin{bmatrix} \mathbf{t}_Q^{continued} \\ \mathbf{t}_{+/-}^{continued} \end{bmatrix} = \begin{bmatrix} 1 & 0 \\ -z_{+/-} \text{sign}(Q) & 1 \end{bmatrix} \begin{bmatrix} \mathbf{t}_Q \\ \mathbf{t}_{+/-} \end{bmatrix} \quad (73)$$

Looking back to Fig. 25, the consequences of Eq. 73 for smooth transport of vectors about a closed loop is illustrated by a series of arrows. At point α in Fig. 25(a), the

vector $\mathbf{v}_2 = \mathbf{t}_+$ is tangent to contours of J_+ and is transported along that contour to point β . Then this vector is transported along the contour $Q = 5$ to γ . To smoothly transport back to α , we must pass to the first continued branch of the multivalued action at $Q = 0$. As a result, when \mathbf{v}_2 returns to point α it has been transformed. In contrast, if we transport the vector $\mathbf{v}_1 = \mathbf{t}_Q$ about the same closed loop, \mathbf{v}_1 returns identically to itself. Using Eq. 73 the transformation of the vectors \mathbf{v}_1 and \mathbf{v}_2 is equivalent to multiplication by the matrix $M_1 = [1, 0; 1, 1]$ written in the basis $\{\mathbf{v}_1, \mathbf{v}_2\}$ at α .

$$M_1 = \begin{bmatrix} 1 & 0 \\ 1 & 1 \end{bmatrix}, \{\mathbf{v}_1, \mathbf{v}_2\} = \left\{ \begin{bmatrix} 1 \\ 0 \end{bmatrix}, \begin{bmatrix} 0 \\ 1 \end{bmatrix} \right\} \quad (74)$$

Such a transformation occurs for transport about any counterclockwise closed loop encircling the lower (cyan online) diamond. Similar considerations applied to the closed loop $\alpha\beta\gamma$ in Fig. 25(b) yields a transformation equivalent to multiplication by the matrix M_2 in the same basis, where:

$$M_2 = \begin{bmatrix} 1 & 0 \\ 2 & 1 \end{bmatrix} \quad (75)$$

To fully classify this spectrum we consider all possible closed loops. Similar analysis applied to counterclockwise loops encircling the upper diamond yields Eq. 74 again. Any clockwise traversal of a loop encircling a single diamond yields the matrix inverse to M_1 , $M_1^{-1} = M_{-1} = [1, 0; -1, 0]$, while any encircling both diamonds will yield M_2^{-1} . Finally, transport about any loop which begins and ends on the same branch will result in a transformation described by the identity matrix $E = [1, 0; 0, 1]$. This exhausts all possible closed loops for any spectrum which is topologically equivalent to that in Fig. 25, as any possible loop is equivalent to some combination of these basis loops. Thus any spectrum having two singly pinched tori at different energies is classified by listing the three matrices $\{M_1, M_2, E\}$.

In this manner, spectra for any weak, nearly-perpendicular \mathbf{F} and \mathbf{B} (such that $|\chi| \lesssim \omega_f N^3 \ll 1$) are classified by a list of matrices which describe the effects of smooth

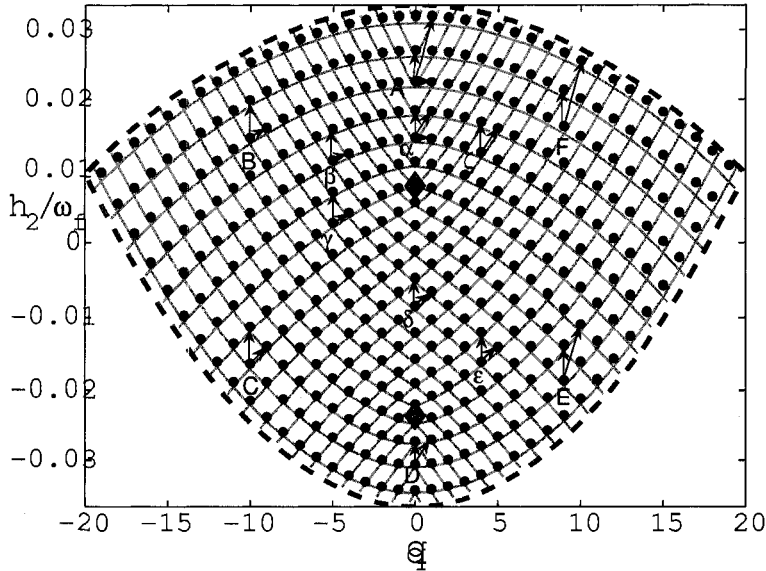


FIG. 26: (color online) Type *II* spectrum. The spectrum h_2 versus q for $\chi/\omega_f n^3 = 0.2$, $n = 20$, $F = 146$ V/cm, $B = 0.302$ T, or $\theta = 50^\circ$ and $\omega_f = 10^{-6}$. The quantum basis included n manifolds from 18 to 22. The (blue online) circular dots are derived from quantum calculations, while all other structures are derived from classical perturbation theory and semiclassical quantization of actions. Two independent monodromy circuits are marked by sequences of letters. A $[1, 0; 2, 1]$ defect is characterized by lattice vector transport of $\{\mathbf{v}_1, \mathbf{v}_2\}$ along locally smooth action contours connecting points marked by the Latin letter cycle *ABCDEF*A. This circuit encircles both point defects and after a complete circuit has been made, \mathbf{v}_1 returns to the vector $\mathbf{v}_1 + 2\mathbf{v}_2$ depicted in gray at point A. A $[1, 0; 1, 1]$ defect is characterized by transport of $\{\mathbf{v}_1, \mathbf{v}_2\}$ along smooth contours connecting points marked by the sequence of Greek letters $\alpha\beta\gamma\delta\epsilon\zeta\alpha$. When a complete circuit has been made \mathbf{v}_1 returns to the vector $\mathbf{v}_1 + \mathbf{v}_2$ depicted in gray at point α .

vector transport about all possible closed loops on the spectrum. By Eq. 73 the values of the components of the matrices are determined by the structure of the Hamiltonian h_2 on $\Gamma_{N,Q}$ in an infinitesimal neighborhood near $Q = 0$ through Eqs. 68.

As an alternative to smooth continuation of the primitive actions, one may transform between any overlapping smooth action functions. For example when continuing around a 2 defect in regions *II* or the $\perp M.Int$ interval, it is easiest to visualize the transport of tangent vectors along the smooth contours J_+ below the defect point, and along contours of J_- above (See Fig. 26).

XII. MULTIVALUED ACTIONS AND QUANTUM LATTICE DEFECTS

The connection between the classical system and quantum calculations is through the EBKM quantization of the actions. In this section we will see how each resulting semiclassical ‘state’ is associated with quantized values of the constants of the motion, and an associated point in a classical spectrum. A collection of such points forms a lattice of points in the spectrum. When a classical spectrum has an intrinsically multivalued action, the associated lattice has a defect. In this section we also consider the appropriate quantum operators having expectation values which correspond with the quantized constants of the motion. Through this connection, quantum spectra in near perpendicular fields are classified by the presence of monodromy.

A. EBKM Quantization

Quantization of primitive classical actions selects those classical tori which correspond to approximate quantum energy eigenvalues. The semiclassical quantization conditions are:

$$N = n = 1, 2, 3, \dots \quad (76a)$$

$$Q = q = -(n-1), -(n-2), \dots, (n-1) \quad (76b)$$

Comparing semiclassical with calculated quantum spectra, we find that either of the primitive actions J_+ or J_- is quantized as half integers:

$$J_{+/-} = k + \frac{1}{2}$$

$$k = 0, 1, \dots, n - |q| - 1 \quad (76c)$$

Thus, in a primitive semiclassical approximation, a quantum state is associated with each contour of h_2 with J_+ or J_- quantized as in Eq. 76c on each $\Gamma_{N,Q}$ at quantized

values of N and Q as in Eqs. 76a,76b such that $\Gamma_{N,Q} = \Gamma_{n,q}$. As an example, consider the case $\mathbf{B} = 0$ and \mathbf{F} parallel to the x-axis where Eq. 57 is reduced to:

$$h_{Stark} = -\frac{1}{2N^2} + \frac{3NF}{2}Q - \frac{N^4F^2}{16} [17N^2 - 3Q^2 - 9W^2] \quad (77)$$

This Hamiltonian is independent of δ_W such that W is a constant. Then it follows from definitions (4.4) that for $B = 0$, $J_+^{(N)} = J_+^{(S)} = (N - |Q| + |W|)/2$, and $J_-^{(N)} = J_-^{(S)} = (N - |Q| - |W|)/2$. Either of these equations and the EBKM quantization conditions Eqs. 76 imply $N = n$, $Q = q$ and $W^2 = (2k + 1 - n + |q|)^2$ where $k = 0, 1, 2, \dots, n - |q| - 1$. Subsequent substitution into the Hamiltonian h_{Stark} above yields an EBKM spectrum which only differs from the well known formulae [48] by a quantum correction $19N^4F^2/16$.

B. Quantum operators

To obtain a collection of quantum spectra for the crossed fields Hamiltonian (Eq. 20), we expand the wavefunction in a basis [21] of bound spherical eigenstates $|n, l, m\rangle$ of the unperturbed hydrogen Hamiltonian \hat{H}_0 , and compute the eigenvalues E_j and eigenvectors $|\Psi_j\rangle$ of the resulting matrix. There is good agreement between the obtained quantum eigenvalues and the primitive semiclassical energy eigenvalues for almost all states in weak near-perpendicular spectra.

On a finite basis of bound eigenstates of \hat{H}_0 , the matrix \hat{H}_0 possesses a well defined inverse \hat{H}_0^{-1} such that $\hat{H}_0\hat{H}_0^{-1} = \hat{H}_0^{-1}\hat{H}_0 = I$. The eigenvalues of \hat{H}_0 in the $|n, l, m\rangle$ bases are $E_n = -(2n^2)^{-1}$, and it follows that $\hat{H}_0^{-1}|n, l, m\rangle = -2n^2|n, l, m\rangle$. The existence of the inverse operator to \hat{H}_0 in the basis of bound states allows the definition of two additional operators which commute with each other and with \hat{H}_0 but do not commute with the full Hamiltonian [49]. These operators are the quantum analog of the canonical momenta in Eq. 44 and require the operator analogs of the angular momentum and

Runge-Lenz vectors. Classically the Runge-Lenz vector is defined:

$$\mathbf{A} = \mathbf{p} \times \mathbf{L} - \frac{\mathbf{r}}{|\mathbf{r}|} \quad (78)$$

The corresponding quantum operator must be Hermitian, and was defined by Pauli as [2]:

$$\hat{\mathbf{A}} = \frac{1}{2} \left(\hat{\mathbf{p}} \times \hat{\mathbf{L}} - \hat{\mathbf{L}} \times \hat{\mathbf{p}} \right) - \frac{\hat{\mathbf{r}}}{|\hat{\mathbf{r}}|} \quad (79)$$

By use of \hat{H}_0^{-1} one may extend Pauli's analysis to multiple n-manifolds by altering an operator he introduced with the replacement $-2n^2 \rightarrow \hat{H}_0^{-1}$:

$$\omega_f \hat{Q} = \frac{B}{2} \hat{L}_z + \frac{3F_x}{4} \hat{H}_0^{-1} \hat{A}_x \quad (80)$$

and we also define a related operator:

$$\omega_f \hat{W} = \frac{B}{2} \sqrt{-\frac{\hat{H}_0^{-1}}{2}} \hat{A}_z - \frac{3F_x}{2} \sqrt{-\frac{\hat{H}_0^{-1}}{2}} \hat{L}_x \quad (81)$$

From the fundamental canonical commutation relations and definitions 80 and 81 it follows that:

$$[\omega_f \hat{Q}, \omega_f \hat{W}] = 0 \quad (82a)$$

$$[\omega_f \hat{Q}, \hat{H}_0] = 0 \quad (82b)$$

$$[\omega_f \hat{W}, \hat{H}_0] = 0 \quad (82c)$$

Since both operators 80 and 81 commute with \hat{H}_0 they are diagonal in n , with eigenvectors that are linear combinations of the $|n, l, m\rangle$ states at a fixed n .

If we define the following function of n :

$$\omega_f(n) = \frac{1}{2} \sqrt{B^2 + (3nF)^2} \quad (83)$$

then the eigenvectors of $\omega_f \hat{Q}$ (Eq. 80) have the eigenvalues $\omega_f(n)q$ with $q = -(n-1), -(n-2), \dots, (n-1)$, while the eigenvectors of $\omega_f \hat{W}$ (Eq. 81) have the eigenvalues $\omega_f(n)w$ with $w = -(n-|q|-1), -(n-|q|-2), \dots, (n-|q|-1)$.

C. Quantum lattices

The second order (and higher) energy may be defined as:

$$h_2^j = \langle \Psi_j | \hat{H} | \Psi_j \rangle - \langle \Psi_j | \hat{H}_0 | \Psi_j \rangle - \langle \Psi_j | \omega_f \hat{Q} | \Psi_j \rangle \quad (84)$$

To scale these expectation values, define:

$$\bar{n}_j = \sqrt{-\frac{1}{2} \langle \Psi_j | \hat{H}_0^{-1} | \Psi_j \rangle} \quad (85)$$

The expectation value in Eq. 84 is scaled by substituting Eq. 85 into Eq. 83 and dividing Eq. 84 by the result.

$$\frac{h_2^j}{\omega_f} = \frac{1}{\omega_f(\bar{n})} \langle \Psi_j | [\hat{H} - \hat{H}_0 - \omega_f \hat{Q}] | \Psi_j \rangle \quad (86)$$

The scaled expectation value of the $\omega_f \hat{Q}$ operator is similarly defined as:

$$q_j = \frac{1}{\omega_f(\bar{n})} \langle \Psi_j | \omega_f \hat{Q} | \Psi_j \rangle \quad (87)$$

Then a quantum lattice (a.k.a. energy momentum spectrum or quantum web) of eigenstates of H is constructed as follows. For each eigenstate, which in the limit of zero fields, is a member of a specific n -manifold, plot $(h_2)_j$ (Eq. 84 or Eq. 86) versus q_j (Eq. 87). For weak near perpendicular fields, the result is a lattice consisting of n^2 points [50]. A quantum lattice appears in Fig. 26. A (blue online) dot is located at the point $(h_2^j/\omega_f, q_j)$ for each quantum state at $n = 20$.

The semiclassical approximation to the quantum lattice is constructed by plotting contours of the primitive classical actions $J_{+/-}$ and Q having values which are quantized according to Eqs. 76. Intersections of the contours yield semiclassical eigenvalues. We observe that almost all points in the quantum lattice lie close to such intersections.

The quantum lattices can be classified by considering the transport of lattice vectors along contours of smooth classical action variables (Section XI C) and would result in the same list of matrices as the corresponding classical spectrum (Fig. 26). It follows that

if a classical spectrum has a multivalued action variable, the corresponding quantum lattice will have a lattice defect.

XIII. THE STRUCTURE OF SPECTRA IN NEAR PERPENDICULAR FIELDS

In this section we finally explain all of the structures in the quantum spectra that were displayed without explanation in part II. All structure in those spectra follow from the study of contour plots of h_2 (Eq. 53) on $\Gamma_{N,Q}$, the (W, δ_W) surface. The following general principals should be recalled. (i) In each region of (θ, χ) , at each Q , the maximum and minimum of h_2 on $\Gamma_{N,Q}$ give the upper and lower boundaries of the spectrum in the (Q, h_2) plane. (ii) For most values of (Q, h_2) that lie within the spectral boundary, the level sets correspond to either one (classical non-degeneracy), or two (classical double degeneracy) 2-tori in $\Gamma_N \sim S^2 \times S^2$. The two fundamental loops of these tori are a Pauli orbit, and a connected level contour of h_2 on $\Gamma_{N,Q}$. (iii) The level sets which are not entirely composed of disjoint tori are marked with either dashed lines (red or magenta online) or (cyan online) diamonds. At $Q = 0$, there is no Pauli orbit at the poles of $\Gamma_{N,Q=0}$ such that any contour of h_2 which passes through a pole forms a pinched torus in Γ_N . At perpendicular fields the energies of the poles are equal and one finds a doubly-pinched torus, while in near-perpendicular fields there are two singly pinched tori with different energies. The pinched tori are marked on the spectrum with (cyan online) diamonds. (iii) Discontinuities in primitive actions follow the patterns described in Fig. 24 and are written explicitly in Eqs. 68.

Shown in Fig. 27 is a map of the parameter space (χ, θ) for weak near-perpendicular fields with $0 \leq \theta \leq \pi/2$ and $0 \leq |\chi| \lesssim \omega_f N^3 \ll 1$. The spectra are divided into regions according to the list of matrices associated with vector transport (Section XI C), and the presence of a classical double degeneracy(Section X C). As was shown in previous

$$\chi_{crit}^S(\theta) = \pm \frac{4N[\alpha + \beta]}{\omega_f \sin(2\theta)} \quad (88b)$$

Eqs. 88 divide the near-perpendicular parameter space into six regions, and when equal to zero, divide the perpendicular fields interval ($\chi = 0$) into three subintervals: $\theta < \theta_1$, $\theta_1 < \theta < \theta_2$, and $\theta > \theta_2$, with

$$\theta_1 = \cos^{-1} \left(2^{-1/4} \right) \approx 32.765^\circ \quad (89a)$$

$$\theta_2 = \cos^{-1} \left(\sqrt{\frac{\sqrt{6}}{2} - 1} \right) \approx 61.701^\circ \quad (89b)$$

There are two critical points where $\chi_{crit}^Z = \chi_{crit}^S$ in weak near-perpendicular fields at:

$$\chi_3 = \pm 3^{-1/4} \omega_f N^3 \approx \pm 0.7598 \omega_f N^3 \quad (90a)$$

$$\theta_3 = \cos^{-1} \left(\sqrt{\frac{\sqrt{3} - 1}{2}} \right) \approx 52.771^\circ \quad (90b)$$

Spectra with $\theta < \theta_1$ and $0 < |\chi| < \chi_{crit}^Z$ are classically doubly degenerate for all (Q, h_2) which are located in the interior of an inner triangular area. These spectra include the Zeeman Limit ($\theta = 0$, χ meaningless) denoted *Z.Lim*, the perpendicular Zeeman Interval ($0 < \theta < \theta_1$, $\chi = 0$) denoted $\perp Z.Int$ and the near perpendicular Zeeman Region denoted *Z.R*. On the map (Fig. 27), the boundaries of these degenerate triangular sub-areas are marked on the sample spectra plotted above *Z.R*, *Z.Lim*, and $\perp Z.Int$ because the boundaries consist of level sets which are not entirely composed of tori. The lower boundary (red dashed line online) of this region is also classically doubly degenerate, but the upper boundary (magenta dashed line online) marks the energy of an x-point separatrix on $\Gamma_{N,Q}$, and is therefore not doubly degenerate.

Spectra with $\theta > \theta_2$ and $0 < |\chi| < \chi_{crit}^S$ have a similar classically doubly degenerate inner triangular area. These Spectra include the Stark Limit ($\theta = \pi/2$, χ meaningless) denoted *S.Lim*, the perpendicular Stark Interval ($\theta_2 > \theta > \pi/2$, $\chi = 0$) denoted $\perp S.Int$

and the near perpendicular Stark Region denoted $S.R.$ Here, points on the upper boundary are classically doubly degenerate, while the lower boundary (dashed magenta online) marks the energy of an x-point separatrix on $\Gamma_{N,Q}$, and is not degenerate.

To understand how this map is derived, we consider the structure of h_2 on the $\Gamma_{N,Q}$ in the various parameter regions.

A. The structure of h_2 on $\Gamma_{N,Q}$ at $Q = 0$

In Section XI we showed how the determination of a list of matrices, used to classify a spectrum, depends on the classification of level sets as apparent rotators or apparent librators on $\Gamma_{N,Q}$ at $Q=0$. In Fig. 28 we plot a representative $\Gamma_{N,Q=0}$ for each region of the map except the regular region R (R has simple structure which is described in the figure caption). Near perpendicular regions comprise the top row, and perpendicular regions are on the bottom. For all $(\theta, \chi/\omega_f N^3)$ inside a given region as demarcated in Fig. 27, the contours of h_2 on $\Gamma_{N,Q=0}$ will have a similar structure to the representative plotted in Fig. 28 such that the same number and types of fixed points will be present. (ie: For all $(\theta, \chi/\omega_f N^3)$ inside a given region, the contours of h_2 on $\Gamma_{N,Q}$ are topologically equivalent).

Non-polar fixed points are located at the coordinates

$$(W, \delta_W) = \left(-\frac{\zeta}{2[\beta - \alpha]}, 0 \right) \quad (91a)$$

$$(W, \delta_W) = \left(-\frac{\zeta}{2[\beta + \alpha]}, \pm \frac{\pi}{2} \right) \quad (91b)$$

provided that the resulting W satisfies the requirement $W < N$. These fixed points are either x-points or o-points in accordance with Eq. 61. Additional polar o-points are located at both poles of $\Gamma_{N,Q=0}$ in regions R , $Z.R$, $S.R$, $Z.Lim$, $\perp Z.Int$, $\perp S.Int$ and $S.Lim$, and at a single pole of $\Gamma_{N,Q=0}$ in regions $I.Z$ and $I.S$.

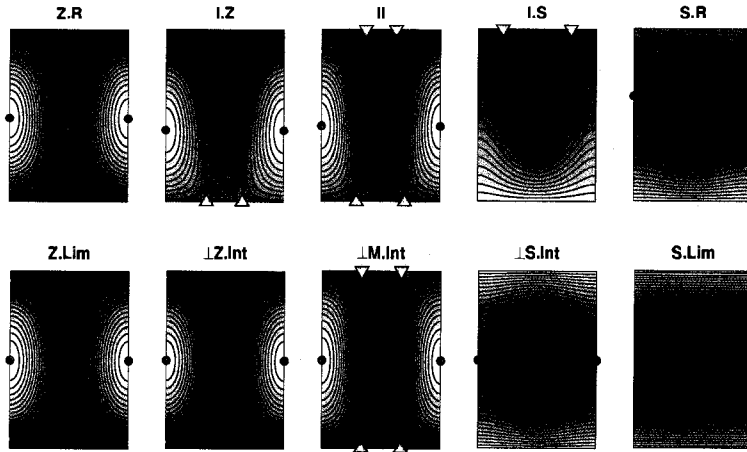


FIG. 28: (color online) The structure of $\Gamma_{N,Q}$ at $Q = 0$ for all field configurations such that $|\chi| \lesssim \omega_f n^3 \ll 1$, except the regular region R . Each $\Gamma_{N,Q=0}$ depicted above is structurally similar to every $\Gamma_{N,Q=0}$ within the same region marked on the map with the same label (Fig. 27). Each region for perpendicular fields $\chi = 0$ has a representative in the bottom row. For perpendicular fields (bottom row) all except $\perp M.Int$ have a classical double degeneracy and effective o-points at each pole, while $\perp M.Int$ has a doubly pinched torus which passes through both poles. In near-perpendicular fields (top row), there are six parameter regions, five of which have a representative in the top row. $Z.R$ and $S.R$ have effective o-points at both poles and families of doubly degenerate apparent rotators, separated from non-degenerate librators by an x-point separatrix. $I.S$ and $I.Z$ have a singly pinched torus at one pole, and an effective o-point at the other, while region II has a singly pinched torus at each pole. The region which is not represented is the completely regular region R where the structure on $\Gamma_{N,Q}$ is composed entirely of apparent rotators with an effective o-point at each pole, one maximum and one minimum.

For $\Gamma_{N,Q=0}$ in near perpendicular fields, there are two regions ($Z.R$ and $S.R$) which contain families of rotators which are classically doubly degenerate. In both cases the degenerate rotators are separated from nondegenerate librators by an x-point separatrix. In perpendicular fields all but $\perp M.Int$ have a similar double degeneracy; however note that the Stark Limit does not have a separatrix and is composed almost entirely of doubly degenerate rotators [51]. If we begin at perpendicular fields in $\perp Z.Int$ ($\perp S.Int$) and increase χ , as we pass through $Z.R$ ($S.R$) the location of the x-point migrates south (north) reaching the pole at χ_{crit}^Z (χ_{crit}^S) where we pass to $I.Z$ ($I.S$). During this passage the energy range and phase space area of the southern (northern) rotators shrinks to zero.

In near perpendicular fields are three regions (*I.Z*, *II* and *I.S*) which contain level sets associated with singly pinched tori. On $\Gamma_{N,Q}$ these level sets pass through the poles at the T-point angles $\delta_W^{T\pm}$:

$$\delta_W^{T\pm} = \frac{1}{2} \cos^{-1} \left[\frac{\beta}{\alpha} \pm \frac{\zeta}{2\alpha N} \right] \quad (92)$$

In Eq. 92, the + sign yields the angles of T-points at the north pole, while the - sign yields the angles of T-points at the south pole. Regions *I.S* and *I.Z* each have one singly pinched torus with its pinch point located at one pole of $\Gamma_{N,Q=0}$. Region *II* has two singly pinched tori, one of which has a pinch point located at the north pole of $\Gamma_{N,Q=0}$, and the other has a pinch point at the south pole. In perpendicular fields there is one interval (*⊥M.Int*) which has one doubly pinched torus, with a pinch point located at each pole of $\Gamma_{N,Q=0}$.

B. The structure of h_2 on $\Gamma_{N,Q}$ for $|Q| > 0$

In Fig. 28 we plot a representative $\Gamma_{N,Q}$ with nonzero Q for each region of the map except the regular region *R* (*R* has simple structure which is described in the figure caption). In all regions except the Stark limit, as $|Q|$ is increased from $Q = 0$, o-points which are present at a pole at $Q = 0$ become non-polar o-points and migrate toward the equator. This behavior is illustrated by comparing the $\Gamma_{N,Q=0}$ of Fig. 28 in all regions which have polar o-points with their corresponding $\Gamma_{N,Q}$ for $Q > 0$ depicted in Fig. 29. For regions with an x-point separatrix and associated classical double degeneracy (*Z.Lim*, *Z.R*, *⊥Z.Int*, *⊥S.Int*, and *S.R*), there exists a certain $|Q| = Q_{crit}$ for which a migrating o-point reaches the same location as the x-point. When this occurs, the fixed points ‘annihilate’, removing both the separatrix and the associated double degeneracy for all $|Q| > Q_{crit}$. For perpendicular fields;

$$Q_{crit} = \frac{N|\beta \pm \alpha|}{\sqrt{\beta^2 - \alpha^2}} \quad (93)$$

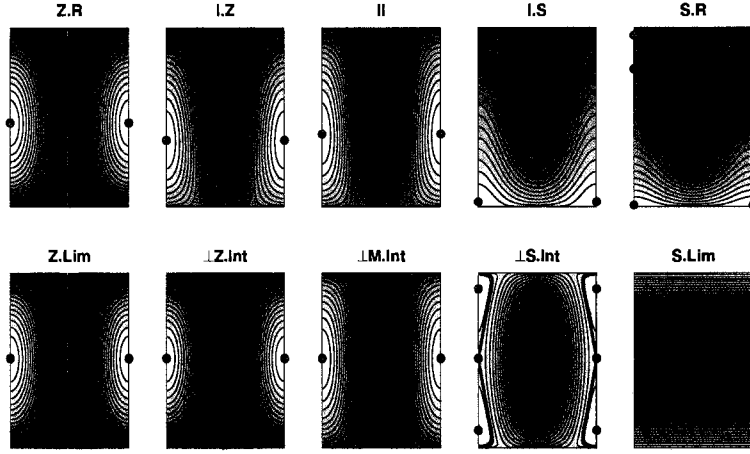


FIG. 29: (color online) The structure of $\Gamma_{N,Q}$ for $0 < Q < N$ (and $0 < Q < Q_{crit}$ in $Z.R$, $Z.Lim$, $S.R$, $\perp S.Int$) for all field configurations such that $|\chi| \lesssim \omega_f n^3 \ll 1$ except R . As $|Q|$ increases from zero, effective o-points at the poles in Fig. 28 migrate toward the equator along either $\delta_W = 0$ or $\delta_W = \pm\pi/2$ in all relevant regions (and in R) except for the Stark limit ($S.Lim$). The structure of $\Gamma_{N,Q}$ in the Stark limit is the same for all Q . If the region also contains a separatrix dividing degenerate and non-degenerate contours, then there exists a $|Q| = Q_{crit}$ such that a migrating o-point will annihilate the x-point on the separatrix, removing both the separatrix, and the degeneracy from the structure of the contours. For $0 < Q < N$, the $\Gamma_{N,Q}$ in regions $\perp M.Int$, $I.Z$, II , $I.S$, and R all share the same simple structure, determined by a single maximum energy, and a single minimum energy o-point for all $0 < Q < N$. Such structure is attained in all regions except the Stark limit for $Q > Q_{crit}$.

The appropriate sign choice in Eq. 93 is determined by the requirement $|Q| \leq N$ to be $-$ for $\theta < \theta_1$ and $+$ for $\theta > \theta_2$. As the fields are tilted from perpendicular, the value of Q_{crit} decreases, and there exist values of χ for which $Q_{crit} = 0$ where the degenerate regions collapse to a pinched level set. This occurs on the boundaries between $Z.R$ and $I.Z$ and $S.R$ and $I.S$ (online black and blue curves in Fig. 27). At these boundaries, the doubly degenerate inner triangular sub-areas of spectra collapse to a single value of (Q, h_2) marked with a (cyan online) diamond.

In all regions except the Stark limit, when $Q_{crit} < Q < N$, $\Gamma_{N,Q}$ has a two non-polar o-points, located at the maximum and minimum values of h_2 . Although they are not explicitly depicted, these contours are similar to the contours depicted in Fig. 29 $I.Z$, II , $I.S$ and $\perp M.Int$. At these large values of Q , only the locations of the o-points differ

from region to region. For perpendicular fields both o-points lie on the equator, and for large χ they remain very near to the poles.

As an example, consider how a spectrum in the Stark Region ($S.R$) varies with Q . A sample spectrum is plotted over the region labeled $S.R$ on the map (Fig. 27) or one may be viewed in Fig. 11 of Ref. [14]. We see that the small classically doubly degenerate triangular region exists only for a certain range of Q , and at $Q = 0$ the degeneracy occupies its maximal energy range. Q_{crit} is the value of $|Q|$ where the upper boundary, marking the energy of the maximal o-point, and lower boundary marking the energy of the x-point separatrix meet. As was explained this is the value of Q where the o-point and the x-point annihilate, removing the degeneracy for $|Q| > Q_{crit}$. The corresponding pictures on $\Gamma_{N,Q}$ are found in Fig. 28($S.R$) for $Q = 0$, Fig. 29($S.R$) for $|Q| < Q_{crit}$ and for $|Q| > Q_{crit}$, $\Gamma_{N,Q}$ would look most similar to Fig. 29 ($I.S$)

C. The map revisited

Having considered all the different topological structures of the fully reduced Hamiltonian found in near-perpendicular electric and magnetic fields, we can now look back at the curves dividing the regions of map and better understand how they are related to topological changes in h_2 . (i) On χ^Z for $\theta < \theta_1$, where in Fig. 27, $Z.R$ changes to $I.Z$, the x-point separatrix on $\Gamma_{N,Q}$ at $Q = 0$ (Fig. 28, $Z.R$) collides with the southern polar o-point, creating one singly pinched torus (Fig. 28, $I.Z$). In this process, the rotators near the south pole, which had overlapped in energy with those near the north pole, disappear. As a result the triangular classically doubly degenerate region of the spectrum shown in Fig. 27, $Z.R$ collapses into a single monodromy point (cyan diamond in Fig. 27, $I.Z$). (ii) On χ^S for $\theta > \theta_2$, when we go from $S.R$ to $I.S$, a similar process occurs on $\Gamma_{N,Q}$ at $Q = 0$ near the north pole. (iii) On χ^Z for $\theta > \theta_1$, where in Fig. 27 $I.Z$ changes to II and R changes to $I.S$, the minimum energy polar o-point on

$\Gamma_{N,Q}$ at $Q = 0$ bifurcates into a non-polar minimum o-point and a singly pinched torus. This is depicted in Fig. 28 where the minimum energy o-point at the north pole in $I.Z$ bifurcates as we pass into region II into the singly pinched torus at the north pole, and minimum o-point which has migrated away from the pole. (iv) On χ^S for $\theta < \theta_2$, where $I.S$ changes to II and R changes to $I.Z$, a similar process happens to the maximum o-point on $\Gamma_{N,Q}$ at $Q = 0$. This is depicted in Fig. 28 where the maximum energy o-point at the south pole in $I.S$ bifurcates in II into the singly pinched torus at the south pole, and maximum o-point which has migrated away from the pole. These considerations give a complete explanation of the spectra that were displayed in Ref. [14].

XIV. QUANTUM CORRELATION DIAGRAMS

As the field parameters are varied across boundaries of the map (Fig.27) the topological structure of the contours of $h_2(W, \delta_W)$ can change abruptly. However the quantum energy eigenvalues are always continuous and even differentiable functions of χ and θ . In this section we examine how the eigenvalues evolve from region to region on the map.

A. Degeneracy breaking: From perpendicular to near-perpendicular fields

Near the Zeeman and Stark limits, the quantum energy spectra have a structure in the second order splitting associated with a double degeneracy. For perpendicular fields, the degeneracy in these regions is (very nearly) exact, and when the fields are tilted into nearly perpendicular configurations, the degeneracy is broken. As χ is varied, the formerly degenerate pair are displaced to higher and lower energies. If multiple adjacent degenerate pairs exist for $\chi = 0$, then as χ is varied such states can exhibit anti-crossings [52]. An example of such behavior appears in Fig. 30, where the solid curves depict the energies of fifteen eigenstates from the $q = 0$ manifold near the Stark Limit as χ is increased from zero ($\perp S.Int \rightarrow S.R$). The energies of the twelve states associated with the anti-crossings have a markedly different behavior from the three lowest energy states which are nondegenerate at $\chi = 0$. Detail in Fig. 30b illustrates that anti-crossings between members of the twelve high energy states are very narrow for $h_2/\omega_f > -0.063$ and widen near the three low energy states as is found near $h_2/\omega_f = -0.0637$, $\chi/\omega_f n^3 = 0.35$. Near $h_2/\omega_f = -0.064$, $\chi/\omega_f n^3 = 0.17$ the lowest energy state above the (magenta online) dashed line behaves as if reflected from the three nondegenerate states below.

The nature of the states in such degenerate portions of the spectrum can be understood in terms of the classical degeneracy found on $\Gamma_{N,Q}$. In a primitive semiclassical approximation, a quantum state is associated with each contour of h_2 with J_+ or J_-

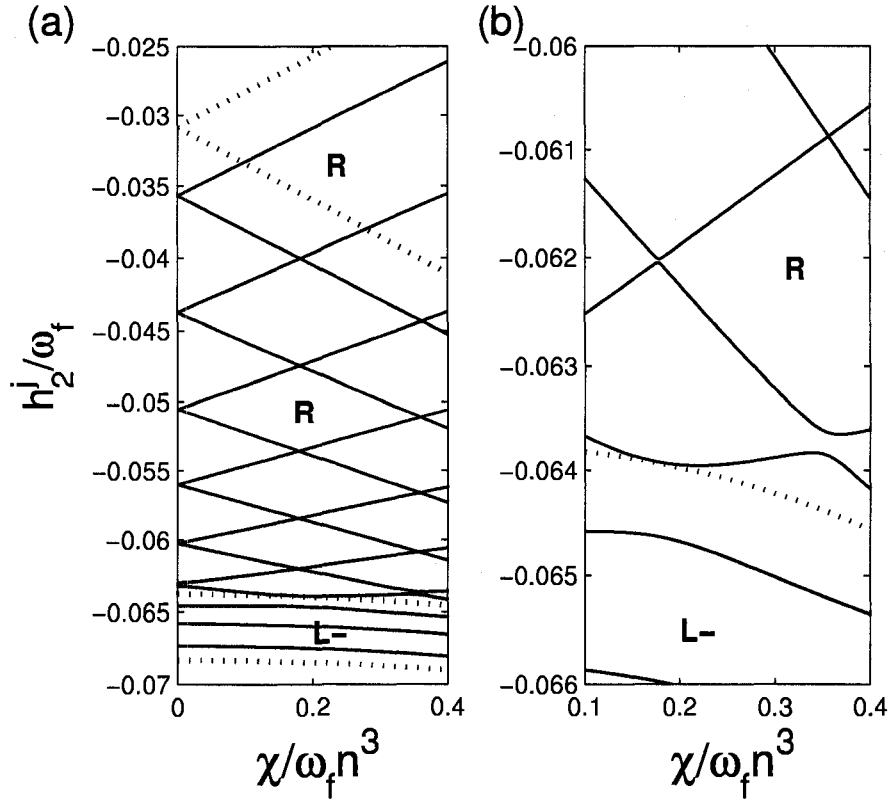


FIG. 30: (color online) Correlation diagram from perpendicular to near-perpendicular fields. The energy eigenvalues of the fifteen eigenstates at $n = 15$, $q = 0$ for $\theta = 80^\circ$, $\omega_f n^3 = 0.01$ are plotted as a function of $\chi / \omega_f n^3$ using 111 evenly spaced data points. The quantum basis included n manifolds 12 – 18. Eigenstates which are (very nearly) degenerate at $\chi = 0$ are split and anti-cross as the fields are tilted from perpendicular. (a) The four dashed lines are the classical energies of (from top to bottom): an effective o-point at the south pole, an effective o-point at the north pole, an x-point separatrix (magenta online), and a non-polar o-point having the minimum energy on $\Gamma_{N,Q} = \Gamma_{15,0}$. All energies between that of the north pole and of the x-point separatrix are classically doubly degenerate. (b) Detail near the energy of the x-separatrix reveals that anti-crossings between the states which occur well inside the classically degenerate region are very narrow, but become larger near the x-point separatrix.

quantized as in Eq. 76c. For perpendicular fields h_2 (Eq. 53) is symmetric about the equator $W = 0$. Then, for some \mathbf{F} and \mathbf{B} there are two disjoint classical contours, $c^{(N)}$ localized in the north ($W > 0$) and $c^{(S)}$ localized in the south ($W < 0$) which have the same value of h_2 . For every northern contour $c^{(N)}$ having an appropriately quantized primitive action, there is a corresponding southern contour $c^{(S)}$ with the same action $J_{+/-}^{(N)} = J_{+/-}^{(S)}$, forming a degenerate pair of states. When the fields are tilted from per-

pendicular the W symmetry is broken but there may still be regions of classical double degeneracy. However, in this case if a contour in the north has a particular value of $J_{+/-}$, the contour in the south having the same energy does not necessarily have the same value of $J_{+/-}$. Thus in general the degeneracy in the quantum states is removed as χ is varied. Continuing to tilt the fields may produce nonzero values of χ for which the difference in the primitive actions $J_{+/-}^{(N)} - J_{+/-}^{(S)}$ is an integer. In this case both contours are associated with a quantum state having the same energy, producing again a double degeneracy. Since the primitive semiclassical approximation does not account for tunneling, northern states are decoupled from southern states, and the locations where the semiclassical levels cross indicates the locations of the quantum anti-crossings.

Looking back to Fig. 30, we identify the four dashed lines from top to bottom with the energies of the following structures in Fig. 28 $\perp S.Int$ and $S.R$: the o-point at the south pole, the o-point at the north pole, the x-point separatrix (magenta online), and the non-polar o-point minimum. States with energies below that of the separatrix correspond to apparent librators while states above correspond to apparent rotators. From the semiclassical model (or simply from correspondence with $\partial h/\partial\chi = -2\sin(2\theta)W$ when not near an anti-crossing), we identify the northern(southern) rotators with states having energies which are decreasing(increasing) functions of χ . The anti-crossings in the classically degenerate region which widen near the x-separatrix are expected from tunneling between the northern and southern rotators, which would be strongest near the separatrix. As was discussed in Section XIII B, as χ increases the energy range and phase space area of the northern rotators is diminished, but the energy range and phase space area of the southern rotators is increased. The semiclassical approximation predicts that northern rotators should disappear while new southern rotators should appear near the energy of the x-separatrix. The analogous quantum process is present in Fig. 30b near $\hbar_2/\omega_f = -0.0642$, $\chi/\omega_f n^3 = 0.19$ where the lowest energy northern rotator changes character from a decreasing function of χ , to an increasing function of

χ near the energy of the separatrix.

Consider quantum expectation values of the operator $\omega_f \hat{W}$ (Eq. 81) corresponding to the classical coordinate W . The scaled expectation value is:

$$w_j = \frac{1}{\omega_f(\bar{n})} \langle \Psi_j | \omega_f \hat{W} | \Psi_j \rangle \quad (94)$$

For perpendicular fields, the calculated degenerate quantum states are linear combinations of the ‘northern’ and ‘southern’ states corresponding to the odd and even parity about $W = 0$, and the expectation value (Eq. 94) vanishes. In between each anti-crossing, the expectation (Eq. 94) displays the northern or southern character of each quantum state. The quantum states are strongly coupled again at each anti-crossing where states adjacent in energy exchange their northern and southern character. The expectations of w_j (Eq. 94) for both states in an anti-crossing are exchanged within an interval of $\chi/\omega_f n^3$ which is inversely proportional to the energy width of the anti-crossing. These phenomena are illustrated in Fig. 31(a) where w_j is plotted for the same states which appear in the energy correlation diagram in Fig. 30.

To visualize the W character of quantum states in a spectrum, one may augment the quantum lattice such that a dot for each quantum state $|\Psi_j\rangle$ is plotted at the values (q_j, h_2^j, w_j) . In Fig. 31b we plot an augmented lattice for a spectrum with a classical double degeneracy but no quantum degeneracy, and away from any anti-crossing. The lattice points are spaced regularly, and in the limit $n \rightarrow \infty$ at fixed $\omega_f n^3$ can be considered to define a surface in three dimensions. The projection of the augmented lattice into the (Q, h_2) plane recovers the usual quantum lattices, but suggests that two families of quantum states exist within the triangular classically degenerate regions, and that each family requires a separate lattice coordinate system. Furthermore one such coordinate system is connected continuously with the states in the rest of the spectrum, while the other is confined within the triangular region. This situation is precisely what results when constructing such a coordinate system from the classical actions.

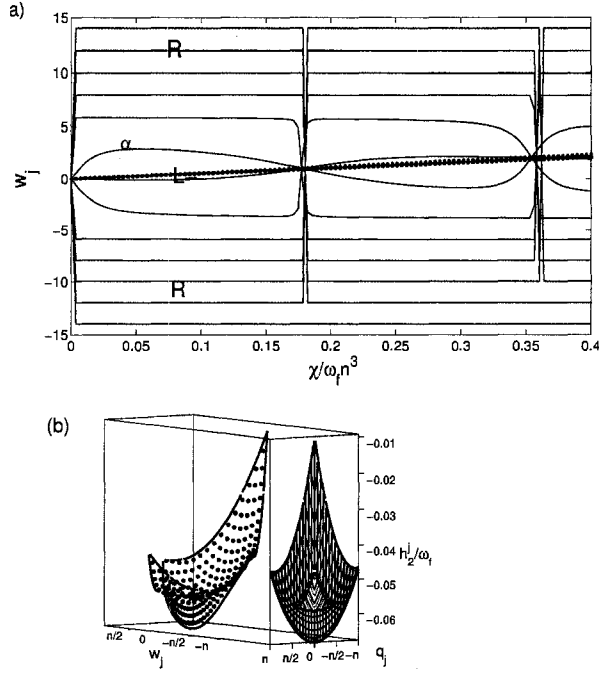


FIG. 31: (color online) (a) The expectation values $w_j = \langle \psi_j | \omega_f \hat{W} | \psi_j \rangle / \omega_f$ for the fifteen energy eigenstates at $n = 15$, $q = 0$ for $\theta = 80^\circ$, $\omega_f n^3 = 0.01$ are plotted as a function of $\chi/\omega_f n^3$ with 111 evenly spaced data points (compare with Fig. 30). The quantum basis included n manifolds 12–18. (a) At $\chi = 0$ doubly degenerate eigenstates are coupled by tunneling into symmetric and antisymmetric combinations of ‘northern’ and ‘southern’ states such that $w_j = 0$. As the fields are tilted from perpendicular, the w_j expectations assume values which are in agreement with the localization of the semiclassical states on $\Gamma_{N,Q}$. For $\chi/\omega_f N^3 < 0.1$ there are expectation values associated with six northern and six southern rotators, and three librators which very closely follow the classical expectations of W for the minimum α -point plotted in (blue online) dots and the x -point plotted with (red online) x ’s. At energy anti-crossings, the quantum states (adiabatically) exchange their W character, with narrow anti-crossings between rotators in the far north and far south occurring within small intervals of $\chi/\omega_f N^3$, and wider anti-crossings occurring between rotators near the W locations of the x -point separatrix. The state labeled α is a northern rotator which changes character to a southern rotator at $\chi/\omega_f N^3 \approx 0.17$ where it crosses the W of the x -point, mildly affecting the libration which visibly oscillates about the x point. The very slow W exchange between the southernmost northern rotator, and the northernmost southern rotator at $\chi/\omega_f N^3 \approx 0.36$ is identified with the wide energy anti-crossing in Fig. 30(b) at $(h_2/\omega_f, \chi/\omega_f N^3) \approx (-0.0637, 0.35)$. (b) An Augmented Quantum Lattice is constructed by plotting a dot for each quantum eigenstate $|\psi_j\rangle$ at the coordinates (q_j, h_2^j, w_j) . Classical boundaries are plotted at their classical expectation values of W . The augmented lattice aids in clarifying the nature of the triangular classically degenerate regions which occur in the two dimensional quantum lattices, and suggests that such quantum lattice vector transport can be well defined when passing through the boundaries of the triangle which are not associated with the classical x -point separatrix.

B. From the Zeeman Limit to the Stark Limit in near perpendicular fields

We now consider the correlation between the energy eigenstates in the Zeeman limit, and the energy eigenstates in the Stark limit as we continuously vary the field parameters from $\mathbf{F} = 0$ to $\mathbf{B} = 0$ at a constant value of χ in the near perpendicular region.

In Fig. 32 we trace the evolution of the fifteen eigenstates associated with the $n = 15$ and $q = 0$ manifolds as θ is varied from 0° to 90° holding both $\omega_f = 0.01/n^3$ and $\chi = 0.2\omega_f n^3$ fixed. Each of the fifteen states corresponds to a contour on $\Gamma_{N,Q}$ at $Q = 0$ (Fig. 28) as the structure of the contours changes continuously from *Z.Lim* to *S.Lim*. As we move from left to right in Fig. 32, the corresponding series of diagrams in Fig. 28 are from *Z.Lim* to *Z.R*, across the upper row of pictures to *S.R* and then to *S.Lim*. Energies of classical level sets which have at least one component which is not a 2-torus are marked with dashed lines or diamonds.

(*Z.Lim*) At the Zeeman Limit $\theta = 0^\circ$, the four states with least energy are associated with pairs of degenerate apparent rotators, separated from eleven apparent librators at high energies by an x-point separatrix, with energy marked by a dashed line (magenta online).

(*Z.R*) When θ is increased holding $\chi/\omega_f n^3 = 0.2$ fixed, the degeneracy in the rotators is broken. The northern rotators move to lower energies while the southern rotators move to higher energies, resulting in avoided crossings which are narrow except when they occur at energies close to the separatrix. The lowest two dashed red lines are the energies of the polar effective o-points. The energy of the southern pole climbs to higher energies and meets the descending x-separatrix at $\theta \approx 29^\circ$ removing the classical double degeneracy. As we would expect from the semiclassical model, the northern rotators pass uneventfully through the energy of the south pole, while southern rotators experience interactions as they cross the x-separatrix to become librators.

(*I.Z*) Upon passing $\theta \approx 29^\circ$, the x-point separatrix and the south polar o-point

collapse into a singly pinched torus, the energy of which is marked with a string of (cyan online) diamonds. Distinction between the energy evolution of apparent librators above the diamonds, and the apparent rotators below the diamonds is no longer present. This is expected because this region is devoid of degeneracy, and we do not expect groups of states here to have vastly different sharp W localizations.

(II) At $\theta \approx 39^\circ$, the o-point at the north pole splits into a non-polar o-point and a singly pinched torus. States which have energies between the energies of the pinched tori are apparent rotators, while those above and below are apparent librators. However there is no real distinction between these, and in Fig. 32 the quantum energies pass with little disturbance through the energy of a pinched torus as they change apparent character between rotators and librators. This passage is in contrast with changes of character which occur as energies cross an x-point separatrix.

(I.S) At $\theta \approx 59^\circ$, the maximal energy o-point supporting the Zeeman librators combines with the pinched torus at the south pole into an o-point with maximal energy. The singly pinched torus at the north pole divides the southern rotators from the low energy Stark librators.

(S.R) At $\theta \approx 64^\circ$ the pinched torus at the north pole splits into an x-point and an effective polar o-point. As θ continues to increase, the north polar o-point climbs in energy to meet that of the south pole, while the energy of the x-point decreases to join that of the minimal o-point. The x-point separates the low energy Stark librators from the high energy Stark rotators. At all energies between that of the x-point and the north pole, there is a classical double degeneracy, and the associated narrow anti-crossings behavior.

(S.Lim) When the Stark limit is reached at $\theta = 90^\circ$, every state except that with the lowest energy is paired in a double degeneracy associated with a northern-southern rotator pair.

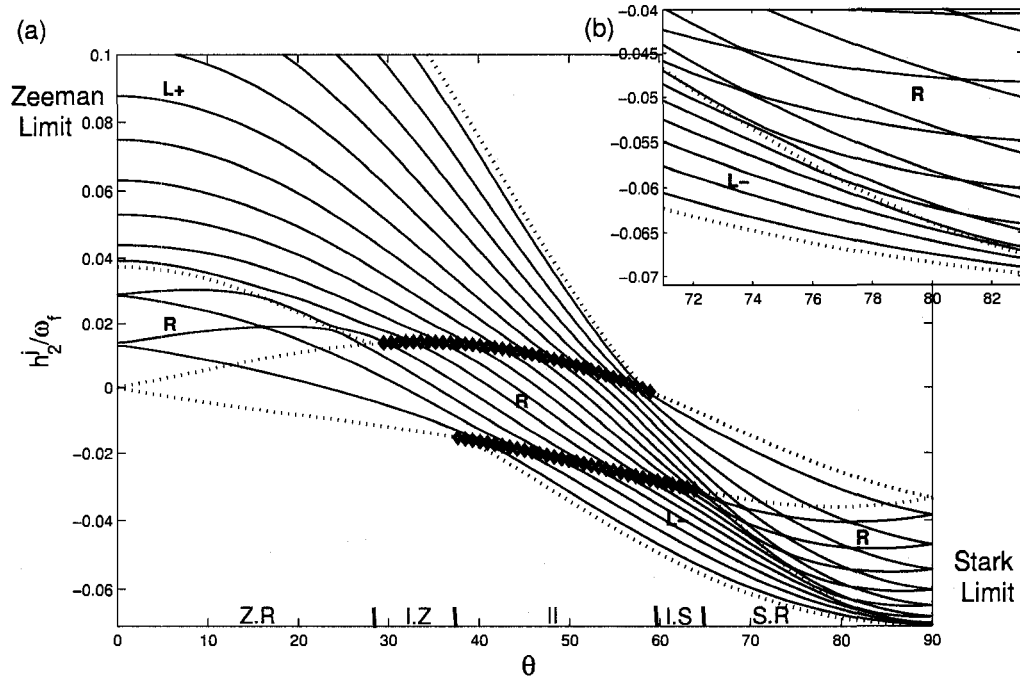


FIG. 32: (color online) Correlation diagram from the Zeeman to the Stark limit in near-perpendicular fields. The energy eigenvalues of the fifteen eigenstates at $n = 15$, $q = 0$, $\omega_f n^3 = 0.01$ are plotted as a function of θ in near-perpendicular fields $\chi/\omega_f n^3 = 0.2$. The quantum basis included n manifolds 12 – 18. The evolution of the energies of the states is traced with solid (blue online) lines from the Zeeman Limit (*Z.Lim*) $\theta = 0^\circ$ to $\theta = 90^\circ$ at the Stark Limit (*S.Lim*), passing into the regions (*Z.R.*, *I.Z.*, *II*, *I.S.* and *S.R.*) at approximately $\theta = (0^\circ, 29^\circ, 38^\circ, 59^\circ, 64^\circ$ and $90^\circ)$ en route. Energies for which at least one component of the classical level set is not a 2-torus are marked with dashed curves or curves of diamonds. The upper/lower curve of (cyan online) diamonds represents the energy of the singly pinched torus at the south/north pole, and joins smoothly to (red online) dashed curves which mark the energy of a polar effective o-point. The (magenta online) dashed curves joining the curve of diamonds mark the energy of an x-point separatrix, and all energies between an x-point energy and the nearest effective o-point energy are classically doubly degenerate. For $\theta \lesssim 59^\circ$ ($\theta \gtrsim 29^\circ$), the dashed curve with maximum(minimum) energy is that of the Zeeman(Stark) liblator o-point. Regions of states separated by the energies of classical structures are marked with either an *R*, an *L+* or an *L-*, indicating that they are associated with apparent rotators, apparent librators about a maximal energy, and apparent librators about a minimal energy respectively. In the upper right hand corner of the figure, detail near the Stark limit is enlarged. States associated with apparent rotators in classically doubly degenerate regions exhibit narrow anti-crossings, which widen near the energy of the x-point separatrix. As the energy range of degeneracy in the Zeeman(Stark) Region is diminished with increasing(decreasing) θ , states associated with southern(northern) rotators pass through the energy of the x-separatrix and change character to librators, while northern/southern rotators continue unaffected into nondegenerate regions below/above the energy of the effective o-point at the south/north pole.

XV. CONCLUSION:

We have used classical perturbation theory to derive an integrable system which describes the dynamics of the Hydrogen atom in weak near-perpendicular electric and magnetic fields. Semiclassical quantization of the resulting integrable system is in good agreement with quantum calculations, and provides interpretation of the structures in the second order quantum spectrum that were discussed in part II.

APPENDIX A: KEPLER AVERAGING

1. Average in the orbital frame

To average functions of phase space over an unperturbed Kepler orbit; use the identity $M = Ne$ and the eccentric anomaly Ψ , defined by Kepler's equation $\phi_N = \Psi - \frac{M}{N} \sin \Psi$, to rewrite Eq. 24d as: [54]

$$\langle g \rangle_{\phi_N} = \frac{1}{2\pi} \int_0^{2\pi} g \left[1 - \frac{M}{N} \cos \Psi \right] d\Psi \quad (\text{A1})$$

The functions to be averaged depend on the position vector and tensor components (x_j and $x_i x_j$) in the space fixed frame with basis vectors $\{\hat{\mathbf{x}}, \hat{\mathbf{y}}, \hat{\mathbf{z}}\}$. These components can be expressed in terms of the orbital reference frame components (x'_j and $x'_i x'_j$) with basis vectors $\{\hat{\mathbf{x}}', \hat{\mathbf{y}}', \hat{\mathbf{z}}'\} = \left\{ \frac{\mathbf{M}}{M}, \frac{\mathbf{L} \times \mathbf{M}}{LM}, \frac{\mathbf{L}}{L} \right\}$ using the orthonormal direction cosine matrix transformation.

$$R_{i,j} = \hat{\mathbf{x}}'_i \cdot \hat{\mathbf{x}}_j \quad (\text{A2})$$

Since the orbit is fixed, the Kepler averages (Eq. A1) of x_j and $x_i x_j$ reduce to averages in the orbital frame.

$$\langle x_j \rangle_{\phi_N} = R_{j,k}^T \langle x'_k \rangle_{\phi_N} \quad (\text{A3a})$$

$$\langle x_i x_j \rangle_{\phi_N} = R_{i,k}^T \langle x'_k x'_p \rangle_{\phi_N} R_{p,j} \quad (\text{A3b})$$

The averages in the orbital frame may be computed by expressing the x'_j and $x'_i x'_j$ components in terms of the eccentric anomaly using: [55]

$$\mathbf{r}' = (x', y', z') = \left(N^2 \left[\cos \Psi - \frac{M}{N} \right], NL \sin \Psi, 0 \right) \quad (\text{A4})$$

2. Computing Eq. 24 of Section VII A

To compute Eq. 24b, average H_1 as it appears in Eq. 20 using $\langle \mathbf{L} \rangle_{\phi_N} = \mathbf{L}$, and Eq. A3a with $R_{1,1}^T = \mathbf{M}_x/M$ and the average of Eq. A4;

$$\langle \mathbf{r}' \rangle_{\phi_N} = \left(-\frac{3}{2}NM, 0, 0 \right) \quad (\text{A5})$$

The result is $\langle H_1 \rangle_{\phi_N}$ in Eq. 30.

The average of H_2 as it appears in Eq. 20 is

$$\langle H_2 \rangle_{\phi_N} = \frac{B^2}{8} [\langle xx \rangle_{\phi_N} + \langle yy \rangle_{\phi_N}] + F_z \langle z \rangle_{\phi_N} \quad (\text{A6})$$

and is computed by noting that the only nonzero Kepler averaged $x'_i x'_j$ are (using $M^2 + L^2 = N^2$):

$$\langle x'x' \rangle_{\phi_N} = \frac{N^2}{2} (N^2 + 4M^2) \quad (\text{A7a})$$

$$\langle y'y' \rangle_{\phi_N} = \frac{N^2}{2} L^2 \quad (\text{A7b})$$

After expressing the averages in the orbital frame via Eqs. A3 and Eqs. A7 one obtains:

$$\langle H_2 \rangle_{\phi_N} = \frac{B^2}{8} \langle x'x' \rangle_{\phi_N} [R_{1,1}^{T^2} + R_{2,1}^{T^2}] + \frac{B^2}{8} \langle y'y' \rangle_{\phi_N} [R_{1,2}^{T^2} + R_{2,2}^{T^2}] + F_z R_{3,1}^T \langle x' \rangle_{\phi_N} \quad (\text{A8})$$

The F_z term is $-\frac{3}{2}NF_zM_z$, while the term proportional to B^2 may be re-expressed by substitution using $\sum_j (R_{i,j}^T)^2 = \sum_i (R_{i,j}^T)^2 = 1$, which follows from the orthonormality of R . One obtains:

$$\langle H_2 \rangle_{\phi_N} = -\frac{3}{2}NF_zM_z + \frac{B^2}{8} \langle x'x' \rangle_{\phi_N} + \frac{B^2}{8} [(\langle y'y' \rangle_{\phi_N} - \langle x'x' \rangle_{\phi_N}) R_{3,1}^{T^2} + \langle y'y' \rangle_{\phi_N} R_{3,3}^{T^2}] \quad (\text{A9})$$

After substitution of Eqs. A7 and $R_{3,1}^T = \mathbf{M}_z/M$ and $R_{3,3}^T = \mathbf{L}_z/L$, the result is $\langle H_2 \rangle_{\phi_N}$ in Eq. 30.

a. *The explicit generating function f_1*

The terms in H'_2 require the first order generating function f_1 (f_2 is not needed because $\langle \partial f_2 / \partial \phi_N \rangle_{\phi_N} = 0$ by the imposed periodicity of f). To obtain an explicit functional form for f_1 , we first note that Eqs. 23b and 24b together imply the following partial differential equation in the Delaunay coordinates.

$$\frac{\partial f_1}{\partial \phi_N} = N^3 [\langle H_1 \rangle_{\phi_N} - H_1] = N^3 F_x [\langle x \rangle_{\phi_N} - x] \quad (\text{A10})$$

The last equality is obtained from the difference of $\langle H_1 \rangle_{\phi_N}$ in Eq. 30 and H_1 in Eq. 20 and is independent of B because $\langle L_z \rangle_{\phi_N} = L_z$. We obtain an explicit form for f_1 by the indefinite integration of Eq. A10 over ϕ_N , holding the rest of the Delaunay Variables fixed. Again utilizing the eccentric anomaly Ψ one obtains:

$$f_1 = -N^5 F_x R_{1,1}^T \left[\left(1 - \frac{M^2}{2N^2} \right) \sin \Psi - \frac{M}{2N} \sin \Psi \cos \Psi \right] - N^4 L F_x R_{1,2}^T \left[1 - \frac{M}{2N} - \cos \Psi + \frac{M}{2N} \cos^2 \Psi \right] + C \quad (\text{A11})$$

which is of the form:

$$f_1 = \tilde{f}_1 + C \quad (\text{A12})$$

Where the undetermined integration constant C is only constrained by the requirement that it be independent of ϕ_N . We are free to choose:

$$C = -\langle \tilde{f}_1 \rangle_{\phi_N} = N^4 L F_x R_{1,2}^T \left(1 + \frac{M}{4N} \right) \quad (\text{A13})$$

such that:

$$\langle f_1 \rangle_{\phi_N} = 0 \quad (\text{A14})$$

b. *The second order Hamiltonian is independent of $F_x B$*

Substituting Eq. A12, and H_1 as it appears in Eq. 20 into Eq. 23d, produces an expression for H'_2 that has an average of the form:

$$\begin{aligned} \langle H'_2 \rangle_{\phi_N} = & \\ & F_x \left[\left\langle \frac{\partial x}{\partial N} \frac{\partial \tilde{f}_1}{\partial \phi_N} \right\rangle_{\phi_N} + \left\langle \frac{\partial x}{\partial L} \frac{\partial \tilde{f}_1}{\partial \phi_p} \right\rangle_{\phi_N} + \left\langle \frac{\partial x}{\partial L_z} \frac{\partial \tilde{f}_1}{\partial \Omega} \right\rangle_{\phi_N} \right] \\ & - F_x \left[\frac{\partial \langle x \rangle_{\phi_N}}{\partial L} \frac{\partial \langle \tilde{f}_1 \rangle_{\phi_N}}{\partial \phi_p} + \frac{\partial \langle x \rangle_{\phi_N}}{\partial L_z} \frac{\partial \langle \tilde{f}_1 \rangle_{\phi_N}}{\partial \Omega} \right] - \frac{3}{2N^4} \left\langle \left(\frac{\partial \tilde{f}_1}{\partial \phi_N} \right)^2 \right\rangle_{\phi_N} \end{aligned} \quad (\text{A15})$$

Since \tilde{f}_1 is proportional to F_x , $\langle H'_2 \rangle_{\phi_N}$ is composed entirely of terms proportional to F_x^2 . Thus, the second order dynamics of Hydrogen in near perpendicular fields has been rendered independent of the mixed fields term $F_x B$ by our choice of integration constant C in Eq. A13.

c. *Computing $\langle H'_2 \rangle_{\phi_N}$*

The evaluation of Eq. A15 is lengthy and tedious, we outline the essential steps here, and publish a detailed account in supplementary outlets [53].

After eliminating M (via $N^2 = L^2 + M^2$), x and \tilde{f}_1 are functions only of N , L and the functions $R_{1,1}^T$, $R_{1,2}^T$ and Ψ . Their averages, $\langle x \rangle$ and $\langle \tilde{f}_1 \rangle$ are independent of Ψ and are considerably reduced. The required partial derivatives of these four functions in the Delaunay coordinates are straightforward to compute; using implicit differentiation of Kepler's equation for calculating derivatives of Ψ , and maintaining the derivatives of the $R_{i,j}^T$ as formal functions. After substituting these partial derivatives into Eq. A15, and performing the required averages, one obtains:

$$\begin{aligned}
& \langle H'_2 \rangle_{\phi_N} = \\
& \frac{F_x^2 N^4}{16} L (5N^2 + 3L^2) \left[\frac{\partial R_{1,1}^T}{\partial L} \frac{\partial R_{1,2}^T}{\partial \phi_p} - \frac{\partial R_{1,2}^T}{\partial L} \frac{\partial R_{1,1}^T}{\partial \phi_p} + \frac{\partial R_{1,1}^T}{\partial L_z} \frac{\partial R_{1,2}^T}{\partial \Omega} - \frac{\partial R_{1,2}^T}{\partial L_z} \frac{\partial R_{1,1}^T}{\partial \Omega} \right] \\
& - \frac{F_x^2 N^4}{16} \left[(5N^2 + 4L^2) R_{1,2}^T \frac{\partial R_{1,1}^T}{\partial \phi_p} - 5L^2 R_{1,1}^T \frac{\partial R_{1,2}^T}{\partial \phi_p} \right] \\
& - \frac{F_x^2 N^4}{16} \left[(14N^2 + 10L^2) R_{1,1}^{T^2} + 20L^2 R_{1,2}^{T^2} \right]
\end{aligned} \tag{A16}$$

The final simplifications come from the properties of R^T . Since R^T is independent of ϕ_N , the expression in the brackets of the first term can be interpreted as the Poisson Bracket: $\{R_{1,1}^T, R_{1,2}^T\}$ in the Delaunay variables. It is straightforward but tedious to verify the following identity: (We find it is quickest to use the Euler matrix form of R^T [56], eliminating the orbital inclination i with the equation $i = \cos^{-1}(L_z/L)$).

$$\{R_{1,1}^T, R_{1,2}^T\} = -\frac{R_{1,3}^{T^2}}{L} \tag{A17a}$$

By the same suggested method, it is trivial to prove two more identities.

$$\frac{\partial R_{1,1}^T}{\partial \phi_p} = R_{1,2}^T \tag{A17b}$$

$$\frac{\partial R_{1,2}^T}{\partial \phi_p} = -R_{1,1}^T \tag{A17c}$$

Substituting these identities into Eq. A16 one obtains:

$$\begin{aligned}
& \langle H'_2 \rangle_{\phi_N} = -\frac{F_x^2 N^4}{16} (5N^2 + 3L^2) R_{1,3}^{T^2} \\
& - \frac{F_x^2 N^4}{16} \left[(5N^2 + 24L^2) R_{1,2}^{T^2} + (14N^2 + 15L^2) R_{1,1}^{T^2} \right]
\end{aligned} \tag{A18}$$

Eliminating $R_{1,2}^{T^2}$ with the column orthonormality of R^T , and cosmetically eliminating L^2 in favor of M^2 one obtains:

$$\langle H'_2 \rangle_{\phi_N} = -\frac{F_x^2 N^4}{16} \left[29N^2 - 24M^2 - 21L^2 R_{1,3}^{T^2} + 9M^2 R_{1,1}^{T^2} \right] \tag{A19}$$

Finally, with $R_{1,1}^T = M_x/M$ and $R_{1,3}^T = L_x/L$, we have arrived at $\langle H_2' \rangle_{\phi_N}$ as it appears in Eq. 30.

APPENDIX B: THE TOPOLOGY OF $\Gamma_{N,Q}$

The space of all Kepler orbits at fixed N is $\Gamma_N \sim S^2 \times S^2$. Each point $K \in \Gamma_N$ is an equivalence class of points in the full six dimensional Cartesian phase space such that all points (x, y, z, p_x, p_y, p_z) contained in a particular Kepler orbit having the vectors \mathbf{J}_1 and \mathbf{J}_2 are equivalent [57]. Define a natural distance between two Kepler orbits:

$$d_K(K, \tilde{K}) = |\mathbf{J}_1 - \tilde{\mathbf{J}}_1| + |\mathbf{J}_2 - \tilde{\mathbf{J}}_2| \quad (\text{B1})$$

A Pauli Orbit $P \in \Gamma_N$ is a subset of the space of all Kepler orbits at a fixed N defined by:

$$P \equiv \left\{ K \in \Gamma_N \mid Q = \mu_1 + \mu_2, W = \mu_1 - \mu_2, \& \text{ if } |W| < N - |Q| \text{ then } \delta_W = \frac{1}{2}(\psi_1 - \psi_2) \right\} \quad (\text{B2})$$

In Γ_N , each P is either a one dimensional closed curve, or a point (if $Q = \pm N$ or $Q = 0$ and $W = \pm(N - |Q|)$). If P is not a point, then each $K \in P \subset \Gamma_N$ is labeled by a value of the coordinate σ_Q .

Let the space of all Pauli orbits at a fixed Q be denoted $\Gamma_{N,Q} \sim (W, \delta_W)$ surface. Each point $P \in \Gamma_{N,Q}$ is an equivalence class of points $K \in \Gamma_N$ such that all points K which are contained in the same P defined in Eq. B2 are equivalent. This structure, motivated by the perturbative description of the motion, determines the effective topology on the (W, δ_W) surface.

Proposition: $\Gamma_{N,Q}$, the two-dimensional fully reduced phase space at fixed N and Q (a.k.a the (W, δ_W) surface) is homeomorphic to a sphere.

The homeomorphism is given in spherical polar coordinates (r, θ, ϕ) by;

$$N - |Q| = r \quad (\text{B3a})$$

$$W = r \cos \theta \quad (\text{B3b})$$

$$\delta_W = \frac{\phi}{2} \quad (\text{B3c})$$

To establish that neighborhoods of (W, δ_W) near $W = \pm(N - |Q|)$ are connected like a sphere, we show that:

Given any P and \tilde{P} such that: (i) $Q = \tilde{Q}$ with $|Q| \leq N$, (ii) $W = \tilde{W}$ with $|W| < N - |Q|$, but (iii) $\delta_W \neq \tilde{\delta}_W$. Then: $\forall K \in P \exists \tilde{K} \in \tilde{P}$ such that:

$$\lim_{W \rightarrow \pm(N - |Q|)} d_K(K, \tilde{K}) = 0 \quad (\text{B4})$$

To show this, obtain expressions for $J_{1,x'_i}(Q, W, \delta_Q, \delta_W)$ and $J_{2,x'_i}(Q, W, \delta_Q, \delta_W)$ from Eqs. 47 and Eqs. 44, then substitute them into the definition of d_K in Eq. B1 and evaluate for the case $Q = \tilde{Q}$, $W = \tilde{W}$ to obtain:

$$d_K|_{(Q,W)=(\tilde{Q},\tilde{W})} = \sqrt{N^2 - (Q + W)^2} \Theta_1 + \sqrt{N^2 - (Q - W)^2} \Theta_2 \quad (\text{B5a})$$

where:

$$\Theta_1 = \sqrt{\frac{1 - \cos(\delta_Q + \delta_W - \tilde{\delta}_Q - \tilde{\delta}_W)}{2}} \quad (\text{B5b})$$

$$\Theta_2 = \sqrt{\frac{1 - \cos(\delta_Q - \delta_W - \tilde{\delta}_Q + \tilde{\delta}_W)}{2}} \quad (\text{B5c})$$

For a given δ_Q , Eq. B5b will vanish if

$$\tilde{\delta}_Q = \delta_Q + \delta_W - \tilde{\delta}_W + 2\pi k_1 \quad (\text{B6a})$$

and Eq. B5c will vanish if

$$\tilde{\delta}_Q = \delta_Q - \delta_W + \tilde{\delta}_W + 2\pi k_2 \quad (\text{B6b})$$

where $k_i = 0, \pm 1, \pm 2, \dots$. These two equations can be simultaneously satisfied only if $(\delta_W - \tilde{\delta}_W) = k_3\pi$, ($k_3 = 0, \pm 1, \pm 2, \dots$). But since the δ_W coordinate is π periodic, all such points mean $\delta_W = \tilde{\delta}_W$ and we recover the trivial fact that Pauli orbits with the same values of (Q, W, δ_W) are identified. But suppose $\delta_W \neq \tilde{\delta}_W$ and consider the limit of Eq. B5a as W approaches $\pm(N - |Q|)$.

$$\lim_{W \rightarrow \pm(N-|Q|)} d_K = 2(N \pm Q)(|Q| \mp Q)\Theta_1 + 2(N \mp Q)(|Q| \pm Q)\Theta_2 \quad (\text{B7})$$

For $Q = 0$, or $Q = \pm N$, both terms in Eq. B7 vanish, consistent with the fact that at these four points, the phase space consists of a single Kepler orbit. For all Q with $0 < |Q| < N$, either the term proportional to Θ_1 , or the term proportional to Θ_2 , will vanish as $W \rightarrow \pm(N - |Q|)$. The surviving term can always be made to vanish by taking the limit at the fixed value of $\tilde{\delta}_Q$ such that the required equation (Eq. B6b) or (Eq. B6a) is satisfied. That is, for any δ_Q, δ_W and $\tilde{\delta}_W$, there exists a $\tilde{\delta}_Q$, depending linearly on δ_Q , such that the limit (Eq. B7) vanishes.

Part V

Supplements to Part IV

APPENDIX C: SUPPLEMENTARY MATERIAL

In this section we present three additional appendices for reference which contain detailed expositions of: the Kepler and Pauli averaging calculations (appendices C and D respectively), and the analysis of the fully reduced Hamiltonian h_2 (appendix E).

APPENDIX C: DETAILED KEPLER AVERAGING

1. The connection between the space fixed frame and the orbital plane

The transformation connecting the instantaneous orbital frame to the space fixed frame is a rotation of a three dimensional vector space. Denoting an orthonormal basis in the orbital frame with primed unit vectors, and the space fixed orthonormal basis with unprimed unit vectors, the rotation may be represented by the matrix of direction cosines R .

$$R = \begin{bmatrix} \hat{x} \cdot \hat{x}' & \hat{y} \cdot \hat{x}' & \hat{z} \cdot \hat{x}' \\ \hat{x} \cdot \hat{y}' & \hat{y} \cdot \hat{y}' & \hat{z} \cdot \hat{y}' \\ \hat{x} \cdot \hat{z}' & \hat{y} \cdot \hat{z}' & \hat{z} \cdot \hat{z}' \end{bmatrix} \quad (C.1)$$

One may express the components of R or R^T in terms of Delaunay Coordinates, or the components of any three orthonormal vectors in the orbital reference frame. The components of R^T written as functions of the Delaunay action angle coordinates are:

$$R^T = \begin{bmatrix} \cos \varphi_p \cos \Omega - \sin \varphi_p \sin \Omega \cos i & -\sin \varphi_p \cos \Omega - \cos \varphi_p \sin \Omega \cos i & \sin \Omega \sin i \\ \cos \varphi_p \sin \Omega + \sin \varphi_p \cos i \cos \Omega & -\sin \varphi_p \sin \Omega + \cos \varphi_p \cos i \cos \Omega & -\sin i \cos \Omega \\ \sin \varphi_p \sin i & \cos \varphi_p \sin i & \cos i \end{bmatrix} \quad (C.2)$$

R^T is independent of the principal action and angle coordinates N and φ_n , but the inclination of the orbital plane is a function of the Delaunay actions L and L_z through the definition $i = \cos^{-1}(L_z/L)$.

Alternatively, we make the following choice of orthonormal basis for the orbital frame:

(1) The x' unit vector is \mathbf{M}/M . (2) The z' unit vector is \mathbf{L}/L . (3) The y' unit vector is $\mathbf{L} \times \mathbf{M}/LM$. With this choice of basis we have the following matrix transformation, equivalent to (C.2):

$$\mathbf{R}^T = \begin{bmatrix} \frac{M_x}{M} & \frac{L_y M_z - L_z M_y}{ML} & \frac{L_x}{L} \\ \frac{M_y}{M} & \frac{L_z M_x - L_x M_z}{ML} & \frac{L_y}{L} \\ \frac{M_z}{M} & \frac{L_x M_y - L_y M_x}{ML} & \frac{L_z}{L} \end{bmatrix} \quad (\text{C.3})$$

2. Averaging over Kepler orbits:

The configuration projection of a Kepler orbit is an ellipse, which as a curve in the orbital plane, depends on only two parameters, the eccentricity e and Semimajor axis a (*see ch. 3 sect 23 Born or 3.8 Goldstein*). These quantities may be defined in terms of the Delaunay actions L and N .

The semi-major axis a depends only on the principal action,

$$a = N^2 = L^2 + M^2. \quad (\text{C.4})$$

The eccentricity e depends only on the ratio of the total angular momentum to the principal action,

$$e = \sqrt{1 - L^2/N^2} = M/N. \quad (\text{C.5})$$

3. Averaging and the eccentric anomaly:

Averages of functions over the 1 dimensional Kepler phase space trajectories of given orbital elements are averages over the principal Delaunay angle φ_n with all other variables held fixed.

$$\langle g \rangle_{\varphi_n} \equiv \frac{1}{2\pi} \int_0^{2\pi} g d\varphi_n \quad (C.6)$$

It is useful to re-express this integral in terms of the eccentric anomaly ψ . The principal angle is related to ψ by Kepler's equation:

$$\varphi_n \equiv (\psi - e \sin \psi) \quad (C.7)$$

This substitution yields the following convenient integral expression for the computation of the average value of a function over a Kepler orbit:

$$\langle g \rangle_{\varphi_n} = \frac{1}{2\pi} \int_0^{2\pi} g(1 - e \cos \psi) d\psi \quad (C.8)$$

Since these averages are to be taken over a fixed Kepler orbit, the averages of tensor functions may be calculated in the orbital frame and then transformed into the space fixed frame via R^T .

4. Table of Kepler averages:

All of the following averages are easily obtained analytically by straightforward evaluation of integration over ψ . Examining equation (C.8) one finds that the Kepler average of any odd function of ψ vanishes. Some nonzero averages we need later are:

g	$\langle g \rangle_{\varphi_n}$	g	$\langle g \rangle_{\varphi_n}$	g	$\langle g \rangle_{\varphi_n}$	g	$\langle g \rangle_{\varphi_n}$
$\cos \psi$	$-1/2e$	$\cos^2 \psi$	$1/2$	$\cos \psi \sin^2 \psi$	$-1/8 e$	$\sin^2 \psi / (1 - e \cos \psi)$	$1/2$
		$\sin^2 \psi$	$1/2$	$\cos^3 \psi$	$-3/8 e$	$\cos^2 \psi \sin^2 \psi / (1 - e \cos \psi)$	$1/8$

5. Average position vector:

$$\langle \vec{r} \rangle_{\varphi_n} = \langle x' \rangle_{\varphi_n} \hat{x}' + \langle y' \rangle_{\varphi_n} \hat{y}' + \langle z' \rangle_{\varphi_n} \hat{z}' \quad (C.9)$$

The components of the position of the electron may be written in the orbital coordinate frame, constructed with the origin located at the nucleus, the x' axis directed towards the perihelion, the z' axis is in the direction along the angular momentum: and y' axis perpendicular to both such that (x',y',z') form a right-handed coordinate system. In the orbital plane $z'=0$ and x' and y' are expressed in terms of the eccentric anomaly by the equations:

$$x' = N^2(\cos \psi - e) , y' = NL \sin \psi , \text{ and } z' = 0 \quad (\text{C.10})$$

Geometrically, y' is the semi-minor axis times the sine of the eccentric anomaly while x' is the semi-major axis times the cosine of the eccentric anomaly displaced from the center of the ellipse to the solar focus. The averages of the components of the position vector in the orbital frame are obtained by substituting the functions $x'(\psi)$ and $y'(\psi)$ (C.10) into the definition of the averaging operation (C.8) and integrating over the eccentric anomaly. One finds:

$$\langle x' \rangle_{\varphi_n} = -\frac{3}{2} N^2 e = -\frac{3}{2} NM , \text{ and } \langle y' \rangle_{\varphi_n} = 0 \quad (\text{C.11})$$

6. Average second moment position tensor:

The second moment position tensor is a nine component tensor consisting of the averages of all quadratic coordinate functions.

$$\langle \bar{r} \bar{r}' \rangle = \sum_{i,j} \langle q'_i q'_j \rangle_{\varphi_n} \hat{q}'_i \hat{q}'_j \quad (\text{C.12})$$

Any component containing a z' vanishes as the configuration coordinates of all points on the orbit lie within the orbital plane. Also, any odd power of y' is symmetric about the x' axis and vanishes upon averaging. The nonzero components are thus:

$$\langle rr \rangle = \langle x' x' \rangle_{\varphi_n} \hat{x}' \hat{x}' + \langle y' y' \rangle_{\varphi_n} \hat{y}' \hat{y}' \quad (\text{C.13})$$

Expressions for the components are obtained by using the averaging operation (C.8) on products of the functions $x'(\psi)$ and $y'(\psi)$ (C.10). One finds;

$$\langle x'x' \rangle_{\varphi_n} = N^2 \left(\frac{1}{2} N^2 + 2N^2 e^2 \right) = N^2 \left(\frac{1}{2} N^2 + 2M^2 \right) \quad (\text{C.14})$$

and:

$$\langle y'y' \rangle_{\varphi_n} = N^2 \frac{1}{2} (N^2 - N^2 e^2) = N^2 \frac{1}{2} L^2 \quad (\text{C.15})$$

7. The zero order Hamiltonian

Immediately we have: $\bar{H}_0 = \langle H_0 \rangle_{\varphi_n} = -\frac{1}{2N^2}$ (C.16)

8. The Pauli Hamiltonian

The first order Hamiltonian is: $H_1 = \frac{B}{2} L_z + F_x x$ (C.17)

For a fixed Kepler orbit L_z is constant, and therefore the Kepler average of (C.17) is:

$$\bar{H}_1 = \langle H_1 \rangle_{\varphi_n} = \frac{B}{2} L_z + F_x \langle x \rangle_{\varphi_n} \quad (\text{C.18})$$

Using: $\bar{\mathbf{r}} = \mathbf{R}^T \bar{\mathbf{r}}'$ and noting that \mathbf{R}^T is independent of φ_n , the averages are calculated from (C.11):

$$\langle x \rangle_{\varphi_n} = \langle \mathbf{R}_{11}^T x' + \mathbf{R}_{12}^T y' \rangle_{\varphi_n} = \mathbf{R}_{11}^T \langle x' \rangle_{\varphi_n} + \mathbf{R}_{12}^T \langle y' \rangle_{\varphi_n} = -\mathbf{R}_{11}^T \frac{3}{2} NM = -\frac{3}{2} NM_x \quad (\text{C.19})$$

Such that one recovers the Pauli Hamiltonian: $\langle H_1 \rangle_{\varphi_n} = \frac{B}{2} L_z - \frac{3}{2} NF_x M_x$ (C.20)

9. The second order perturbation terms

According to the perturbation expansion, the second order Hamiltonian assumes the following form:

$$\bar{H}_2 = \langle H_2 \rangle_{\varphi_n} + \left\langle \frac{\partial H_1}{\partial N} \frac{\partial f_1}{\partial \varphi_n} \right\rangle_{\varphi_n} + \left\langle \frac{\partial H_1}{\partial L} \frac{\partial f_1}{\partial \varphi_p} \right\rangle_{\varphi_n} + \left\langle \frac{\partial H_1}{\partial L_z} \frac{\partial f_1}{\partial \Omega} \right\rangle_{\varphi_n} + \frac{1}{2} \frac{\partial^2 H_o}{\partial N^2} \left\langle \left(\frac{\partial f_1}{\partial \varphi_n} \right)^2 \right\rangle_{\varphi_n}$$

(C.21)

a. *The diamagnetic and z-Stark terms*

An expression for the first term in (C.21) is obtained using the results for the averaged second moment tensor. This Evaluation of this term essentially parallels the procedure used in the appendix of (*Waterland/Delos & also see Delos/Knudsen/Noid*) but here we express the components of R^T as functions of the \mathbf{L} and \mathbf{M} vectors instead of the Delaunay action and angle variables.

$$H_2 = \frac{B^2}{8}(\mathbf{x}\mathbf{x} + \mathbf{y}\mathbf{y}) + F_z z \quad (C.22)$$

The Kepler average of this is: $\langle H_2 \rangle_{\varphi_n} = \frac{B^2}{8} \left(\langle \mathbf{x}\mathbf{x} \rangle_{\varphi_n} + \langle \mathbf{y}\mathbf{y} \rangle_{\varphi_n} \right) + F_z \langle z \rangle_{\varphi_n}$ (C.23)

The average of z is calculated analogously to (C.19) and is equal to $-3/2NM_z$. $\mathbf{x}\mathbf{x}$ and $\mathbf{y}\mathbf{y}$ are two of the space fixed components of the nine element $\mathbf{r}\mathbf{r}$ tensor. We express this tensor in terms of the components in the orbital frame and then average.

$$\langle \mathbf{r}\mathbf{r} \rangle_{\varphi_n} = \langle \mathbf{R}^T \mathbf{r}' \mathbf{r}' \mathbf{R} \rangle_{\varphi_n} = \mathbf{R}^T \langle \mathbf{r}' \mathbf{r}' \rangle_{\varphi_n} \mathbf{R} \quad (C.24)$$

Performing the matrix multiplication, using the definition of the transpose, and using the orthonormality of the rows and columns of \mathbf{R}^T one obtains:

$$\langle H_2 \rangle_{\varphi_n} = \frac{B^2}{8} \left[\langle \mathbf{x}' \mathbf{x}' \rangle_{\varphi_n} + \left(\langle \mathbf{y}' \mathbf{y}' \rangle_{\varphi_n} - \langle \mathbf{x}' \mathbf{x}' \rangle_{\varphi_n} \right) \mathbf{R}_{31}^T \mathbf{R}_{31}^T + \mathbf{R}_{33}^T \mathbf{R}_{33}^T \langle \mathbf{y}' \mathbf{y}' \rangle_{\varphi_n} \right] \quad (C.25)$$

Substituting expressions (C.14) and (C.15) for $\langle \mathbf{x}' \mathbf{x}' \rangle$ and $\langle \mathbf{y}' \mathbf{y}' \rangle$ into (C.25), simplifying with (C.4), and expressing the components of \mathbf{R}^T as the functions of \mathbf{L} and \mathbf{M} given in (C.3) one finds;

$$\langle H_2 \rangle_{\varphi_n} = \frac{B^2}{8} \frac{N^2}{2} [N^2 + 4M^2 - 5M_z^2 + L_z^2] - \frac{3}{2} N F_z M_z \quad (C.26)$$

b. Perturbation expansion terms:

The remaining terms depend on the form of the first order generating function. The perturbation theory implies that f_1 must satisfy the following partial differential equation:

$$\frac{\partial f_1}{\partial \varphi_n} = N^3 \left[\langle H_1 \rangle_{\varphi_n} - H_1 \right] \quad (C.27)$$

This equation was derived from the requirement that f_1 must be periodic in the mean anomaly φ_n . We obtain a form for f_1 by the indefinite integration of (C.27) over φ_n .

$$f_1 = \int_0^{\varphi_n} \frac{\partial f_1}{\partial \varphi_n} d\varphi_n = N^3 \int_0^{\varphi_n} \left[\langle H_1 \rangle_{\varphi_n} - H_1 \right] d\varphi_n + C \equiv \tilde{f}_1 + C \quad (C.28)$$

where C is independent of φ_n . We choose C such that $\langle f_1 \rangle = 0$.

$$C = -\langle \tilde{f}_1 \rangle_{\varphi_n} \quad (C.29)$$

$$\text{Thus: } f_1 = \tilde{f}_1 - \langle \tilde{f}_1 \rangle_{\varphi_n} \quad (C.30)$$

With this choice the calculation of the second order terms in (C.21) are simplified by substituting (C.17) for H_1 and (C.30) for f_1 which reduces the four terms into the following form:

$$\left\langle \frac{\partial H_1}{\partial N} \frac{\partial f_1}{\partial \varphi_n} \right\rangle_{\varphi_n} = F_x \left\langle \frac{\partial x}{\partial N} \frac{\partial \tilde{f}_1}{\partial \varphi_n} \right\rangle_{\varphi_n} \quad (C.31)$$

$$\left\langle \frac{\partial H_1}{\partial L} \frac{\partial f_1}{\partial \varphi_p} \right\rangle_{\varphi_n} = F_x \left[\left\langle \frac{\partial x}{\partial L} \frac{\partial \tilde{f}_1}{\partial \varphi_p} \right\rangle_{\varphi_n} - \frac{\partial \langle x \rangle_{\varphi_n}}{\partial L} \frac{\partial \langle \tilde{f}_1 \rangle_{\varphi_n}}{\partial \varphi_p} \right] \quad (C.32)$$

$$\left\langle \frac{\partial H_1}{\partial L_z} \frac{\partial f_1}{\partial \Omega} \right\rangle_{\varphi_n} = F_x \left[\left\langle \frac{\partial x}{\partial L_z} \frac{\partial \tilde{f}_1}{\partial \Omega} \right\rangle_{\varphi_n} - \frac{\partial \langle x \rangle_{\varphi_n}}{\partial L_z} \frac{\partial \langle \tilde{f}_1 \rangle_{\varphi_n}}{\partial \Omega} \right] \quad (C.33)$$

$$\frac{1}{2} \frac{\partial^2 H_0}{\partial N^2} \left\langle \left(\frac{\partial f_1}{\partial \varphi_n} \right)^2 \right\rangle_{\varphi_n} = -\frac{3}{2} \frac{1}{N^4} \left\langle \left(\frac{\partial \tilde{f}_1}{\partial \varphi_n} \right)^2 \right\rangle_{\varphi_n} \quad (C.34)$$

Notice that the terms proportional to the magnetic field have vanished from (C.33) by our choice of the constant C. In the next section we will find that f_1 is first order in electric field. It follows that terms proportional to $F_x B$ have been eliminated with our choice of C.

10. The explicit first order generating function

An explicit form for f_1 may be obtained from its differential equation in the Delaunay coordinates as follows. Substituting the explicit forms of H_1 and $\langle H_1 \rangle$ as given in (C.17) and (C.18) into the differential equation for f_1 (C.27) one finds:

$$\frac{\partial f_1}{\partial \varphi_n} = -N^3 F_x \left(x - \langle x \rangle_{\varphi_n} \right) \quad (C.35)$$

Now f_1 may be obtained by indefinite integration along the fixed unperturbed Kepler orbit.

This implies:

$$f_1 = -N^3 F_x \left(\int_0^{\varphi_n} x d\varphi_n - \langle x \rangle_{\varphi_n} \varphi_n \right) + C \quad (C.36)$$

Expressing the mean anomaly and its differential in terms of the eccentric anomaly via Kepler's equation.

$$f_1 = -N^3 F_x \int_0^{\varphi_n} x(1 - e \cos \psi') d\psi' - \langle x \rangle_{\varphi_n} (\psi - e \sin \psi) + C \quad (C.37)$$

To compute the integrals; express x as a function of the eccentric anomaly through the equation: $\mathbf{r} = \mathbf{R}^T \mathbf{r}'$ and the functions $x'(\psi)$, $y'(\psi)$, and $z'(\psi)$ given in (C.10).

$$x = \mathbf{R}_{11}^T N^2 (\cos \psi - e) + \mathbf{R}_{12}^T N L \sin \psi \quad (C.38)$$

Finally express the average $\langle x \rangle$ as:

$$\langle x \rangle_{\varphi_n} = \mathbf{R}_{11}^T \left(-\frac{3}{2} N^2 e \right) \quad (C.39)$$

When (C.38) and (C.39) are substituted into (C.37), the resulting expression simplifies to:

$$f_1 = -N^3 \left[F_x \mathbf{R}_{11}^T N^2 \left(I_1 + \frac{3}{2} e (\psi - e \sin \psi) \right) + F_x \mathbf{R}_{12}^T N L I_2 \right] + C \quad (C.40)$$

$$\text{where: } I_1 = \int_0^{\psi} (\cos \psi' - e)(1 - e \cos \psi') d\psi' = (1 + e^2) \sin \psi - \frac{e}{2} \sin \psi \cos \psi - \frac{3e}{2} \psi$$

$$\text{and } I_2 = \int_0^{\psi} \sin \psi' (1 - e \cos \psi') d\psi' = 1 - \frac{e}{2} - \cos \psi + \frac{e}{2} \cos^2 \psi$$

Upon substitution, collection and simplification of like terms (with terms linearly proportional to ψ canceling out) one obtains:

$$f_1 = -N^5 F_x \mathbf{R}_{11}^T \left(\left(1 - \frac{1}{2} e^2 \right) \sin \psi - \frac{e}{2} \sin \psi \cos \psi \right) - N^4 L F_x \mathbf{R}_{12}^T \left(1 - \frac{e}{2} - \cos \psi + \frac{e}{2} \cos^2 \psi \right) + C \quad (C.41)$$

Averaging (C.41) over a Kepler orbit gives an expression for C :

$$\langle \tilde{f}_1 \rangle_{\varphi_n} = -N^4 L F_x \mathbf{R}_{12}^T \left(1 + \frac{e}{4} \right) = -C \quad (C.42)$$

a. Averaging Eq. (C.32)

The only angular dependence of (C.42) is contained in the matrix elements of \mathbf{R}^T such that:

$$\frac{\partial \langle \tilde{f}_1 \rangle_{\varphi_n}}{\partial \varphi_p} = -N^4 L \left[F_x \frac{\partial R_{12}^T}{\partial \varphi_p} \left(1 + \frac{e}{4} \right) \right] \quad (C.43)$$

And it is simple to calculate:

$$\frac{\partial \langle x \rangle}{\partial L} = -\frac{3}{2} N^2 e \frac{\partial R_{11}^T}{\partial L} + \frac{3}{2} \frac{L}{e} R_{11}^T \quad (C.44)$$

Where we have used the partial derivative of the eccentricity (C.5) with respect to L holding all other Delaunay variables fixed.

$$\frac{\partial e}{\partial L} = \frac{\partial}{\partial L} \sqrt{1 - \frac{L^2}{N^2}} = -\frac{1}{e} \frac{L}{N^2} \quad (C.45)$$

Substitution of (C.43) and (C.44) into (C.33) yields:

$$\left\langle \frac{\partial H_1}{\partial L} \frac{\partial f_1}{\partial \varphi_p} \right\rangle_{\varphi_n} = F_x \left\langle \frac{\partial x}{\partial L} \frac{\partial \tilde{f}_1}{\partial \varphi_p} \right\rangle - \frac{3}{2} N^6 L \left(e + \frac{e^2}{4} \right) F_x F_x \frac{\partial R_{11}^T}{\partial L} \frac{\partial R_{12}^T}{\partial \varphi_p} + \frac{3}{2} N^4 L^2 \left(\frac{1}{e} + \frac{1}{4} \right) F_x F_x R_{11}^T \frac{\partial R_{12}^T}{\partial \varphi_p}$$

(C.46)

We have left to calculate the first term in (C.46). Taking the derivative of x (C.38) with respect to L yields:

$$\begin{aligned} \frac{\partial x}{\partial L} &= \left\{ \frac{\partial R_{11}^{\text{dag}}}{\partial L} \right\} N^2 (\cos \psi - e) + \left\{ \frac{\partial R_{12}^{\text{dag}}}{\partial L} \right\} N L \sin \psi \\ &+ R_{11}^{\text{dag}} \frac{L}{e} \left(\frac{\sin^2 \psi}{(1 - e \cos \psi)} + 1 \right) + R_{12}^{\text{dag}} N \left(\sin \psi - \frac{L^2}{e N^2} \left\{ \frac{\cos \psi \sin \psi}{(1 - e \cos \psi)} \right\} \right) \end{aligned} \quad (C.47)$$

Where we have made use of (C.45) as before, and we also have used the partial derivative of the eccentric anomaly with respect to L holding the remaining Delaunay coordinates fixed.

This is calculated by implicit differentiation of Kepler's equation (C.7) in the Delaunay coordinates.

$$\frac{\partial \varphi_n}{\partial L} = 0 = (1 - e \cos \psi) \frac{\partial \psi}{\partial L} - \frac{\partial e}{\partial L} \sin \psi \rightarrow \frac{\partial \psi}{\partial L} = -\frac{L}{e N^2} \frac{\sin \psi}{(1 - e \cos \psi)} \quad (C.48)$$

The angular dependence of the first order generating function is limited to the matrix elements of R^T since Kepler's equation depends only on N , L and φ_n such that $d\psi/d\varphi_p = 0$.

Therefore;

$$\begin{aligned} \frac{\partial \tilde{f}_1}{\partial \varphi_p} = & -N^5 \left[F_x \frac{\partial R_{11}^T}{\partial \varphi_p} \left(\left(1 - \frac{1}{2} e^2 \right) \sin \psi - \frac{e}{2} \sin \psi \cos \psi \right) \right] - N^4 L \left[F_x \frac{\partial R_{12}^T}{\partial \varphi_p} \left(1 - \frac{e}{2} - \cos \psi + \frac{e}{2} \cos^2 \psi \right) \right] \end{aligned} \quad (C.49)$$

Multiplying (C.47) and (C.49) and Kepler averaging the resulting expression yields:

$$\begin{aligned} \left\langle \frac{\partial x}{\partial L} \frac{\partial \tilde{f}_1}{\partial \varphi_p} \right\rangle_{\varphi_n} = & N^6 L F_x \frac{\partial R_{11}^T}{\partial L} \frac{\partial R_{12}^T}{\partial \varphi_p} \left(\frac{1}{2} + \frac{3}{2} e + \frac{3}{16} e^2 \right) - N^6 L F_x \frac{\partial R_{12}^T}{\partial L} \frac{\partial R_{11}^T}{\partial \varphi_p} \left(\frac{1}{2} - \frac{3}{16} e^2 \right) \quad (C.50) \\ & - N^4 \frac{L^2}{e} F_x R_{11}^T \frac{\partial R_{12}^T}{\partial \varphi_p} \left(\frac{3}{2} + e \frac{1}{16} \right) - N^6 F_x R_{12}^T \frac{\partial R_{11}^T}{\partial \varphi_p} \left[\frac{1}{2} - \frac{3}{16} e^2 + \frac{1}{16} \frac{L^2}{N^2} \right] \end{aligned}$$

A significant simplification is achieved by using the relations:

$$\frac{\partial R_{11}^T}{\partial \varphi_p} = R_{12}^T \quad \text{and} \quad \frac{\partial R_{12}^T}{\partial \varphi_p} = -R_{11}^T \quad (C.51)$$

These relations are easily proved by expressing R^T components as functions of the Delaunay Variables (C.2) and explicitly computing their derivatives. We find:

$$\begin{aligned} \left\langle \frac{\partial x}{\partial L} \frac{\partial \tilde{f}_1}{\partial \varphi_p} \right\rangle_{\varphi_n} = & N^6 L F_x \frac{\partial R_{11}^T}{\partial L} \frac{\partial R_{12}^T}{\partial \varphi_p} \left(\frac{1}{2} + \frac{3}{2} e + \frac{3}{16} e^2 \right) - N^6 L F_x \frac{\partial R_{12}^T}{\partial L} \frac{\partial R_{11}^T}{\partial \varphi_p} \left(\frac{1}{2} - \frac{3}{16} e^2 \right) \quad (C.52) \\ & + N^4 \frac{L^2}{e} F_x R_{11}^T R_{11}^T \left(\frac{3}{2} + e \frac{1}{16} \right) - N^6 F_x R_{12}^T R_{12}^T \left[\frac{1}{2} - \frac{3}{16} e^2 + \frac{1}{16} \frac{L^2}{N^2} \right] \end{aligned}$$

Multiplying this expression by the F_x and substituting the result back into the entire expression (C.46), simplifying and gathering like terms yields:

$$\begin{aligned} \left\langle \frac{\partial H_1}{\partial L} \frac{\partial f_1}{\partial \varphi_p} \right\rangle_{\varphi_n} &= N^6 L \left(\frac{1}{2} - \frac{3}{16} e^2 \right) F_x F_x \left\{ \frac{\partial R_{11}^T}{\partial L} \frac{\partial R_{12}^T}{\partial \varphi_p} - \frac{\partial R_{12}^T}{\partial L} \frac{\partial R_{11}^T}{\partial \varphi_p} \right\} \\ &- N^4 L^2 \frac{5}{16} F_x F_x R_{11}^T R_{11}^T - N^6 \left[\frac{1}{2} - \frac{3}{16} e^2 + \frac{1}{16} \frac{L^2}{N^2} \right] F_x F_x R_{12}^T R_{12}^T \end{aligned} \quad (C.53)$$

b. *Averaging Eq. (C.33)*

The term (C.33) is calculated by following the same steps used above to calculate (C.32).

However, this calculation is simpler because the eccentric anomaly does not depend on L_z .

The analogous steps yield:

$$\left\langle \frac{\partial H_1}{\partial L_z} \frac{\partial f_1}{\partial \Omega} \right\rangle_{\varphi_n} = N^6 L \left[\frac{1}{2} - \frac{3}{16} e^2 \right] F_x F_x \left[\frac{\partial R_{11}^T}{\partial L_z} \frac{\partial R_{12}^T}{\partial \Omega} - \frac{\partial R_{12}^T}{\partial L_z} \frac{\partial R_{11}^T}{\partial \Omega} \right] \quad (C.54)$$

c. *Averaging Eqs. (C.31) and (C.34)*

It is straightforward to calculate (C.31). Since C is independent of φ_n we have:

$$\frac{\partial \tilde{f}_1}{\partial \varphi_n} = \frac{\partial f_1}{\partial \varphi_n} = -N^3 F_x \left(\mathbf{x} - \langle \mathbf{x} \rangle_{\varphi_n} \right) \quad (C.55)$$

Using this expression to expand the terms, and moving the derivatives with respect to N outside the averages yields:

$$\left\langle \frac{\partial H_1}{\partial N} \frac{\partial f_1}{\partial \varphi_n} \right\rangle_{\varphi_n} = -N^3 F_x F_x \frac{1}{2} \frac{\partial}{\partial N} \left[\langle \mathbf{x} \mathbf{x} \rangle_{\varphi_n} - \langle \mathbf{x} \rangle_{\varphi_n} \langle \mathbf{x} \rangle_{\varphi_n} \right] \quad (C.56)$$

These averages are calculated from (C.11) and (C.12) and simplified using (C.5) yielding:

$$\left[\langle \mathbf{x} \mathbf{x} \rangle_{\varphi_n} - \langle \mathbf{x} \rangle_{\varphi_n} \langle \mathbf{x} \rangle_{\varphi_n} \right] = R_{11}^{T^2} \left(\frac{N^4}{4} + \frac{N^2 L^2}{4} \right) + R_{12}^{T^2} \frac{N^2 L^2}{2} \quad (C.57)$$

such that:

$$\left\langle \frac{\partial H_1}{\partial N} \frac{\partial f_1}{\partial \varphi_n} \right\rangle_{\varphi_n} = -N^4 \frac{1}{2} \left(N^2 + \frac{1}{2} L^2 \right) F_x F_x R_{11}^T R_{11}^T - N^4 \frac{1}{2} L^2 F_x F_x R_{12}^T R_{12}^T \quad (C.58)$$

The last term (C.34) is calculated similarly and the result is:

$$\frac{1}{2} \frac{\partial^2 H_o}{\partial n^2} \left\langle \left(\frac{\partial f_1}{\partial \varphi_n} \right)^2 \right\rangle_{\varphi_n} = -N^4 \frac{3}{8} (N^2 + L^2) F_x F_x R_{11}^T R_{11}^T - N^4 \frac{3}{4} L^2 F_x F_x R_{12}^T R_{12}^T \quad (C.59)$$

d. Summation and simplification of the second order perturbation terms

Summing all the terms in (C.53), (C.54), (C.58) and (C.59) together and simplifying yields:

$$\begin{aligned} & \left\langle \frac{\partial H_1}{\partial L} \frac{\partial f_1}{\partial \varphi_p} \right\rangle_{\varphi_n} + \left\langle \frac{\partial H_1}{\partial N} \frac{\partial f_1}{\partial \varphi_n} \right\rangle_{\varphi_n} + \frac{1}{2} \frac{\partial^2 H_o}{\partial n^2} \left\langle \left(\frac{\partial f_1}{\partial \varphi_n} \right)^2 \right\rangle_{\varphi_n} + \left\langle \frac{\partial H_1}{\partial L_z} \frac{\partial f_1}{\partial \Omega} \right\rangle_{\varphi_n} = \\ & N^6 L \left(\frac{1}{2} - \frac{3}{16} e^2 \right) F_x F_x \left[\left\{ \frac{\partial R_{11}^T}{\partial L} \frac{\partial R_{12}^T}{\partial \varphi_p} - \frac{\partial R_{12}^T}{\partial L} \frac{\partial R_{11}^T}{\partial \varphi_p} \right\} + \left\{ \frac{\partial R_{11}^T}{\partial L_z} \frac{\partial R_{12}^T}{\partial \Omega} - \frac{\partial R_{12}^T}{\partial L_z} \frac{\partial R_{11}^T}{\partial \Omega} \right\} \right] \quad (C.60) \\ & - N^4 \frac{1}{16} [14N^2 + 15L^2] F_x F_x R_{11}^T R_{11}^T - N^4 \frac{1}{16} [5N^2 + 24L^2] F_x F_x R_{12}^T R_{12}^T \end{aligned}$$

This expression simplifies considerably with the use of the following identity:

$$\left\{ \frac{\partial R_{11}^T}{\partial L} \frac{\partial R_{12}^T}{\partial \varphi_p} - \frac{\partial R_{12}^T}{\partial L} \frac{\partial R_{11}^T}{\partial \varphi_p} \right\} + \left\{ \frac{\partial R_{11}^T}{\partial L_z} \frac{\partial R_{12}^T}{\partial \Omega} - \frac{\partial R_{12}^T}{\partial L_z} \frac{\partial R_{11}^T}{\partial \Omega} \right\} = -\frac{1}{L} R_{13}^T R_{13}^T \quad (C.61)$$

This identity is proved in a straightforward but tedious manner using (C.2), together with $\cos i = L_z/L$. (Alternatively, one could use (C.3) and the Poisson brackets of the components of the \mathbf{L} and \mathbf{M} vectors.)

Substituting the identity (C.61) into (C.60) and simplifying using the orthonormality of the R^T matrix to eliminate the R_{12}^T components, one obtains:

$$\begin{aligned} & \left\langle \frac{\partial H_1}{\partial L} \frac{\partial f_1}{\partial \varphi_p} \right\rangle_{\varphi_n} + \left\langle \frac{\partial H_1}{\partial N} \frac{\partial f_1}{\partial \varphi_n} \right\rangle_{\varphi_n} + \left\langle \frac{\partial H_1}{\partial L_z} \frac{\partial f_1}{\partial \Omega} \right\rangle_{\varphi_n} + \frac{1}{2} \frac{\partial^2 H_o}{\partial n^2} \left\langle \left(\frac{\partial f_1}{\partial \varphi_n} \right)^2 \right\rangle_{\varphi_n} = \\ & - N^4 \frac{1}{16} F_x F_x [29N^2 - 24M^2 - 21L^2 R_{13}^T R_{13}^T + 9M^2 R_{11}^T R_{11}^T] \end{aligned}$$

(C.62)

Finally, substituting components from (C.3) into (C.62), and summing with (C.26), the second order terms in the Hamiltonian may be written:

$$\begin{aligned}
& \langle H_2 \rangle_{\varphi_n} + \left\langle \frac{\partial H_1}{\partial L} \frac{\partial f_1}{\partial \varphi_p} \right\rangle_{\varphi_n} + \left\langle \frac{\partial H_1}{\partial N} \frac{\partial f_1}{\partial \varphi_n} \right\rangle_{\varphi_n} + \left\langle \frac{\partial H_1}{\partial L_z} \frac{\partial f_1}{\partial \Omega} \right\rangle_{\varphi_n} + \frac{1}{2} \frac{\partial^2 H_0}{\partial n^2} \left\langle \left(\frac{\partial f_1}{\partial \varphi_n} \right)^2 \right\rangle_{\varphi_n} = \\
& \frac{B^2 N^2}{16} [N^2 + 4M^2 - 5M_z^2 + L_z^2] - \frac{3}{2} N F_z M_z - \frac{F_x^2 N^4}{16} [29N^2 - 24M^2 - 21L_x^2 + 9M_x^2]
\end{aligned}$$

(C.63)

APPENDIX D: DETAILED PAULI PRECESSION AVERAGING

1. The Pauli Precession Orbit

The specification of the space fixed electric and magnetic fields allows the definition of Pauli's effective field vectors $\mathbf{\Omega}_1$ and $\mathbf{\Omega}_2$, defined by:

$$\bar{\mathbf{\Omega}}_1 \equiv \left[\frac{1}{2} \bar{\mathbf{B}} - \frac{3}{2} N \bar{\mathbf{F}} \right] \quad \text{and} \quad \bar{\mathbf{\Omega}}_2 \equiv \left[\frac{1}{2} \bar{\mathbf{B}} + \frac{3}{2} N \bar{\mathbf{F}} \right] \quad (\text{D.1})$$

For perpendicular fields $\mathbf{B} \cdot \mathbf{F} = 0$, $\mathbf{\Omega}_1$ and $\mathbf{\Omega}_2$ have identical magnitudes equal to:

$$\omega_f = \frac{1}{2} \sqrt{B^2 - (3NF)^2} \quad (\text{D.2})$$

We scale the $\mathbf{\Omega}_i$ vectors by $1/\omega_f$ such that they have unit magnitude at perpendicular fields in order to define the near-perpendicular first order Pauli effective field vectors $\mathbf{\omega}_1$ and $\mathbf{\omega}_2$:

$$\bar{\mathbf{\omega}}_1 \equiv \frac{1}{2\omega_f} B \hat{\mathbf{z}} - \frac{3}{2\omega_f} N F_x \hat{\mathbf{x}} \quad \text{and} \quad \bar{\mathbf{\omega}}_2 \equiv \frac{1}{2\omega_f} B \hat{\mathbf{z}} + \frac{3}{2\omega_f} N F_x \hat{\mathbf{x}} \quad (\text{D.3})$$

We consider each of these two $\mathbf{\omega}_i$ vectors to specify a z axis, thereby defining the following two coordinate frames (x_i, y_i, z_i) for $i = 1, 2$ with the z_i axis aligned with the direction of $\mathbf{\omega}_i$, the y_i axis aligned with the space fixed y axis, and the x_i axis chosen such that the three axes specify a right handed coordinate system.

The transformation between either of these frames and the space fixed frame is given by a linear orthogonal transformation. We represent the corresponding rotations by the matrices of the direction cosines.

$$\begin{bmatrix} \hat{\mathbf{x}}_i \cdot \hat{\mathbf{x}} & \hat{\mathbf{y}}_i \cdot \hat{\mathbf{x}} & \hat{\mathbf{z}}_i \cdot \hat{\mathbf{x}} \\ \hat{\mathbf{x}}_i \cdot \hat{\mathbf{y}} & \hat{\mathbf{y}}_i \cdot \hat{\mathbf{y}} & \hat{\mathbf{z}}_i \cdot \hat{\mathbf{y}} \\ \hat{\mathbf{x}}_i \cdot \hat{\mathbf{z}} & \hat{\mathbf{y}}_i \cdot \hat{\mathbf{z}} & \hat{\mathbf{z}}_i \cdot \hat{\mathbf{z}} \end{bmatrix} = \frac{1}{2\omega_f} \begin{bmatrix} B & 0 & \mp 3NF_x \\ 0 & 2\omega_f & 0 \\ \pm 3NF_x & 0 & B \end{bmatrix} \quad \text{for } i = 1, 2 \quad (\text{D.4})$$

where the upper sign is for $i = 1$ and the lower sign is for $i = 2$.

In reference frame specified by $\mathbf{\omega}_i$, the components of \mathbf{J}_i are expressed as functions of (μ_i, ψ_i) .

$$\bar{J}_i(\mu_i, \psi_i) = \begin{bmatrix} \cos(\psi_i) \sqrt{N^2/4 - \mu_i^2} \\ \sin(\psi_i) \sqrt{N^2/4 - \mu_i^2} \\ \mu_i \end{bmatrix} \quad (D.5)$$

Matrix multiplication by (D.4) provides the components in the space fixed coordinate frame:

$$\bar{J}_i(\mu_i, \psi_i) = \frac{1}{2\omega_f} \begin{bmatrix} B \cos(\psi_i) \sqrt{N^2/4 - \mu_i^2} \mp 3NF_x \mu_i \\ 2\omega_f \sin(\psi_i) \sqrt{N^2/4 - \mu_i^2} \\ \pm 3NF_x \cos(\psi_i) \sqrt{N^2/4 - \mu_i^2} + B\mu_i \end{bmatrix} \quad (D.6)$$

We make the canonical transformation [*The transformation may be enacted by the generating function* $G(\psi_1, \psi_2, Q, W) = \frac{1}{2} Q (\psi_1 + \psi_2) + \frac{1}{2} W (\psi_1 - \psi_2)$]:

$$\mu_1 = \frac{1}{2}(Q+W), \quad \mu_2 = \frac{1}{2}(Q-W), \quad \psi_1 = \delta_Q + \delta_W, \quad \psi_2 = \delta_Q - \delta_W.$$

Since $|\mathbf{J}_i| = N/2$ (Eq. D.3), it follows that the allowed values of the components μ_1 and μ_2 form a closed square with length $[-N/2, N/2]$. It follows that the allowed ranges of Q and W become:

$$-N \leq Q \leq N \quad \text{and} \quad -(N-|Q|) \leq W \leq (N-|Q|) \quad \text{as is illustrated in Fig. 17(a).}$$

The allowed ranges of δ_Q and δ_W can be chosen in a number of ways. For values of Q and W such that both ψ_1 and ψ_2 are defined, they are coordinates on a two torus mod(2π), and it is convenient initially to say that each ranges between $-\pi$ and π . Then, δ_Q would also range from $-\pi$ to π , while δ_W would range from $-(\pi-|\delta_Q|)$ to $(\pi-|\delta_Q|)$. This however, is inconvenient. It is better to tile the (ψ_1, ψ_2) plane as indicated in Fig. 17(b). such that δ_Q and δ_W have the independent ranges:

$$-\pi \leq \delta_Q \leq \pi \quad -\pi/2 \leq \delta_W \leq \pi/2 \quad .$$

Now the space fixed components of the J vectors may be expressed as functions on $(Q, W, \delta_Q, \delta_W)$.

$$J_{i,q} = A_{i,q} \cos(\delta_Q \pm \delta_W) + C_{i,q} \quad \text{for } i=1 \text{ (upper sign) and } i=2 \text{ (lower sign) and } q = x \text{ or } z$$

$$J_{i,y} = A_{i,y} \sin(\delta_Q \pm \delta_w) \quad \text{for } i=1 \text{ (upper sign) and } i=2 \text{ (lower sign)} \quad (\text{D.7})$$

Where for notational convenience we have defined the functions $A_{i,q}(Q,W)$ and $C_{i,q}(Q,W)$ as follows.

$$C_{i,x} = \mp \frac{3NF_x}{4\omega_f} (Q \pm W), \quad A_{i,x} = \frac{B}{4\omega_f} \sqrt{N^2 - (Q \pm W)^2} \quad (\text{D.8.a})$$

$$C_{i,y} = 0, \quad A_{i,y} = \frac{1}{2} \sqrt{N^2 - (Q \pm W)^2} \quad (\text{D.8.b})$$

$$C_{i,z} = \frac{B}{4\omega_f} (Q \pm W), \quad A_{i,z} = \pm \frac{3NF_x}{4\omega_f} \sqrt{N^2 - (Q \pm W)^2} \quad (\text{D.8.c})$$

2. The Averaging Operation

Averages of functions over the one dimensional Pauli phase space trajectories at fixed N,W and δ_w are averages over the principal precessional angle δ_Q .

$$\langle g \rangle_{\delta_Q} \equiv \frac{1}{2\pi} \oint g \, d\delta_Q \quad (\text{D.9})$$

The quantities that are to be averaged are may be expressed as functions of the space fixed components of the \mathbf{J} vectors. The averages are then easily computed by expressing these components as they appear in (D.8).

3. Averaging terms Linear in space fixed \mathbf{J} components

Since the average of sinusoids over the 2π interval vanish, when expressions (D.7) are Pauli averaged (D.9), only the constant terms in the x and z vector components do not vanish. The nonzero averages are simply given by:

$$\langle J_{i,q} \rangle_{\delta_Q} = C_{i,q} \quad \text{for } i \in \{1,2\} \text{ and } q \in \{x,z\} \quad (\text{D.10})$$

4. Averaging terms Quadratic in space fixed J components

The general quadratic Pauli average is written

$$\langle J_{i,q} J_{j,q'} \rangle_{\delta_Q} \equiv \frac{1}{2\pi} \oint J_{i,q} J_{j,q'} d\delta_Q \quad (D.11)$$

The calculation of the fully perturbed Hamiltonian requires the following averages:

(i) Averages of quadratic components with $i = j$:

$$\langle J_{i,q}^2 \rangle_{\delta_Q} = \frac{1}{2} A_{i,q}^2 + C_{i,q}^2 \quad (D.12)$$

(ii) Averages of quadratic components $i \neq j$:

$$\text{For } q, q' \neq y: \langle J_{1,q} J_{2,q'} \rangle_{\delta_Q} = A_{1,q} A_{2,q'} \frac{1}{2} \cos(2\delta_w) + C_{1,q} C_{2,q'} \quad (D.13)$$

$$\text{For } q \neq y, q' = y: \langle J_{1,q} J_{2,y} \rangle_{\delta_Q} = -A_{1,q} A_{2,y} \frac{1}{2} \sin(2\delta_w) \quad (D.14)$$

$$\text{For } q \neq y, q' = y: \langle J_{2,q} J_{1,y} \rangle_{\delta_Q} = A_{2,q} A_{1,y} \frac{1}{2} \sin(2\delta_w) \quad (D.15)$$

$$\text{For } q = q' = y: \langle J_{1,y} J_{2,y} \rangle_{\delta_Q} = \frac{1}{2} A_{1,y} A_{2,y} \cos(2\delta_w) \quad (D.16)$$

5. Pauli average of the first order Hamiltonian

The first order Hamiltonian is entirely linear in the space fixed components of the \mathbf{J} vectors.

$$\bar{H}_1 = \bar{\Omega}_1 \cdot \bar{\mathbf{J}}_1 + \bar{\Omega}_2 \cdot \bar{\mathbf{J}}_2 \quad (D.17)$$

Using (D.10) the averaged first order Hamiltonian is;

$$\langle \bar{H}_1 \rangle_{\delta_q} = \frac{B}{2} \langle J_{1,z} + J_{2,z} \rangle_{\delta_q} - \frac{3}{2} N F_x \langle J_{1,x} - J_{2,x} \rangle_{\delta_q} = \frac{B}{2} (C_{1,z} + C_{2,z}) - \frac{3}{2} N F_x (C_{1,x} - C_{2,x}) \quad (D.18)$$

Substitution of (D.8) and using the definition of ω_f (D.2) then yields: $\langle \bar{H}_1 \rangle_{\delta_q} = \omega_f Q$

(D.19)

6. Pauli average of the second order Hamiltonian

$$\bar{H}_2 = \underbrace{-\frac{3}{2} N F_z \langle J_{1,z} - J_{2,z} \rangle}_{z\text{-Stark}} + \underbrace{\frac{N^2 B^2}{16} \left[3N^2 + 4\langle J_{1,z} J_{2,z} \rangle - 8\langle J_{1,x} J_{2,x} + J_{1,y} J_{2,y} \rangle - 4\langle J_{1,z}^2 + J_{2,z}^2 \rangle \right]}_{\text{Diamagnetic}}$$

$$- \underbrace{\frac{N^4 F_x^2}{16} \left[17N^2 + 48\langle J_{1,y} J_{2,y} + J_{1,z} J_{2,z} \rangle - 12\langle J_{1,x}^2 + J_{2,x}^2 + J_{1,x} J_{2,x} \rangle \right]}_{\text{Quadratic Stark}}$$

(D.20)

a. z-Stark Term

Effects of near perpendicular fields are contained in a second order term that is linear in the J components;

$$-\frac{3}{2} N F_z \langle J_{1,z} - J_{2,z} \rangle = -\frac{3}{2} N F_z (C_{1,z} - C_{2,z}) = -\frac{1}{4} \frac{3 N F_z B}{\omega_f} W \quad (\text{D.21})$$

b. Diamagnetic Term

The second term in (D.20) is:

$$DT = \frac{N^2 B^2}{16} \left[3N^2 + 4\langle J_{1,z} J_{2,z} \rangle - 8\langle J_{1,x} J_{2,x} + J_{1,y} J_{2,y} \rangle - 4\langle J_{1,z}^2 + J_{2,z}^2 \rangle \right] \quad (\text{D.22})$$

The required averages are:

$$\langle J_{1,z} J_{2,z} \rangle = \frac{1}{2} A_{1,z} A_{2,z} \cos(2\delta_w) + C_{1,z} C_{2,z} \quad (\text{D.23.a})$$

$$\langle J_{1,x}J_{2,x} + J_{1,y}J_{2,y} \rangle = \frac{1}{2} [A_{1,x}A_{2,x} + A_{1,y}A_{2,y}] \cos(2\delta_w) + C_{1,x}C_{2,x} \quad (\text{D.23.b})$$

$$\langle J_{1,z}^2 + J_{2,z}^2 \rangle = \frac{1}{2} [A_{1,z}^2 + A_{2,z}^2] + C_{1,z}^2 + C_{2,z}^2 \quad (\text{D.23.c})$$

After substitution of equations (D.8) and (D.23) into (D.22), simplification of the resulting expression is expedited by the following convenient definitions:

$$\Theta \equiv \sqrt{N^2 - (Q+W)^2} \sqrt{N^2 - (Q-W)^2} \frac{\cos 2\delta_w}{2} \quad (\text{D.24.a})$$

$$\gamma \equiv \frac{B^2}{B^2 + (3NF_x)^2} = \frac{B^2}{4\omega_f^2} \quad (\text{D.24.b})$$

Where (b) implies:

$$\left(\frac{3NF_x}{4\omega_f} \right)^2 = \frac{1}{4} (1 - \gamma) \quad (\text{D.24.c})$$

Then the diamagnetic term simplifies to:

$$\text{DT} = \frac{N^2 B^2}{16} \left[(2 + \gamma)N^2 + (3 - 4\gamma)Q^2 - (3 + \gamma)\Theta - (1 + 2\gamma)W^2 \right] \quad (\text{D.25})$$

c. Quadratic Stark Terms

The third term in (D.20) is:

$$\text{QST} = -\frac{N^4 F_x^2}{16} \left[17N^2 + 48 \langle J_{1,y}J_{2,y} + J_{1,z}J_{2,z} \rangle - 12 \langle J_{1,x}^2 + J_{2,x}^2 + J_{1,x}J_{2,x} \rangle \right]$$

The required averages are:

$$\langle J_{1,y}J_{2,y} + J_{1,z}J_{2,z} \rangle = \frac{\cos 2\delta_w}{2} (A_{1,y}A_{2,y} + A_{1,z}A_{2,z}) + C_{1,z}C_{2,z}$$

$$\langle J_{1,x}^2 + J_{2,x}^2 + J_{1,x} J_{2,x} \rangle = \frac{\cos 2\delta_w}{2} A_{1,x} A_{2,x} + \frac{1}{2} [A_{1,x}^2 + A_{2,x}^2] + C_{1,x}^2 + C_{2,x}^2 + C_{1,x} C_{2,x}$$

After substitution of equations (D.8) and definitions (D.24.a) and (D.24.b) the term is simplified to:

$$\text{QST} = \frac{N^2 (3NF_x)^2}{16} \left[\left(\frac{\gamma}{3} - \frac{17}{9} \right) N^2 + \left(\frac{1}{3} - 2\gamma \right) Q^2 - \gamma \Theta + W^2 \right]$$

Finally we use the relation $\gamma(3NF_x)^2 = (1-\gamma)B^2$ as implied by (D.24.b) to selectively convert F^2 terms to B^2 terms before the summation of all second order terms. We obtain the following:

$$\text{QST} = \frac{N^2}{16} \left[\left(\frac{B^2}{3} [1-\gamma] - 17N^2 F_x^2 \right) N^2 + \left(\frac{1}{3} (3NF_x)^2 + 2B^2 [\gamma-1] \right) Q^2 + B^2 [\gamma-1] \Theta + (3NF_x)^2 W^2 \right]$$

(D.26)

Summing the terms in equations (D.21), (D.25) and (D.26) and simplifying yields the Pauli averaged second order Hamiltonian h_2 . We h_2 divide into two parts, where h_{diff} is the part of h_2 which is independent of W and δ_w .

$$h_{\text{diff}} = \frac{N^2}{16} \left[N^2 \left(\frac{B^2}{3} [7+2\gamma] - 17N^2 F_x^2 \right) + Q^2 \left(\frac{1}{3} (3NF_x)^2 + B^2 [1-2\gamma] \right) \right] \quad (\text{D.27})$$

$$h_2 - h_{\text{diff}} = -\frac{1}{4} \frac{3NF_z B}{\omega_f} W + \frac{N^2}{16} \left[-2B^2 \sqrt{(N^2 - (Q+W)^2)(N^2 - (Q-W)^2)} \cos(2\delta_w) + \{(3NF_x)^2 - B^2(1+2\gamma)\} W^2 \right] \quad (\text{D.28})$$

APPENDIX E: DETAILED ANALYSIS OF h_2 ON $\Gamma_{N,Q}$

Non-polar fixed points of h_2 are located on $\Gamma_{N,Q}$ at values of the coordinates where both of the following equations are satisfied.

$$2\alpha \sin(2\delta_w) \sqrt{(N^2 - (Q+W)^2)(N^2 - (Q-W)^2)} = 0 \quad (E.1)$$

$$[2\beta W + \zeta] \sqrt{(N^2 - (Q+W)^2)(N^2 - (Q-W)^2)} = -2\alpha \cos(2\delta_w) W [W^2 - Q^2 - N^2] \quad (E.2)$$

1. Solutions in the General Case

In Eq. (E.1), the square root only vanishes in the limit that $W \rightarrow \pm(N-|Q|)$ at the poles of $\Gamma_{N,Q}$ and $\alpha = 0$ only if $\mathbf{B}=0$. For $|W| < N-|Q|$ and $\mathbf{B} \neq 0$, Eq. (E.1) will only be satisfied for

$$\delta_w = 0, \pm\pi/2 \quad (E.3)$$

Squaring both sides of (E.2) and sorting by powers of W yields the following inhomogeneous 6th order polynomial;

$$\begin{aligned} & W^6 \{4(\beta^2 - \alpha^2 \cos^2(2\delta_w))\} \\ & + W^5 \{4\zeta\beta\} \\ & + W^4 \{\zeta^2 + 8(N^2 + Q^2)[\alpha^2 \cos^2(2\delta_w) - \beta^2]\} \\ & + W^3 \{-8(N^2 + Q^2)\zeta\beta\} \\ & + W^2 \left\{ \begin{aligned} & [N^2 - Q^2]^2 4\beta^2 - 2\zeta^2(N^2 + Q^2) \\ & - (Q^2 + N^2)^2 \{\alpha^2 \cos^2(2\delta_w) 4\} \end{aligned} \right\} \\ & + W \{[N^2 - Q^2]^2 4\zeta\beta\} \\ & + \zeta^2 [N^2 - Q^2]^2 = 0 \end{aligned} \quad (E.4)$$

Solutions which are of physical interest are the real roots of (E.4) which do not exceed $N-|Q|$ in magnitude, and satisfy equation (E.2). Special cases simplify (E.4) producing several useful formulae.

2. Solutions for $Q=0$

Setting $Q=0$ in equation (E.2) yields:

$$\{\beta - \alpha \cos(2\delta_w)\} W + \frac{\zeta}{2} = 0 \quad (E.5)$$

For perpendicular fields $\zeta=0$ and (E.5) is satisfied if either of the following two equations are satisfied.

$$W = 0 \quad (\text{E.6})$$

$$\beta = \alpha \cos(2\delta_w) \quad (\text{E.7})$$

Together, (E.8) and (E.4) imply that for perpendicular fields and $Q=0$, two fixed points will always be present on the equator $W=0$ at the points:

$$(W, \delta_w) \in \{(0,0), (0, \pm\pi/2)\} \quad (\text{E.8})$$

If $\beta - \alpha \cos(2\delta_w) \neq 0$ then for small χ , these two equatorial fixed points are perturbed to new values of W given by:

$$W = -\frac{\zeta}{2\{\beta - \alpha \cos(2\delta_w)\}} \quad (\text{E.9})$$

Equation (E.7) is independent of W , and if satisfied yields two values of δ_w for which $\partial h_2 / \partial W = 0$ for all W . It follows that the resulting contour of h_2 on the flat representation of the (W, δ_w) surface must intersect the upper and lower boundaries in a pair of T-points (Fig. 5.1(a)). For $B \neq 0$, $\alpha \neq 0$ and condition (E.8) may be inverted to yield:

$$\delta_w^T = \pm \frac{1}{2} \cos^{-1} \left(\frac{\beta}{\alpha} \right) \quad (\text{E.10})$$

For a certain range of field strength ratios such that $-1 \leq \beta/\alpha \leq 1$, equation (E.11) defines a double branched function $\delta_w^T(\theta)$ whose values satisfy Eq. (E.9) for all W .

$\delta_w^T(\theta)$ is only defined for $-1 \leq \beta/\alpha \leq 1$, and limits on the values of θ for which T-points are present are determined by the following two equations.

$$\beta = \alpha \quad (\delta_w^T = 0 \rightarrow \text{least possible } \theta) \quad (\text{E.11})$$

$$\beta = -\alpha \quad (\delta_w^T = \pm\pi/2 \rightarrow \text{greatest possible } \theta) \quad (\text{E.12})$$

If Equations (E.11) and (E.12) are solved for θ , one finds that for perpendicular fields the T-points can only exist on the interval $\theta_{\min} \leq \theta \leq \theta_{\max}$, where:

$$\theta_1 = \cos^{-1} \left[\frac{1}{2^{1/4}} \right] \sim 32.765 \quad (\text{E.13})$$

$$\theta_2 = \cos^{-1} \left[\sqrt{\frac{\sqrt{6}}{2}} - 1 \right] \sim 61.701 \quad (\text{E.14})$$

The values of the δ_w which produced the T-points were obtained from (E.7) for arbitrary W . Since level sets which have T-points extend into the poles, we may substitute the values $W = \pm N$ into (E.5), and solve for the perturbed T-point angles. The resulting solution will be valid

for W near the poles $|W| \sim N$, producing the angles of T-points for nearly perpendicular fields.

$$\delta_w^{\mp\pm} = \frac{1}{2} \cos^{-1} \left[\frac{\beta \pm \frac{\zeta}{2\alpha N}}{\alpha} \right] \quad (\text{E.15})$$

In Eq. (E.17), the +ve sign yields the angles of T-points at the North Pole, while -ve sign yields the angles of T-points at the South Pole.

Instead of solving (E.15) for θ at fixed χ , we can hold θ fixed and solve for the critical values of χ . These values will define where the T-points leave the phase space (0 or $\pi/2$). Solving (E.15) for χ yields:

$$\chi_{\text{crit}} = \mp 2N \frac{\alpha \cos(2\delta_w) - \beta}{\omega_f \cos \theta \sin \theta} \quad (\text{E.16})$$

Evaluating (E.16) at the maximum and minimum possible T-point angles $\delta_w = 0$ and $\delta_w = \pi/2$ yields:

$$\chi_{\text{crit}}^1 = \mp \frac{2N}{\omega_f} \frac{\alpha - \beta}{\cos \theta \sin \theta} \quad (\text{E.17a})$$

$$\chi_{\text{crit}}^2 = \mp \frac{2N}{\omega_f} \frac{\alpha - \beta}{\cos \theta \sin \theta} \quad (\text{E.17b})$$

3. Solutions for $F \cdot B = 0$ and all Q

For perpendicular fields $\zeta=0$ and Eq. (E.4) reduces to a homogeneous quadratic equation in W^2 . This equation has two roots located at $W=0$, and four additional roots which if nonzero, may be found by assuming $\beta - \alpha \cos(2\delta_w) \neq 0$ and solving for the roots of:

$$W = \pm \sqrt{(N^2 + Q^2) \pm 2N|Q| \sqrt{\frac{\beta^2}{\beta^2 - \alpha^2 \cos^2(2\delta_w)}}} \quad (\text{E.18})$$

The physical solutions W^* are real valued with $|W^*| \leq N - |Q|$. It follows that (i) the quantity $\beta^2/[\beta^2 - \alpha^2 \cos^2(2\delta_w)]$ must be positive and that (ii) the negative sign must be chosen under the outermost square root. Since we are ultimately seeking fixed points of h_2 , by Eq. (E.3) we need only look for solutions at $\delta_w = 0$ and $\delta_w = \pm\pi/2$ where in both cases $\cos^2(2\delta_w) = 1$. Then condition (i) implies that these additional perpendicular fixed points can only exist for $\theta < \theta_1$ or $\theta > \theta_2$, outside of the interval where the T-points can exist. Condition (ii) implies

$$N^2 + Q^2 - 2N|Q| \sqrt{\frac{\beta^2}{\beta^2 - \alpha^2}} \geq 0 \quad (\text{E.19})$$

which has the following critical solution $|Q| = Q_{\text{crit}}$ marking the value $|Q| = Q_{\text{crit}}$ for which no additional physical solutions exist for any Q with $|Q| > Q_{\text{crit}}$.

$$Q_{\text{crit}} = \frac{N(\beta \pm \alpha)}{\sqrt{\beta^2 - \alpha^2}} \quad (\text{E.20})$$

The appropriate sign choice in (E.20) is determined by the additional condition $|Q| \leq N$.

From (E.18) one deduces that as $Q \rightarrow 0$ these additional fixed points limit to $W = \pm N$ (the polar pinch points). For nonzero Q , and θ outside the monodromy interval, these polar points become non-polar fixed points which migrate from the poles towards the equator along either $\delta_w = 0$ ($\theta < \theta_1$) or $\delta_w = \pm\pi/2$ ($\theta > \theta_2$). There exists a maximal $|Q| = Q_{\text{crit}}$ such that $W = 0$, and the additional fixed points cease to exist.

-
- [1] Yu. N. Demkov, B. S. Monozon, and V. N. Ostrovskii, *Sov. Phys. JETP* **30** 775 (1970); T. P. Grozdanov, E. A. Solov'ev, *J. Phys. B: At. Mol. Opt. Phys.* **15** 1195 (1982); J. B. Delos, S. K. Knudson, D. W. Noid *Phys. Rev. A* **28** 7 (1983); P. A. Braun and E. A. Solov'ev, *Sov. Phys. JETP* **59** 38(1984); P. Schmelcher, L. S. Cederbaum, *Chem. Phys. Lett.* 208 548 (1993); P. Schmelcher, L. S. Cederbaum, *Phys. Rev. A* **47** 2634 (1993); E. Flöthmann, J. Main, K. H. Welge, *J. Phys. B* **27** 2821 (1994); J. Main, G. Wunner, *J. Phys. B: At. Mol. Opt. Phys.* **27** 2835 (1994); Robert C. Hilborn, Larry R. Hunter, Kent Johnson, Stephen K. Peck, Alison Spencer, and John Watson, *Phys. Rev. A* **50** 2467 (1994); Robert C. Hilborn, *American J. Phys.* **63** 330 (1995); J. von Milczewski, G. H. F. Dierksen, T. Uzer, *Phys. Rev. Lett.* **76** 2890 (1996); J. Main, M. Schwacke, G. Wunner, *Phys. Rev. A* **57** 1149 (1998); Charles Jaffé, David Farrelly, and T. Uzer, *Phys. Rev. A* **60**, 3833 (1999); J. Rao, D. Delande and K. T. Taylor, *J. Phys. B: At. Mol. Opt. Phys.* **34** L391 (2001); D. M. Wang, J. B. Delos, *Phys. Rev. A* **63** 043409 (2001); T. Bartsch, J. Main, G. Wunner, *Phys. Rev. A* **67** 063411 (2003); S. Gekle, J. Main, T. Bartsch, T. Uzer, *Phys. Rev. A* **75** 023406 (2007); And references that follow.
- [2] W. Pauli, *Z. Phys.* **36** 336 (1926); Eng. Trans. - B. L. Van der Waerden, *Sources of Quantum Mechanics*, Dover Pub., N.Y. (1967).
- [3] F. Penent, D. Delande, F. Biraben, J. C. Gay, *Optics Comm.* **49** 184 (1984); F. Penent, D. Delande and J. C. Gay, *Phys. Rev. A* **37** 4707 (1988); G. Wiebusch, J. Main, K. Krüger, H. Rottke, A. Holle, K. H. Welge, *Phys. Rev. Lett.* **62** 2821 (1989). G. Raithel, M. Fauth, and H. Walther, *Phys. Rev. A* **44** 1898 (1991); G. Raithel and H. Walther, *Phys. Rev. A* **49** 1646 (1994);
- [4] D. A. Sadovskii and B. I. Zhilinskii, *Phys. Rev. A* **57** 2867 (1998); N. Berglund and T. Uzer, *Found. Of Phys.* **31** 283 (2001).
- [5] P. Bellomo, C. R. Stroud, D. Farrelly, T. Uzer, *Phys. Rev. A* **58** 3896 (1998).
- [6] M. J. Gourlay, T. Uzer and D. Farrelly, *Phys. Rev. A* **47** 3113 (1993).
- [7] J. von Milczewski and T. Uzer, *Phys. Rev. A* **56** 220 (1997).
- [8] E. A. Solove'v, *Sov. Phys. JETP* **58** **63** (1983).

- [9] D. R. Herrick, *Phys. Rev. A* **26** 323 (1982).
- [10] P. A. Braun, *Rev. Mod. Phys.* **65** 115 (1993).
- [11] R. H. Cushman and D. A. Sadovskii, *Physica D* **142** 166 (2000).
- [12] R. H. Cushman and D. A. Sadovskii, *Europhys. Lett.* **47** 1 (1999).
- [13] K. Efstathiou, R. H. Cushman, D. A. Sadovskii, *Physica D* **194** 250 (2004).
- [14] C. R. Schleif and J. B. Delos, *Phys. Rev. A* **76** 013404 (2007)
- [15] C. R. Schleif and J. B. Delos, *Phys. Rev. A* **77** 043422 (2008)
- [16] A. Einstein, *Verhandl. deut. physik. Ges.* **19** 82 (1917)
- [17] L. Brillouin, *J. Phys. radium* **7** 353 (1926)
- [18] J. B. Keller, *Ann. of Phys.* **4** 180 (1958)
- [19] V. P. Maslov and M. V. Fedoriuk, *Semi-Classical Approximation in Quantum Mechanics*, D. Reidel Boston (1981)
- [20] Nearly-perpendicular, weak fields means: $|\chi| \lesssim \omega_f N^3 \ll 1$.
- [21] The quantum basis must include several n-manifolds or important effects, second order in the electric field, will be neglected.
- [22] Equivalently any single choice of action variable may be regarded as a smooth but multi-valued function of q and \hbar .
- [23] K. Efstathiou, D. A. Sadovskii and B. I. Zhilinskiĭ, *Proc. Roy. Soc. Ser. A* **463** 1771 (2007)
- [24] J. B. Delos, C. R. Schleif and G. Dhont, *Journal of Physics Conference Series* **99** 012005 (2008)
- [25] J. J. Duistermaat, *Commun. Pure Appl. Math.* **33** 687 (1980); R. Cushman and L. Bates, *Global Aspects of Classical Integrable Systems* (Birkhauser, Boston, 1997); M. S. Child, *J. Phys. A Math. Gen.* **31** 657 (1988); San Vu Ngòc, *Commun. Math. Phys.* **203** 465 (1999); B. I. Zhilinskiĭ, *Acta. Appl. Math.* **87** 281 (2005).
- [26] E. L. Stiefel and G. Scheifele, *Linear and Regular Celestial Mechanics*, Springer-Verlag New York (1970).
- [27] G. D. Birkhoff, *Dynamical Systems* (Am. Math. Soc., New York 1966) Vol. IX; F. G. Gustavson *Astron. J.* **71** 670 (1966).
- [28] M. L. Du and J. B. Delos, *Phys. Rev. A* **38** 1896 (1988); M. L. Du and J. B. Delos, *Phys.*

- Rev. A* **38** 1913 (1988); J. Gao and J. B. Delos, M. Baruch, *Phys. Rev. A* **46** 1449 (1992); J. Gao and J. B. Delos, *Phys. Rev. A* **46** 1455 (1992); J. Gao and J. B. Delos, *Phys. Rev. A* **49** 869 (1994); Jörg Main and Günter Wunner, *J. Phys. B* **27**, 2835 (1994); D. M. Wang and J. B. Delos, *Phys. Rev. A* **63** 043409 (2001); S. Freund, R. Ubert, E. Flöthmann and K. Welge, D. M. Wang and J. B. Delos, *Phys. Rev. A* **65** 053408 (2002); T. Bartsch, J. Main, G. Wunner *Phys. Rev. A* **67** 063410 (2003); T. Bartsch, J. Main, G. Wunner *Phys. Rev. A* **67** 063411 (2003).
- [29] J. J. Duistermaat, *Commun. Pure Appl. Math.* **33** 687 (1980)
- [30] R. Cushman and L. Bates, *Global Aspects of Classical Integrable Systems* (Birkhauser, Boston, 1997)
- [31] M. S. Child, *J. Phys. A Math. Gen.* **31** 657 (1988)
- [32] San Vu Ngòc, *Commun. Math. Phys.* **203** 465 (1999)
- [33] B. I. Zhilinskií, *Acta. Appl. Math.* **87** 281 (2005).
- [34] M. Born, *The Mechanics of the Atom* (Frederick Ungar, New York, 1927, 1960).
- [35] H. Goldstein, *Classical Mechanics* (Addison Wesley, New York, 2002).
- [36] J. B. Delos, S. K. Knudson, D. W. Noid, *Phys. Rev. A* **28**, 7 (1983).
- [37] L. I. Schiff, *Quantum Mechanics* (McGraw-Hill, London, 1955, 1968).
- [38] This 2-form is undefined at points where $|\mu_i| = \pm N/2$, but all necessary integrals are well defined.
- [39] These circles have coordinates ψ_1 or ψ_2 , whichever survives according to the discussion in Section VIII B.
- [40] The space of Pauli orbits at fixed Q (the (W, δ_W) surface) is homeomorphic to a sphere, but we do not establish that it is diffeomorphic to sphere.
- [41] The classical spectrum is also known as the image of the energy momentum map.
- [42] For some parameters, a dashed red curve appears on classically doubly degenerate points of the classical spectrum. Specific examples are the upper boundary of the inner triangular region for Stark Region, and the lower boundary of the inner triangular region for Zeeman Region. In these cases, only one of the two disjoint components of the level set is not a 2-torus. Such cases will always be evident when inspecting the contours of h_2 on the (W, δ_W) surface.

- [43] Eqs. 58 cannot be linearized at the poles of the (W, δ_W) surface, and extrema at the poles are not quadratic.
- [44] V. I. Arnold, *Mathematical Methods of Classical Mechanics* (Springer-Verlag, New York, 1979).
- [45] The reference point of the action may be taken to be at $Q = 0$. All other choices of reference point would yield an action that differs from Eq. 62 by an additive constant.
- [46] For $0 < |Q| < N$, close examination of curves passing through the poles is needed.
- [47] By construction, the action is only defined for areas which are bound by contours of $h_2(W, \delta_W)$ which do not contain fixed points. See CH 10 of Ref. [44].
- [48] E. U. Condon and G. H. Shortley, *The Theory of Atomic Spectra* (Cambridge University Press, New York, 1935).
- [49] In the definitions of the \hat{Q} and \hat{W} operators, the field vectors \mathbf{F} and \mathbf{B} can be replaced with arbitrary vectors \mathbf{V}_1 and \mathbf{V}_2 such that the operators \hat{H}_0 , \hat{Q} and \hat{W} would form a complete set of commuting observables on a basis of bound states of the unperturbed hydrogen atom.
- [50] A lattice can be constructed from a list of energy levels alone. see Ref. [14].
- [51] In the Stark Limit, the equator $W = 0$ has exceptional structure. It is composed entirely of relative fixed points. Similar exceptional structure is found on $\Gamma_{N, Q=0}$ for \mathbf{F} and \mathbf{B} which lie on the (black and blue online) curves dividing regions of the map.
- [52] Quantum calculations also show that states belonging to different q and n manifolds also exhibit anti-crossings with variations in ω_f .
- [53] See EPAPS Document Number [] for a detailed derivation. For more information on EPAPS see <http://www.aip.org/pubservs/epaps.html>. This material will also be available for download from www.chrisschleif.com until the first author's demise.
- [54] See chapter 22 of Ref. [34] or chapter 3.8 Ref. [35].
- [55] See Fig. 13 of Ref. [34].
- [56] See chapter 4.4 of Ref. [35].
- [57] In the six dimensional phase space \mathbb{R}^{2n} , K is either diffeomorphic to a circle ($L \neq 0$) or its compactification is. Each point $x \in K \subset \mathbb{R}^{2n}$ is labeled by a value of the Delaunay coordinate ϕ_N .

VITA**Christopher Robert Schleif**

Chris Schleif was born a child of Peter Robert Schleif and Franka Deluca in Mt. Kisco, New York on March 28, 1975. He graduated from John Jay High School in Katonah, New York in 1993. He then earned a bachelor's degree of music from Hartt School of Music, West Hartford Connecticut in 1997. After a few years he went back to school in 2000. After completing some physics courses at SUNY Geneseo, Geneseo New York, he was accepted in the physics graduate program at the College of William and Mary, Williamsburg Virginia in 2002. He completed a Doctoral Thesis in theoretical AMO physics at the department of physics at the College of William and Mary while working under the guidance of John Delos on June 9, 2008.